**Title**

The Design and Modeling of Periodic Materials with Novel Properties

**Author**

Berger, Jonathan Bernard

**Publication Date**

2014

UNIVERSITY OF CALIFORNIA

Santa Barbara

# The design and modeling of periodic materials with novel properties

A dissertation submitted in partial satisfaction of the
requirements for the degree Doctor of Philosophy
in Materials

by

Jonathan Bernard Berger

Committee in charge:
Professor Robert McMeeking, Chair
Professor Tresa Pollock
Professor Frank Zok
Professor Matthew Begley

June 2014

The dissertation of Jonathan Bernard Berger is approved.

Tresa Pollock

Frank Zok

Matthew Begley

Robert McMeeking, Committee Chair

June 2014

The Design and Modeling of Periodic Materials with Novel Properties

# ACKNOWLEDGEMENTS

This is dedicated to my family, to whom I owe the utmost gratitude; without your love and support this work would not exist. And to all my friends and colleagues, who routinely amaze me with their brilliance and kindness, you are a constant inspiration, surely not enough thanks are said.

This work is dedicated to my  parents who have supported me totally. I cannot imagine a greater gift than life you have given me. And to my older siblings, Tim and Amy, who taught me, by example, the courage to go out and explore the world.

There is a huge list of people that I would like to thank that helped shape my life and make this possible. I feel overwhelmed with the love so many people have shown me throughout my life. Especially the Radcliffe and Schwartz families, who made me feel like a part of theirs.

While I seem to have found a home in Santa Barbara, I dearly miss everyone back in Whistler, BC. A huge thanks to Kevin Freeman for being a dear friend and keeping my bike rolling all these years. Thanks to the crews at Mountain Riders and FanatykCo for all the great times, gainful employment, for letting me take up space and helping when my stuff was broken, and just adding so much to my years riding the hill—Dillan, Brad, Karen, Guy, Dave, Kevin, Scotty, Bruce, Budgie, Bernie, Karen Sabine, Cory, and everyone else.

For many years Whistler and Blackcomb mountains felt like home thanks to many people. Aside from being an amazingly warm and wonderful person, Karen Bauckham gave me a chance to do something a little more professional and serious in a town overflowing with fun and silliness.

The Velopro Cyclery became my second home almost immediately upon my move to Santa Barbara. A big thanks to Greg Hirsch and Ed Brown for holding down the fort for so many years, Daryl Abrahms for keeping the doors open, Eric Lohela for getting me the job, and to Julian Peters, Sam, Tom, and everyone else for making The Pro what it is and was. Mountain biking is a huge part of my life, it helped bring me to Santa Barbara, kept me healthy and happy during the stressful times in life, and I owe a huge thanks to the people that help keep it in my life.

Ironically perhaps I have always been a little antisocial when it comes to riding bikes and snowboards—I just love the peace of getting out into the hills by myself—but the people I know through riding are some of the best I have ever had the privilege of meeting. When we did ride together—Brent, Dillan, Corey, Zasho

Donner, Jesse Kurrasch, and Preston Moore and so many others—it was hard to have more fun or be surrounded by better company.

I did actually go to school too. Dr. Mike Young and Dr. Nick Arnold at Santa Barbara City College were instrumental in turning a fulltime mountain biker into a budding scientist. If it were not for the intensely interesting and challenging classes they taught I almost certainly be here today.

As a longtime friend and officemate, Chance Holland and I went through nearly three years of mechanical engineering undergraduate work, and finished our Ph.D.'s under the same adviser, at nearly the same time. We were comrades in arms on the engineering battlefield, sharing many scars and victories. It was a great gift to have such company on such a long and fantastic journey.

For more than ten quarters, as an undergraduate and graduate, I had the privilege of working for Dr. John and Janice Baldwin in the Sociology Department at UCSB. Their Sociology 152a course on the sociology of human sexuality was, by both quantity and quality, the premier source of practical education on campus—being a part of it changed my life and so many others. The Baldwin's embody the joy of teaching and learning. They are not just colleagues, but also great friends, and a constant source of inspiration.

Getting to actually make something you designed, to turn an idea into reality, is a great privilege. Bringing something into the world that wasn't before is a special experience. It is perhaps a bit ironic then that the first thing we often want to do is then break it. A big thanks to engineers like Pete Maxwell, without whose assistance many projects would not have become reality. And to Kirk Fields, for helping me squish many things, mostly in the name of science, and whose time and advice were invaluable on countless topics.

As an undergraduate, there is no teacher that stood out more than Dr. Keith Kedward, whose love for people, life, engineering, and seemingly everything, was a privilege and joy to be around. His advice, encouragement, instruction and example were second to none.

A huge thanks to professors in the Materials Department at UCSB, bother former and current, David Clarke, Robert Odette and Susanne Stemmer, who not only were great teachers but who's encouragement to purse a PhD was instrumental. Tony Evans, my former co-adviser, may he rest in peace, was a truly incredible person as anyone who knew him can well attest. His warmth, kindness, brilliance and hard work set the bar for us all.

Completing this graduate thesis is truly the culmination of years of study and work. It was enabled only through the time, assistance and advice of many incredible people. I cannot think of a more esteemed, bright, and knowledgeable group than the members of my committee, Tresa Pollock, Frank Zok and Matthew Begely. Sharing and developing one's work is in the essence of science, and being able to share mine with such eminent engineers and great people was an immense privilege.

And a very special thanks to my adviser, Bob McMeeking. Your kindness, generosity, advice, support and the huge amount of trust you placed in me, made my graduate school experience truly amazing.

While these people have influenced my life in so many different ways, and at so many different times, it is because of them that I am who I am today--I cannot thank you all enough. There are many other people who, given the space, I would love to pay thanks to for helping to make my life what it has been. Thank you all!

# VITA OF JONATHAN BERNARD BERGER

January 2014

## EDUCATION

Bachelor of Science, University of California, Santa Barbara, June 2007 (high honors)
Doctor of Philosophy in Materials, University of California, Santa Barbara, February 2014 (expected)

## PROFESSIONAL EMPLOYMENT

2006-07: Grader, Department of Sociology, University of California, Santa Barbara
2006-08: Course Assistant, Department of Sociology, University of California, Santa Barbara
2005-08: Teaching Assistant, Department of Materials, University of California, Santa Barbara

## PUBLICATIONS

“The Design of Bonded Bimaterial Lattices that Combine Low Thermal Expansion with High Stiffness,” *Journal of the American Ceramic Society*, Vol. 94, S1 (2011) s42-s54

“The compressive response of some idealized foams,” Unpublished thesis submitted in partial fulfillment of the requirements for the Doctor of Philosophy Degree, University of California, Santa Barbara, 2014. 74 pp.

## AFFILIATIONS

President, Tau Beta Pi, California Sigma Chapter (2006-2007)
UCSB Engineering Honors Society (2005-2007)

## FIELDS OF STUDY

Major Field: Structural Materials

Studies in Tailorable Thermal Expansion Materials with Professor Anthony Evans

Studies in the Brittle Response of Ceramics with Professor Robert McMeeking

Studies in the Performance of Foams and Lattices

# ABSTRACT

## The Design and Modeling of Periodic Materials with Novel Properties

by

Jonathan Bernard Berger

Cellular materials are ubiquitous in our world being found in natural and engineered systems as structural materials, sound and energy absorbers, heat insulators and more. Stochastic foams made of polymers, metals and even ceramics find wide use due to their novel properties when compared to monolithic materials. Properties of these so called *hybrid materials*, those that combine materials or materials and space, are derived from the localization of thermomechanical stresses and strains on the mesoscale as a function of cell topology. The effects of localization can only be generalized in stochastic materials arising from their inherent potential complexity, possessing variations in local chemistry, microstructural inhomogeneity and topological variations. Ordered cellular materials on the other hand, such as lattices and honeycombs, make for much easier study, often requiring analysis of only a single unit-cell. Theoretical bounds predict that hybrid materials have the potential to push design envelopes offering lighter stiffer and stronger materials. Hybrid materials can achieve very low and even negative coefficients of thermal expansion (CTE) while retaining a relatively high stiffness – properties completely unmatched by monolithic materials. In the first chapter of this thesis a two-dimensional lattice is detailed that possess near maximum stiffness, relative to the tightest theoretical bound, and low, zero and even appreciably negative thermal expansion. Its CTE and stiffness are given in closed form as a function of geometric parameters and the material properties. This result is confirmed with finite elements (FE) and experiment. In the second chapter the compressive stiffness of three-dimensional ordered foams, both closed and open cell, are predicted with FE and the results placed in property space in terms of stiffness and density. A novel structure is identified that effectively achieves theoretical bounds for Young's, shear and bulk modulus simultaneously, over a wide range of relative densities, greatly expanding the property space of available materials with a pragmatic manufacturable structure. A variety of other novel and previously studied ordered foam topologies are also presented that are largely representative of the spectrum of performance of such materials, shedding insight into the behavior of all cellular materials.

# TABLE OF CONTENTS

# LIST OF FIGURES – CHAPTER I

Figure 13 – 304 stainless steel lattice compressed along the vertical axis. Bright areas indicate out of plane deformation associated with member buckling.

Figure 14 – Uniaxial compression strain-stress behavior or 304 Steel lattices. (a) Triangular Type 2 element. (b) Thin Type 2 members.

Figure 15 – Finite element stress distributions in uniaxially compressed 303 stainless steel lattices. Yielding occurs in struts linking triangle vertices to 6-member joints a-d involves out of plane displacements. This behavior agrees well with experimental results.

Figure 16 –Stress distributions in lattices made from Ti alloy and Al alloy with maximum biaxial stiffness as predicted by pin-jointed analytical model, subject to 0.1% biaxial tensile strain. Skew angles range from 24.5°-30° and volume fractions of solid from 14-46% (a-g). Stress distributions become more uniform with increasing slenderness moving towards behavior similar to the pin-jointed response.

Figure 17 – Results for the coefficient of thermal expansion and biaxial stiffness for lattices shown in Figure 16. Analytical results derived from a pin-jointed model are shown as are results from finite element analysis of lattices having bonded joints.

Figure 18 – The biaxial stiffness, $S_b$, of seven lattice geometries composed of Ti6AlV4 and 7075-T6 Aluminum and five composed of Haynes and a niobium alloy along with their respective theoretical bounds on stiffness, devised by Gibiansky and Torquato (1997), which is a function of constituent properties and volume fractions. At effective CTEs near the rule of mixtures structures with a higher relative density (yellow) have a greater potential for stiffness over those with lower density (orange). At large deviations from the rule of mixtures (approaching zero CTE) the potential stiffnesses (theoretical bounds) converge. Lattices with slender members have more uniform stress and strain energy distributions and perform closest to the theoretical bound (darkest orange). Normalized biaxial stiffness is a measure of stretching indicating that lattices achieve only a small fraction of the stiffness of a bilayer of identical composition. When the low CTE constituent is more compliant than the high CTE, as in the case of two high temperature alloys, Haynes 188 and a niobium alloy, the stiffness of this material system relative to the theoretical bounds is reduced when the effective CTE is near zero(purple).

# LIST OF FIGURES – CHAPTER II

Figure 31 - Normalized axial, shear and bulk moduli for quasi-random foams. Curve fits for $(\bar{E}/E_S)$ and $(\bar{G}/G_S)$ for $(\bar{\rho}/\rho_S) \lesssim 25\%$ are nearly identical to Equation (78) and (79) with $\phi = 2/3$. At higher relative densities a cubic term is necessary to describe the behavior. FE data from (Roberts and Garboczi, 2001) for similar quasi-random foams are in excellent agreement. FE mesh quality was poorer above $(\bar{\rho}/\rho_S) \approx 0.5$ due to limitations in the meshing algorithm, artificially stiffening results only slightly.

Figure 32 - Normalized effective axial, shear and bulk moduli (left, center and right respectively). Effective moduli are normalized by the moduli of the bulk material (top), and by the moduli of the bulk material and the Voigt bound (bottom) for the cases of $\bar{E}$ and $\bar{G}$, and by the Hashin-Shtrickman (H-S) upper bound for the case of bulk modulus. Contours of Equation (78) and (79) are shown (bottom-left and –center) where the linear stretching coefficient, $(1-\phi)$, are the $y$-intercepts. The axial and shear stiffness of the QR foams are plotted for comparison (left and center). All these materials have cubic symmetry so only one axial and shear modulus is reported. In the case of bulk modulus the results for direct calculations are shown with a diamond; they agree with the remaining calculations done using the axial modulus, the effective Poisson ratio, $\bar{\nu}_{ij}$, and the assumption of isotropy. While the H-S bound on bulk modulus is rigorous (right) the bounds on Young's and shear moduli are not due to the high degree of anisotropy of some designs.

Figure 33 - Normalized strain energy distributions in SC foams with wall thickness $t/L = 2\%$ and $t/L = 20\%$ (top and bottom respectively) under macroscopic axial compressive stress (left), shear (center) and hydrostatic compression (right). In all cases $\epsilon = 0.1\%$ which have been magnified 100X. Local strain energy densities are normalized by the average local strain energy density. Low density foams have large regions of uniform strain energy compared with higher density foams. Material in edges and vertices in walls under high stress is confined by neighboring material in the intersecting walls at lower stress. As wall thickness increases with relative density a degradation in performance is seen in all designs relative to the Hashin-Shtrikman upper bound on bulk modulus (Hashin and Shtrikman, 1963) due to this constrained material. Under shear loading two of three walls are relatively unstrained increasing the magnitude of this effect. (Negative strain energy levels indicated in legends are fictitious and do not actually occur in models.)

Figure 34 - Normalized strain energy distributions in FCC and BCC foams (top and middle) and Octet-truss (OT) (bottom) under axial, shear and hydrostatic loading (left, center and right). Strain energy contours of greatest interest and influence are plotted at the sacrifice of fidelity near strain energy concentrations; the magnitude of strain energy concentrations are of course mesh dependent and do not contribute substantially to the total strain energy. Under axial load strain energy is clearly concentrated in cell walls aligned with the applied stress (top- and middle-left) which

form stiff chains of material. Strain energy is more clearly partitioned by the local mode of deformation in the BCC foam whose square cell walls can store almost no strain energy depending on their orientation in both axial and shear case. The high shear stiffness of the OT results from the alignment of principle stresses with the longitudinal axis of truss members where strain energy is stored through stretching (bottom-center); under axial loading the OT undergoes mostly bending (bottom-left). (Negative strain energy levels indicated in legends are fictitious and do not actually occur in models.)

Figure 35 - Overall stiffness performance of ten ordered from geometries. The total stiffness (right) segregates the designs into three groups: a group with maximal performance whose total stiffness approaches the sum of the H-S bounds, $\Omega \rightarrow 1$ as $(\overline{\rho}/\rho_S) \rightarrow 0$ (heavy dashed lines), another group whose properties are close to that of the idealized stretch dominated material, having stiffness ~1/3 of the Voigt bound, that have $\Omega \approx 75\%$ as $(\overline{\rho}/\rho_S) \rightarrow 0$, and a third, only including the OT, whose performance is less than the others. On the right the total stiffness is multiplied by the isotropy, $a$, as a measure of isotropic stiffness where an ideal isotropic material has $= \Psi = 1$ . A structure produced from topology optimization by (Radman et al., 2012) to be isotropic and have maximum shear modulus has a total stiffness nearly identical to the OF+SC foam; it is slightly more anisotropic by equation (73) and therefor has lower Ψ (left). The scaling factor, $a$, is somewhat arbitrary in magnitude as the objective function is unbounded on one side. The OF+SC foam is found to have a stiffness, $\Omega \rightarrow 1$, as $(\overline{\rho}/\rho_S) \rightarrow 0$ and is nearly isotropic making it the only material with $\Psi \rightarrow \Psi_{HSU}$, as $\overline{\rho} \rightarrow 0$, giving it ideal properties far in excess of theoretical stretch dominated lattices. Materials with maximum stiffness are plotted with thick lines.

Figure 36 - Isotropy and effective Poisson ratios as a function of relative density for all geometries with the exception of the QR foams, which are effectively isotropic and have $\bar{\nu} \approx 0.30$. Materials with maximal stiffness are plotted with heavier lines.

Figure 37 - Normalized strain energy distributions under axial, shear and hydrostatic loading (left, center, and right respectively) at a macroscopic strain of $\boldsymbol{\epsilon}$=0.1% in the Octet-Foam (OF) (top), dodecahedral-pyramidal foam (DDPF) (2nd row), X-Foam (XF) (third-row) and Octet+'Simple Cubic' (OF+SC) foam (bottom). All strains are scaled 100X for clarity. Because the relative orientation of cell walls in the OF, being composed of regular tetrahedraons, the strain energy distributions in each wall are identical in the both axail and shear cases (top-left and –middle); in the shear case all walls are placed in a state of nearly pure compression or tension suggesting its shear stiffness is maximal, at least in the low density limit. (Negative strain energy levels indicated in legends are fictitious and do not actually occur in models.)

Figure 38 - Stiffness of X-Foam, Diamond (DF), dodecahedral pyramidal foam (DDPF) and Body+Face Centered (BFC) foams. The OF+SC foam has stiffness that is in excess of 99.9% of the H-S bound on Young's modulus, 97.1% the bound on shear and 98.3% of the bound on bulk modulus, at the lowest density analyzed. The H-S bounds on Young's and shear modulus do not limit the performance of some materials due to their anisotropy. The BFC foam is nearly isotropic with stiffness similar to the QR foams. The OF+SC, DDPF and XF all have bulk moduli that converge on the H-S bound at the low density limit (right). Topology optimization for an isotropic material with maximum shear modulus resulted in a design with similar performance to the OF+SC foam (black-square).

Figure 39 - Normalized strain energy distributions in the diamond foam (DF) (top) and the Body+Face Centered (BFC) (bottom), both with $t/L = 2\%$, at macroscopic strains of $\epsilon = 0.1\%$. Under axial loading cell walls aligned with the applied stress experience the highest strain energy density (left). Shear loading in the DF results in complementary buckling of neighboring antisymmetrically aligned cells at strains as low $\epsilon = 0.001\%$, when no initial cell wall curvature is present. The sub-maximal bulk stiffness of the DF and BFC foams is evident in the non-uniformity of the strain energy distributions between cell walls under hydrostatic loading (right). Contours of strain energy density around the average are plotted at the expense of fidelity near strain energy concentrations, the magnitude of which are mesh dependent and do not contribute substantially to the total strain energy. (Negative strain energy levels indicated in legends are fictitious and do not actually occur in models.)

Figure 43 - Strain energy distributions in cross-sections of DF with $t/L = 1\%$ (top) and $t/L = 8\%$ (bottom) from macroscopic shear loading; macroscopic strains of $\epsilon = 0.1\% = \gamma_{xy}/2$ are scaled 100x. Principle stress directions are horizontal and vertical. Cross-sections are taken at *z*=3/8, 1/2 and 5/8 (left to right respectively). As wall thickness increases the short ligaments thicken and shorten, decreasing in aspect ratio dramatically, increasing their bending stiffness and the overall shear stiffness of the design. Cell walls in the DF take on curvature at all shear strains, $\bar{\gamma}_{xy} > 0$, with zero initial wall curvature, yet the antisymmetric nature leaves some cross-sections with straight lines where antisymmetric buckling mechanisms converge (left and right columns). As relative density increases complementary buckling mechanisms are inhibited causing more energy to be stored through stretching. Contours of strain energy density around the average are plotted at the expense of fidelity near strain energy concentrations, the magnitude of which are mesh dependent and do not contribute substantially to the total strain energy. (Negative strain energy levels indicated in legends are fictitious and do not actually occur in models.)

Figure 44 – Ordered foams and lattices comprised of an Al-20%SiC composite outperform stochastic foams made from the same material. While the octet-truss has comparable shear stiffness to isotropic stretch dominated foams at low relative densities (~1/3 of the Voigt bound), it is anisotropic and has an axial stiffness that approaches that of stochastic foams at relative densities $\gtrsim 20\%$. The stiffness of the OF+SC foam is almost directly proportional to $E/\rho$, while the BFC foam, having stiffness similar to the Q-R foams (~1/3 of the Voigt bound at low relative densities), has the performance of theoretical stretch dominated lattices of (Ashby, 2011).

Figure 42 – Finite element (FE) results for the OF+SC foam composed of an Al-SiC composite, and Beryllium, are placed in the universe of available isotropic, or nearly isotropic, materials; excluded from this are fibers, laminates and woods. Only the stiffest foams, made of ceramics, rival the stiffness of the Al-SiC OF+SC foam, and then only at densities above 600 (kg/m$^3$). The OF+SC foam composed of Beryllium can potentially be more than one order of magnitude stiffer, at a given density, than currently available nearly isotropic materials; a system incorporating this material would realize a proportional and dramatic weight savings. As single crystal diamond is not a reasonable constituent material, and polycrystalline diamond has only half its stiffness, the maximally stiff OF+SC foam composed of beryllium represents the maximum performance achievable by any material system barring the development of new materials on the atomic scale.

# I. General Introduction

The ability to transmute a material, by altering some of its properties while retaining others, is one of the fundamental aims of materials science. And while the alchemical means of transforming lead into gold escapes us practically, it remains feasible to alter the properties of existing materials substantially by combining materials with contrasting properties into unique topologies. Porosity can be added to stiff, dense materials to create buoyancy and/or surface area, greatly altering its properties. Void space is routinely added to food, such as ice cream and bread, to modify and improve the mechanical properties while retaining the flavor and recipe. Lattice materials and foams are also examples of such meta-materials that derive their properties, in large part, from their topology.

In these meta-materials, deformations on the mesoscale dictate the properties of the macroscopic structure. In stochastic foams, such as those made of polymers for example, these mechanisms vary spatially in their nature and orientation resulting in local variations in compliance and density. This random distribution results in homogeneous or nearly homogeneous effective properties on the macroscale. While stochastic foams already offer unique material properties when compared to monolithic materials,  in the form of metal and polymer foams, making excellent insulators, energy absorbers and structural materials, it is easy to envision how ordering such local mechanisms, to work in tandem or in opposition, can alter substantially and improve certain properties such as stiffness and strength. In this thesis two such ordered systems are studied: a two-dimensional (2-D) lattice with tailorable coefficient of thermal expansion (CTE) and a family of ordered foams that exhibit a wide and representative range of properties, including one topology that simultaneously achieves theoretical bounds for Young's, shear and bulk modulus. These high-efficiency systems perform unlike any known bulk materials, and outperform all other known meta-materials, making them extremely interesting material systems of study.

In the first system, thermal stresses and strains inherent to the constituent materials are leveraged, through geometry, to primarily self-mitigate, resulting in a low, zero or even appreciably negative effective CTE. A near maximum amount of material is placed in tension in the process so that the material achieves a large fraction, greater than any other known topology, of theoretical bounds for stiffness. A variety of materials can be used as the only major thermomechanical requirement of the constituents is that they have an appreciable difference in CTEs, $\alpha_2/\alpha_1 \gtrsim 2.0$, where $\alpha_i$ are the CTE of the constituents. Metals can then be used in high-temperature environments when previously thermal expansion prohibited their use. This is particularly useful for the application of hypersonic flight where thermal loading is the primary design constraint. A combination of analytical modeling using beam theory, 3-D finite element representative volume element modeling and experimental data are utilized to illustrate the behavior and performance of this lattice design. There are many considerations when positing lattices for use in such demanding high-temperature environments, however, only the stiffness characteristics are considered in this study.

A different set of theoretical bounds limits the stiffness of foams and lattices; materials composed of a dense stiff phase and a void or gaseous phase. Stochastic foams and lattices have a history of study and application as structural materials, finding application in sandwich structures as stiff lightweight core materials. The currently burgeoning field of additive manufacturing--where material is placed selectively in space rather than removed from a dense one, as in machining--now allows for the production of arbitrary geometries with no penalty for complexity, making the design of closed cell foams with desirable properties, through the engineering of cell topology, now of practical consideration. In the aim of understanding the behavior and performance of various cell geometries, their performances are assessed with finite elements. Some historical geometries, such as the BCC Kelvin foam, a simple cubic/box foam, and others, shed light on the fundamental features that give rise to efficient designs. This insight is then used to design topologies that extend the performance range of available materials considerably, offering stiff lightweight meta-materials.

One unique topology in this group performs at the boundary of material property space in terms of isotropic stiffness, as it achieves theoretical bounds for Young's, shear and bulk modulus simultaneously. This material outperforms stiff stochastic foams and the in-plane stiffness of honeycombs by more than an order of magnitude at low relative densities. In any transportation application where the design requirements are stiffness limited, as in non-load bearing aerodynamic surfaces like an engine cowl, a proportional weight savings can be realized offering obvious and substantial improvements in efficiency. These and other topologies, most based upon a spatial tessellation procedure, possess properties not achieved by any other known material system reveling a unique class of materials.

Through studying theses periodic structures comes insight into the fundamental behavior of materials. The unique behavior of these two mostly disparate systems, both having stiffness that essentially achieve the respective appropriate theoretical bounds, shines light on the influential factors that lead to high-performance. In their study there is tangible evidence, in the deformations and strain energy concentrations, of the features and mechanisms responsible for such extreme behavior.

Contained in this work are not only designs of merit that may find direct use is engineered systems due to their unique properties, but also perhaps there are some lessons that will lead to the design of other unique material systems. Currently the design and fabrication of topological materials is in its adolescence with ripe with bountiful opportunities do create novel materials that greatly improve design capabilities.

# II. The Design of Bonded Bimaterial Lattices that Combine Low Thermal Expansion with High Stiffness

**In engineered systems where thermal strains and stresses are limiting, the ability to tailor the thermal expansion of the constituent materials independently from other properties is desirable. It is possible to combine two materials and space in such a way that the net coefficient of thermal expansion (CTE) of the structure is significantly different from the constituents, including the possibility of zero and negative thermal expansion. Bimaterial lattices that combine low, negative, or an otherwise tailored CTE with high stiffness, when carefully designed, have theoretical properties that are unmatched by other known material systems. Of known lattice configurations with tailorable CTE, only one geometry, a pin-jointed lattice, has been shown to be stretch dominated and thus capable of having stiffness that approaches its theoretical upper bound.**

**A related lattice with bonded joints, more amenable to fabrication, is developed that has a stiffness and CTE similar to the pinned structure. Analytical models for this rigid-jointed lattice's CTE and stiffness are developed and compared successfully with numerical results. A near space-**

**filling, negative thermal expansion version of this lattice is devised and fabricated from titanium and aluminum. CTE measurements on this lattice are made and are well predicted by the analytical and numerical models. These insights guide the design of a family of bonded lattices with low areal density, low or negative CTE, and high stiffness to density ratio. Such lattices are shown to have a thermomechanical response that converges on pin-jointed behavior when the lattice elements are long and slender.**

## *1. Introduction*

Recent assessments have elucidated bimaterial, planar lattice concepts that attain zero (or low) thermal expansion coefficients (Figure 1) [1-5]. Among these, only the configuration depicted in Figure 1d is known to combine low thermal expansion with high stiffness and strength. The lattice in Figure 1b is the result of topology optimization and has biaxial stiffness near theoretical bounds, but has poor uniaxial stiffness, suffers from edge effects in lattices with limited periodicity, and has a complex geometry [2]. Furthermore, the lattice in Figure 1d, hereby known as the UCSB Lattice, has properties that are transversely isotropic. Other stiff, strong, planar lattices have been identified that have zero, negative or low thermal expansions in specific directions within its plane [6], but are anisotropic, with significant thermal expansions in other in plane orientations.

In the lattice of Figure 1d, the members that govern its response are defined within the unit cell depicted in Figure 2. In this lattice, the outer, hexagonal (type I) members (length $L_1$ and width $w_1$) have the lower coefficient of thermal expansion $\alpha_1$, while the triangular, inner (type II) members (length $L_2$ and width, $w_2$) have relatively higher CTE, $\alpha_2$. At the nodal points A, J, F in the lattice (Figure 2), the ratio of the effective thermal expansion $\bar{\alpha}$ to the CTE of the type I material $\alpha_1$, is dictated by the constituent CTE-ratio, $\lambda = \alpha_2 / \alpha_1$, and by the skewness angle, θ, depicted in Figure 2. For a *pin-jointed* lattice, the expansion coefficient, $\bar{\alpha}$ has been derived as [5]:

$$\frac{\bar{\alpha}}{\alpha_1} = \frac{1 - (1/2)\lambda \sin(2\theta)(1/\sqrt{3} + \tan\theta)}{1 - (1/2)\sin(2\theta)(1/\sqrt{3} + \tan\theta)} \qquad (1.1)$$

For a representative material combination, Al alloy and Ti alloy, with λ ≈ 2.6, zero expansion prevails for a pin-loaded lattice at skewness θ ≈ 25° [5]. When the lattices are bonded, or otherwise mechanically-attached at the nodes to make them rigid joints, bending moments are introduced into the type I members and the thermal expansions are larger [5].

To assess these predictions, lattices based on Ti and Al alloys have been made, and their thermal expansion characterized [7]. Measurements obtained for a pin-jointed unit cell are in close agreement with the prediction of Eq. (1.1). Those measured for lattices assembled using mechanical (dovetail) attachments, *i.e.* with rigid joints, give larger thermal expansions. A variety of features adversely affect the reliability and repeatability of the thermal expansion of such rigid-jointed lattices: (i) Local plastic strains induced by the thermal expansion difference between constituents at the bimaterial attachment. (ii) Bending moments associated with the reduction in effective member lengths due to member overlap at the nodal points where six type-1 members from three neighboring unit cells converge (Type J Node, Figure 2). (iii) The reduction in effective length of type-1 members due to the intersection of struts at Type J and D nodes. (iv) The reduction in effective length of type-1 members due to material added at the dovetail bimaterial interface. A previous assessment has demonstrated that the detrimental effect of plasticity at the bimaterial attachment is minimal, because the plastic strains are highly localized, facilitating shakedown after the first few cycles [7]. Consequently, while the CTE mismatch at the attachment generates a non-linear, hysteretic contribution to the thermal strain during the first cycle, the thermal expansion *remains repeatable during all subsequent cycles*. A pre-conditioning treatment is sufficient to initialize the system and stabilize the thermal expansion.

The detrimental influence of the nodal geometry on the bending moments is more substantive. The elevation in the bending stiffness of the type I members associated with nodes of Type J significantly increases the overall thermal expansion coefficient, as determined both experimentally and by finite element analysis [7].

This detriment motivates a systematic study that seeks geometrically-straightforward configurations, amenable to manufacture, that impart thermal expansion closer to the pin-jointed prediction of Eq. (1.1), while retaining high stiffness and strength. The objective of this article is to seek such configurations, but with a focus, for the time-being, on stiffness.

The thermal expansion characteristics to be pursued emphasize designs that reduce the bending moments in the slender type I members. Analytic results are presented in section 2 for the original design and extended to an alternative, offset design (Figure 3). The alternative design is comprehensively analyzed in section 3 by the finite element method and specific designs discussed. It will be demonstrated that bonded, offset configurations can be conceived that have thermal expansions essentially the same as the pin-jointed lattice. Given the minimal member bending stiffness for these new lattices, basic elasticity results are derived for pin-jointed systems in section 4. These specify the salient trends in elastic response. Thereafter, a series of finite element (FE) results for rigid-jointed systems are generated to ascertain deviations in stiffness from the pin-joint predictions.

## ***2. Design Principles for Low Thermal Expansion***

Predicated on the foregoing assessment that the thermal expansions in excess of the pin-jointed lattice are primarily affected by the bending moments in the type I members, a beam theory methodology has been devised that identifies geometrically-straightforward designs that converge to pin-jointed behavior. Two design layouts are considered. (i) One conforms to Figure 2, with the effective rigidity of the material around the joints taken into account. (ii) The other allows the unit cells to be separated by spacers (Figure 3), both relaxing the joint rigidity limitation and permitting greater motions of type I members. The latter feature allows the implementation of a unit cell with a negative thermal expansion, so that, when averaged with the positive expansion of the spacer, the lattice has a zero or extremely low CTE. The joints are represented as circular flanges (Figure 2), having radius $R_1$ (for Type A, F, J) and radius $R_2$ (for Type B, C, D). The radius $R_1$ is defined as the convergence of struts of type AD and CJ, and $R_2$ by the convergence of struts of type AD with type BD and CD. The rigidity of the flanges reduces the effective length of the adjacent struts.

By considering the incremental changes in member length during thermal expansion, and eliminating the increment of $\theta$ we find for the original design of Figure 2,

$$\frac{\Delta L}{L} = \frac{\sqrt{3}\,\frac{\Delta L_1}{L_1} - \sin\theta\left(\cos\theta + \sqrt{3}\sin\theta\right)\frac{\Delta L_2}{L_2}}{\cos\theta\left(\sqrt{3}\cos\theta - \sin\theta\right)}, \tag{2.1}$$

where

$$L_1 = \frac{L}{2\cos\theta} \qquad (2.2) \qquad\qquad L_2 = \frac{L}{2}\left(1 + \sqrt{3}\tan\theta\right) \qquad (2.3)$$

and the symbol *Δ* followed by the letter *L*, with or without subscripts, indicates change of length. Since type II struts do not bend, but sustain only an axial load $T_2$, their strain is

$$\frac{\Delta L_2}{L_2} = \left(\frac{T_2}{E_2 A_2} + \varepsilon_2^t\right)\left(1 - 2\frac{R_2}{L_2}\right) + 2\hat{\varepsilon}_2^t \frac{R_2}{L_2}, \qquad (2.4)$$

where $E_2$ is Young's modulus for type II members, $A_2$ is their cross-sectional area, $\varepsilon_2^t$ is the thermal strain in the struts and $\hat{\varepsilon}_2^t$ is the effective thermal strain of joints of type D. Type 1 struts bend and stretch, and their axial strain is given by

$$\frac{\Delta L_1}{L_1} = \left(\frac{T_1}{E_1 A_1} + \varepsilon_1^t\right)\left(1 - \frac{R_1 + R_2}{L_1}\right) + \hat{\varepsilon}_1^t \frac{R_1}{L_1} + \hat{\varepsilon}_2^t \frac{R_2}{L_1}, \qquad (2.5)$$

where $T_1$ is the tension in these members, $E_1$ is Young's modulus for type I members, $A_1$ is their cross-sectional area, $\varepsilon_1^t$ their thermal strain and $\hat{\varepsilon}_1^t$ is the effective thermal strain of joints of type J.

Type I struts sustain a uniform shear force *V* and a non-uniform bending moment *M* (Figure 4). Equilibrium at joints A and D requires that,

$$T_1 = \frac{\cos\theta + \sqrt{3}\sin\theta}{\sqrt{3}\cos\theta - \sin\theta} V \,, \tag{2.6}$$

and,

$$T_2 = -\frac{2}{\sqrt{3}\cos\theta - \sin\theta} V \,. \tag{2.7}$$

Inspection of Figure 2 reveals that, by geometry, the transverse bending deflection of AD is given by

$$\delta = L_1 \Delta\theta = \frac{\Delta L_2 - \left(\cos\theta + \sqrt{3}\sin\theta\right)\Delta L_1}{\sqrt{3}\cos\theta - \sin\theta} \,, \tag{2.8}$$

while Euler-Bernoulli beam theory gives

$$\delta = \frac{V\left(L_1 - R_1 - R_2\right)^3}{12 E_1 I_1} \,, \tag{2.9}$$

where $I_1$, for type I members, is the 2nd moment of area of the cross-section about the neutral axis, so that $E_1 I_1$ is the bending stiffness of type I members, specified for bending in the plane of the lattice. Elimination of $\delta$ and $V$ among Eq. (2.6) – (2.9) provides

$$T_1 = \frac{12 E_1 I_1 L_1 \left(\cos\theta + \sqrt{3}\sin\theta\right)^2 \left(\frac{\Delta L_2}{L_2} - \frac{\Delta L_1}{L_1}\right)}{\left(L_1 - R_1 - R_2\right)^3 \left(\sqrt{3}\cos\theta - \sin\theta\right)^2} \tag{2.10}$$

and

$$T_2 = -\frac{24 E_1 I_1 L_1 \left(\cos\theta + \sqrt{3}\sin\theta\right) \left(\frac{\Delta L_2}{L_2} - \frac{\Delta L_1}{L_1}\right)}{\left(L_1 - R_1 - R_2\right)^3 \left(\sqrt{3}\cos\theta - \sin\theta\right)^2} \tag{2.11}$$

Use of Eq. (2.4) and (2.5) allows a solution for the strut tensions as

$$T_1 = \frac{12 E_1 I_1 L_1 \left(\cos\theta + \sqrt{3}\sin\theta\right)^2 \left(\varepsilon_2^t \frac{\hat{L}_2}{L_2} + 2\hat{\varepsilon}_2^t \frac{R_2}{L_2} - \varepsilon_1^t \frac{\hat{L}_1}{L_1} - \hat{\varepsilon}_1^t \frac{R_1}{L_1} - \hat{\varepsilon}_2^t \frac{R_2}{L_1}\right)}{\hat{L}_1^3 \left\{\left(\sqrt{3}\cos\theta - \sin\theta\right)^2 + \frac{12 I_1}{A_1 \hat{L}_1^2}\left[\frac{2 E_1 A_1 \hat{L}_2}{E_2 A_2 \hat{L}_1} + \left(\cos\theta + \sqrt{3}\sin\theta\right)^2\right]\right\}} \tag{2.12}$$

and

$$T_2 = -\frac{24 E_1 I_1 L_1 \left(\cos\theta + \sqrt{3}\sin\theta\right) \left(\varepsilon_2^t \frac{\hat{L}_2}{L_2} + 2\hat{\varepsilon}_2^t \frac{R_2}{L_2} - \varepsilon_1^t \frac{\hat{L}_1}{L_1} - \hat{\varepsilon}_1^t \frac{R_1}{L_1} - \hat{\varepsilon}_2^t \frac{R_2}{L_1}\right)}{\hat{L}_1^3 \left\{\left(\sqrt{3}\cos\theta - \sin\theta\right)^2 + \frac{12 I_1}{A_1 \hat{L}_1^2}\left[\frac{2 E_1 A_1 \hat{L}_2}{E_2 A_2 \hat{L}_1} + \left(\cos\theta + \sqrt{3}\sin\theta\right)^2\right]\right\}} \tag{2.13}$$

where the notation

$$\hat{L}_1 = L_1 - R_1 - R_2 \tag{2.14}$$

and

$$\hat{L}_2 = L_2 - 2R_2 \tag{2.15}$$

has been introduced. When these results are inserted into Eq. (2.4) and (2.5) and the outcome used in Eq. (2.3), the thermal expansion of the lattice becomes

$$\frac{\Delta L}{L} = \frac{\sqrt{3}\left(\varepsilon_1^t \frac{\hat{L}_1}{L_1} + \hat{\varepsilon}_1^t \frac{R_1}{L_1} + \hat{\varepsilon}_2^t \frac{R_2}{L_1}\right) - \left(\cos\theta + \sqrt{3}\sin\theta\right)\sin\theta\left(\varepsilon_2^t \frac{\hat{L}_2}{L_2} + 2\hat{\varepsilon}_2^t \frac{R_2}{L_2}\right)}{\left(\sqrt{3}\cos\theta - \sin\theta\right)\cos\theta}$$

$$+ \frac{12I_1\left(\cos\theta + \sqrt{3}\sin\theta\right)\left[\sqrt{3}\cos\theta + \left(3 + \frac{2E_1A_1\hat{L}_2}{E_2A_2\hat{L}_1}\right)\sin\theta\right]\left(\varepsilon_2^t \frac{\hat{L}_2}{L_2} + 2\hat{\varepsilon}_2^t \frac{R_2}{L_2} - \varepsilon_1^t \frac{\hat{L}_1}{L_1} - \hat{\varepsilon}_1^t \frac{R_1}{L_1} - \hat{\varepsilon}_2^t \frac{R_2}{L_1}\right)}{A_1\hat{L}_1^2\left(\sqrt{3}\cos\theta - \sin\theta\right)\cos\theta\left\{\left(\sqrt{3}\cos\theta - \sin\theta\right)^2 + \frac{12I_1}{A_1\hat{L}_1^2}\left[\frac{2E_1A_1\hat{L}_2}{E_2A_2\hat{L}_1} + \left(\cos\theta + \sqrt{3}\sin\theta\right)^2\right]\right\}}$$

(2.16)

When the bending stiffness is negligible ($I_1 = 0$), and the joint radii $R_1$ and $R_2$ are neglected, this result simplifies to Eq. (1.1).

The result in Eq. (2.16) highlights the two effects of bonded joints. The first involves the finite extent of the joints ($R_1$ and $R_2$ are non-zero), implied by the first term on the right hand side. The second arises because the bending of type I struts adds strain to the thermal response, signified by the second term on the right hand side.

Appropriate choices for the joint radii (Figure 2) are

$$R_1 = \frac{3w_1}{\pi - 6\theta} \tag{2.17}$$

and

$$R_2 = \max\left( \frac{3\left(w_1 + w_2\right)}{2\pi - 6\theta}, \frac{3w_2}{\pi} \right) \tag{2.18}$$

The thermal expansion for nodes A, J, F is

$$\hat{\varepsilon}_1^t = \varepsilon_1^t . \tag{2.19}$$

An appropriate choice for nodes B, C, D is a weighted average of the expansion of type I and II materials,

$$\hat{\varepsilon}_2^t = \frac{1}{3}\left(2\varepsilon_1^t + \varepsilon_2^t\right) \tag{2.20}$$

Results for the linear thermal expansion for various material combinations are plotted against $\theta$ in Figure 5, with a range of values for the bending stiffness parameter $I_1 / A_1 L_1^2$ used for illustration.

The above results affirm that the design of joints of Type A, J, F is critical to the realization of low thermal expansion behavior, because the low angle included between type I members from adjacent unit cells leads to excessively large $R_1$. This limitation is obviated by using an offset design wherein the centers of neighboring unit cells are displaced, allowing $R_1$ to become small even when $\theta \to \pi/6$ ( $R_1 \to w_1 / \tan(\theta + \pi/6)$ ). Such offset designs are achieved by insertion of a spacer made from type I material, as shown in Figure 3. The spacer removes the coupling of $\hat{L}_1$ and $\theta$, for a fixed L, enabling the use of larger values of $\theta$. Offset designs can have negligible bending, whereupon, the thermal expansion can be closely approximated by the first term on the right hand side of Eq. (2.16), with $R_1$ and $R_2$ neglected. The CTE for the offset lattice is thus:

$$\frac{\bar{\alpha}}{\alpha_1} = \frac{\sqrt{3} - \lambda F(\theta)}{\sqrt{3} - F(\theta)}\left(\frac{L}{L + \mathrm{H}}\right) + \frac{\mathrm{H}}{L + \mathrm{H}} \tag{2.21}$$

where H is the size of the spacer and $F(\theta) = \left(\cos\theta + \sqrt{3}\sin\theta\right)\sin\theta$. When H is zero, Eq. (1.1) is recovered once more. The formula in Eq. (2.21) can been used to guide low thermal expansion lattice designs, specifically, Eq. (2.21) predicts that zero thermal expansion of the lattice occurs when

$$\frac{\mathrm{H}}{L} = \frac{\lambda F(\theta) - \sqrt{3}}{\sqrt{3} - F(\theta)}. \tag{2.22}$$

This design has unit cells that contract upon heating, compensating for the expansion of the spacers. Such solutions are feasible when $\sqrt{3}/\lambda < F(\theta) < \sqrt{3}$ (Note that, within this range, the unit cell has negative thermal expansion). The upper limit of this range coincides with $\theta = \pi/3$. For illustration, when $\lambda = 2$, the lower limit is $\theta = \pi/6$. Beyond these limits is the requirement that joints A, J, F remain physically small, requiring that $H \geq \sqrt{3}w_1 \sin\theta / F(\theta)$: whereupon the type I elements from neighboring unit cells have no intersection. From Eq. (2.22), this requirement provides

$$\frac{w_1}{L} \leq \frac{\left[\lambda F(\theta) - \sqrt{3}\right] F(\theta)}{\left[\sqrt{3} - F(\theta)\right]\sqrt{3}\sin\theta}, \tag{2.23}$$

revealing that the slenderness of type I elements has to be respected. Consequently, when $\theta = \pi / 6$, Eq. (2.23) gives $w_1 / L \leq (\lambda - 2)$, indicating that the design can be satisfied provided that $\lambda = \alpha_2 / \alpha_1 > 2$, ensuring that $w_1$ is positive. Moreover, any material combination with $\lambda$ slightly in excess of 2 (say more than 2.1) is acceptable, since $w_1 / L$ must be small to ensure low bending stiffness.

Alternatively, Eq. (2.23) can be recast as a condition on $\theta$ with $\lambda$ and $w_1 / L$ already selected. The outcome is not transparent since it involves a combination of trigonometric functions of $\theta$ without obvious simplification. Nevertheless, inspection indicates that any $\theta$ slightly above the lower limit ($F(\theta) = \sqrt{3} / \lambda$) will satisfy Eq. (2.23). Specific cases should be assessed numerically to ensure a satisfactory design, as elaborated below.

A chosen design is limited in its range of temperature operation by the requirement that the triangle of type II elements has space into which material can expand when the lattice is heated. The critical condition occurs when joint C (Figure 2) touches its counterparts from the two adjacent unit cells. It is straightforward to ascertain that the strain increment in type II bars that causes this critical condition is

$$\varepsilon_2^t = \frac{\cos\theta - \sqrt{3}\sin\theta + \frac{2\mathrm{H}}{L}\cos\theta}{\cos\theta + \sqrt{3}\sin\theta} \tag{2.24}$$

Consequently, the operating temperature range must be chosen to ensure that thermal straining of type II elements is smaller. For $\theta \sim \pi/6$ and greater a careful choice of H/L is needed, since $\cos\theta - \sqrt{3}\sin\theta \leq 0$ for $\theta \geq \pi/6$ .

## *3. Specific, Low Expansion, Offset Designs*

### 3.1 FE Method

Lattices are modeled using a representative volume element (RVE) FE technique. Three-dimensional models are subject to periodic boundary conditions for the two in plane dimensions in the form of uniform macroscopic strains. The relative displacements between pairs of boundary nodes are controlled by tying their displacements together consistent with the strains we wish to impose[8, 9]. The third, $z$-direction, is left free. A single node on the interior of the model is held fixed in space to prevent rigid-body translations. The commercial FE code ABAQUS [10] is used for mesh generation and to perform analysis. MATLAB [11] code is used extensively to manipulate meshes, apply boundary conditions, and for post processing. Periodic boundary conditions were implemented in Cartesian coordinates. A typical RVE is pictured in Figure 6. Typical meshes consist of ~20,000 to ~70,000 8-noded linear hexahedral elements (type C3D8R). The number of elements varies greatly with the relative density of the lattice geometry being analyzed, which ranged from 8% to 98% for slender to space-filling designs, respectively. Mesh sensitivity is studied to ascertain model resolution at which solutions converge. Because the average strains are small, there is no distinction between the macroscopic Cauchy stress and the macroscopic nominal stress, so that the macroscopic stress can be computed by simply dividing force resultants by section areas for the undeformed volume of the RVE

### 3.2 Offset Lattices

In stretch dominated structures, where loads are well distributed, stress contours are rather uniform, and consequently the structure is relatively efficient in its utilization of material. On the other hand, FE calculated thermomechanical stress distributions in the original lattice design reveal large nonuniform bending stresses associated with rigidity and member intersection at the joints (Figure 7a). The lattices analyzed to obtain these results are modeled with the temperature dependent properties of Ti and Al alloys listed in Table I-b and subject to a temperature excursion from 40C to 250C. The bimaterial interface, in reality press-fit, is considered to be perfectly bonded for simplicity. Simulations that model the interface between sublattices with contact in compression, and a frictional coefficient of $\mu$=1 give results that are negligibly different from welded models. The maximum tensile equivalent stress (also known as the von Mises stress) is located in the bimaterial joint region and results from CTE mismatch between constituents. In the temperature range analyzed, the maximum tensile equivalent stress is lower than the tensile yield stress in both materials.

Constraints on the motion of the lattice's components drive the macroscopic CTE towards that of the constituents. By placing a spacer (Figure 3), with characteristic dimension H, between unit cells and eliminating excess material around the bimaterial joint, the lattice geometry can be designed so that it behaves according to the original concept for low CTE, *i.e.* with negligible stress (Figure 7b). Contours for the revised design show greatly reduced bending stresses and the overall lattice behavior is in good agreement with new analytical predictions (Figure 8).

### 3.3 Lattice Design

For any pair of constituent materials and their associated properties there is a range of skew angles, $\theta$, over which a desired lattice CTE can be achieved. Properties such as stiffness, Poisson's ratio, and strength vary over this range so that any one solution may be superior to others depending on design requirements. For a unit temperature change, $\Delta T = 1$, so that $\varepsilon_i^t = \alpha_i$, Eq. 2.16 gives the thermal expansion coefficient of the lattice and can be inserted into Eq. 3.1,

$$\bar{\alpha} = \frac{\Delta L + \mathrm{H}\alpha_1}{L + \mathrm{H}} \tag{3.1}$$

to calculate the expansion of a spaced lattice. The macroscopic thermal strain in a spaced lattice is the weighted sum of the lattice and spacer strain, the latter having thermal expansion coefficient $\alpha_1$. Eq. 3.1 can be used to identify regions of design parameter space where lattices with the desired thermomechanical response exist. Designs in this neighborhood can then be investigated through FE to address specific geometries and to investigate their thermomechanical response in comparison to the results in Section 2.

The thermomechanical strain response of the bimaterial joints in Eq. 2.20 is assumed to be the average of the constituents. While this approximation is sufficient for exploratory investigations, specific mechanical bimaterial interface geometries must be considered when designing real structures, as their behavior may differ substantially from this idealization. The dovetail joint employed by Steeves *et al.* [5,7], and in the current effort, are examples of bimaterial attachments. Mechanical connections capable of carrying tensile loads are necessary for transmitting all applied macroscopic loading situations except biaxial tension. The size of these joints, given by their characteristic dimension, $R_2$, reduce the effective length of members ($\hat{L}_1$ and $\hat{L}_2$, Eq. (2.14) and (2.15)).

For fixed values of $w_1$ and $w_2$ the thermomechanical response of the system is a strong function of the member effective lengths, and therefore of $R_1$ and $R_2$. In many designs a single radius $R_2$ does not exist by which both type I and II members are reduced equally at the Type D joints (Eq. (2.14) and (2.15)). The actual reduction in effective length of members at these nodes is a function of member width and the relative angle at which they are incident to the joint. To identify designs with a tailored and well predicted CTE which is amenable to fabrication more detailed modeling is necessary.

The addition of the spacer (Figure 3) allows practical access to previously unachievable skew angles and corresponding higher relative densities. In previous designs without the spacer, at skew angles approaching 30°, members from adjacent unit cells intersect to an extent, and prevent the desired thermomechanical response, and the desired CTE cannot be realized. A skew angle of 30°, without a spacer present, results in type 1 members in adjacent cells being parallel and a hexagonal unit cell appearance. If only the area bounded by the unit cell is considered, these designs can achieve near maximum areal density as an assembly of hexagonal cells with small gaps between them. The size of the gaps between unit cells is directly related to the size of the spacer H. Upon temperature excursion from the reference state, type I members expand, distort and rotate, causing Type D nodes to translate away from the center of the unit cell. The size of the spacer and the corresponding gap is dictated by the maximum outward deflection of these nodes in the specified temperature range combined with the need to avoid adjacent unit cells impinging upon each other after thermal straining. For some designs with skew angles near or above 30° an upper use temperature exists at which initially nearly parallel type I members in adjacent cells deform to contact each other causing the lattice to densify. For these designs the upper use temperature can be increased by expanding the size of the spacer at the cost of driving the CTE of the system towards that of the type I material (Eq. (3.1)). Densification may also significantly influence the stiffness and strength of these lattices and may be a beneficial feature in some applications. If material continuity is beneficial, such as for aerodynamic surfaces, densified lattices can be useful.

In some spaced lattice designs where the dimension of the spacer is on the order of $w_1$, no additional material is need to achieve this offset. In others designs with skew angles in the neighborhood of 30° unit cells may intersect minimally or not at all (Figure 3) and the strength and stiffness joint will suffer. A disk of material centered on the spacer, a stiffener with radius $S_r$ can be added to the lattice to maintain continuity and transmit stresses between unit cells. If the disk of material is too small, stress concentrations in these regions can be design limiting. An appropriate radius for this disk is one where axial loads in type 1 members can be directly transmitted to adjacent cells (Figure 3 c and d). This stiffener has a dimension independent of the spacer and may be useful in facilitating a connection between the lattice and a substructure.

As type II members are not subject to thermally induced bending stresses, members with geometries other than truss or beam like forms can be considered without altering the mechanics of the system [5]. In Figure 10 the lattices pictured in the middle and on the right (b and c) are variations of the lattice on the left (a) incorporating type II members that are not simple prismatic beams. Stiffening of type II members drives the thermal expansion of the system to lower values. The increased stiffness of these members can be modeled by using an effective modulus $E_2$* for $E_2$ in Eq. (2.12) and Eq. (2.13). The only restriction in geometry is that the type II members not impinge on, and reduce the effective length of the slender type I members when thermomechanically strained. Previous fabricated designs have used truss and solid triangular inner type II members (Figure 9 a and b) [5,7].To explore the potential space-filling properties of this lattice a hexagonally shaped type II sublattice geometry was chosen for fabrication in this work.

If in plane geometries of members are specified to have a finite width centered on the lines shown in Figure 2 the width the bimaterial joint is limited by the width of type II members, $w_2$ (for the geometry considered in this work). Selecting a small bimaterial joint resulted in a small value of $w_2$ in Eq. (2.16). To account for the much larger cross-section of the hexagonal geometry used an effective modulus of $E_2^* = 10\,E_2$ is utilized in the analytical model. The order of magnitude increase in stiffness is an estimate; further increases do not significantly influence results. By choosing a slightly skewed, but nearly hexagonal type II element, an upper use temperature densification event can be engineered between high and low CTE sublattices. When both adjacent unit cells and sublattices contact each other at the same $\Delta T$, a nearly or completely densified and continuous structure can be formed.

The dovetail joint dimensions were chosen to maximize the effective length of type I members. Joint dimensions were minimized to reduce $R_2$ with practical consideration for the interface size and the need to maintain a robust mechanical connection between sublattices. Lattices previously investigated [5, 7] used dovetail joints where the high CTE type II material composed the inner, male side of the connection. Additional material was added to the lattice at these locations to help facilitate a robust connection. This added material served to reduce the effective length of members resulting in a poorly predicted thermal response (Figure 8). In the current design the inner male component is now composed of the low CTE type I material, and the bimaterial joint is relocated to be enclosed in the inner type II member. Switching the low CTE material to the male side reduces thermal stresses resulting from the expansion of the high CTE material, which previously confined the low CTE constituent. It is hoped that plasticity can be avoided altogether with this configuration, in contrast to the previous dovetail joint design.

The test specimen designed and fabricated in this work was chosen to have a skew angle of 30° and nearly space filling inner type II member. By specifying the geometric parameters $w_1$=3.0mm, $w_2$=0.4mm, $\theta$=30°, H=2.0mm, $S_r$=3.80mm, and unit cell length L=50.0mm, the designs in Figure 10 are achieved. Finite element and analytical predictions for the geometries shown are listed in Table II.

### 3.4 Lattice Fabrication

A metallic lattice was fabricated for CTE measurement purposes. The type I lattice was electro discharge machined from 3mm thick sheets of Ti-6Al-4V. The type II members were machined from 7075-T6 aluminum alloy. Sublattices were press-fit together. Tolerances were such that assembly with hand pressure was possible; however a mechanical press was used to ensure proper assembly. The structure consists of 10 unit cells arranged so that two cells in the interior are separated from the edge by another unit to minimize edge effects (Figure 10).

### 3.5 CTE Measurement Methodology

Thermal expansion measurements on the Ti and Al lattice were performed using a 2-D digital image correlation (DIC) system. A high contrast black and white speckle pattern was applied using spray paint. Lattices were heated on a laboratory hot plate (Wensco, model# H1818RA4000) at a rate of 60C/hr from room temperature to 220C. A frame of common silica insulation, approximately 1.5in thick, was placed around the lattice with a glass plate on top. The temperature was recorded by four self-adhering K-type thermocouples (Omega, model# SA1XL-K-SRTC) located on the upper face of the lattice, two each on Ti and Al. Acetone was used to remove the applied paint at the location of the thermocouple attachments to increase heat transfer. The temperature of the lattice was taken to be the average of the four. Digital images were captured by CCD camera (AVT Dolphin F-201B) with a zoom lens (Tamron AF 70-300 1:4-5.6) positioned approximately 2 m from the specimen. The focal length was maximized subject in the confines of the laboratory space to minimize the effect of out of plane deformations on in plane measurements. Images were taken every five seconds to record deformations. Two 300W incandescent lights in hoods were positioned close above the glass plate for imaging purposes. Using the Vic-2D (Correlated Solutions) software, virtual extensometers placed on the reference image, and tracked through the images, measured the displacement between pairs of pixel subsets. A typical area of interest consisted of one unit cell with three Type D nodes visible. Strains were calculated from the relative displacement between pairs of subsets which were typically $23^2$ pixels. Strains were measured in the Al and Ti and were calculated as the average of 6 virtual extensometers. Lattice strains were calculated as the average of three virtual extensometers placed between the three Type D nodes surrounding an interior unit cell. Temperature average CTE was measured by linear fitting to strain-temperature plots where the average CTE over the temperature range is the slope of the resulting straight line. Extensometers were placed upon relatively unstressed material regions to measure the CTE of the constituents.

Image distortion from convective currents emanating from the specimen is a common problem when using DIC to record thermomechanical strains. A frame of silica fiber insulation was placed around the lattice and a glass plate on top to help thermally isolate the specimen from the camera. A fan is used to mix the air directly above the glass plate and carry hot air away from the lights.

### 3.6 CTE Results

A typical experimental strain versus temperature plot is shown in Figure 11 along with FE prediction. Temperature average CTE for the lattice and the constituent materials is reported in Table III. Although the DIC software is capable of measuring microstrains, scatter on the order of 1000 microstrain was present in the measurements due to image distortion. Convective currents emanating from the lighting were sufficient to cause visible inhomogeneous lensing in successive images. Measurements on the Ti were limited to the Type D joints resulting in short gauge lengths and larger scatter.

The average value of CTE for the constituent materials is measured to be ~4% higher than reported values (24.3 ppm/C for Al, and 9.4 ppm/C for Ti) (Table I-a), but are within experimental error. The lattice has an average measured CTE of -0.9 ppm/C that is well predicted by FE of -1.1 ppm/C, and close to the analytical prediction of -1.4 ppm/C.

## 3.7 Discussion – Thermal Expansion

Measured thermal expansions of the lattice agree well with analytical and FE predictions. Differences between measured and FE prediction are believed to be due to the reduced effective length of the type I members resulting from fabrication imperfections causing premature contact between sublattices. The hexagonally shaped aluminum members had visible machining imperfections on some edges where they were cut from stock. The small wing-shaped gap between high and low CTE members results in a structure that is more imperfection sensitive than a lattice with triangular or prismatic beam type members. Geometric imperfections in this gap can cause sublattices to impact each other before the predicted upper use temperature, reducing the effective length of type I members and driving up the

CTE. Space-filling lattices with these features, such as aerodynamic surfaces, may be adversely affected by debris in these small gaps.

No plasticity is predicted in the revised dovetail geometry. The limited plasticity present in other designs [7] was a function of the bimaterial joint geometry employed and is not inherent to the functional mechanics of the lattice itself.

Scatter in CTE measurements results from several sources. Convective currents in the air column between the specimen and the camera distort images through their associated density gradients and lensing effects [12]. Efforts were made to mitigate convective currents coming from the specimen and hotplate, but the incandescent lighting used for imaging proved a sufficient source of interference. A cold light source or a camera orientation that minimizes the effect of convective currents, by positioning it outside the affected area, would reduce the effect. The large scatter in the CTE measurements for Ti is due to the lattice geometry studied, the size of the unit cells, and the short lengths of relatively unstressed material available for measurements taken in the Type D node region.

The analytical model developed in Section 2 does a good job of predicting lattice thermal expansion. The model uses the simple assumption that the thermal expansion of the Type 2 joint region is a weighted average of the constituent materials (Eq. (2.20)). In reality a distinct material interface exists between the constituents, and the thermal response is much more complicated. The analytical CTE prediction of -1.4 ppm/C for the lattice is close to the FE predicted value of -1.1 ppm/C and sufficiently accurate to help characterize the design space to locate geometries of interest.

CTE measurements performed on a titanium and aluminum lattice using 2-D DIC were able to validate the analytical and FE predictive models used in its design. The metal lattice behaved elastically over a temperature range of 175C, exhibiting consistent negative thermal expansion. The design space identified through the analytical model suggests the ability to realize a family of structures with a wide range of stiffness and thermal expansion properties.

## *4. Stiffness*

### 4.1 Basic Stiffness Results for Pin-Jointed Lattices.

***Elastic properties.*** The unit cell of the design without spacers is shown in Figure 12-a is loaded by a set of forces, parameterized by $P$, $Q$ and $S$. It is presumed that the lattice has been designed in the manner described above, such that the bending stiffness of struts of type I are very low, whereupon their behavior is stretch dominated. In such a situation, the lattice can be analyzed as if it were pin-jointed.

The resulting behavior is isotropic in the plane of the lattice, and stated as

$$\varepsilon_{xx} = \frac{\sigma_{xx}}{E} - \frac{\nu\sigma_{yy}}{E} + \alpha\Delta T \tag{4.1a}$$

$$\varepsilon_{xx} = \frac{\sigma_{xx}}{E} - \frac{\nu\sigma_{yy}}{E} + \alpha\Delta T \tag{4.1b}$$

$$\varepsilon_{xy} = \frac{\sigma_{xy}}{2G} \tag{4.1c}$$

where *E*, $\nu$, *G* and $\alpha$ are the in-plane Young's modulus, Poisson ratio, shear modulus and coefficient of thermal expansion, respectively, of the lattice.

The biaxial stiffness is the ratio of the biaxial stress to the in-plane strain under equibiaxial loading [5], and can be deduced as

$$S_b = \frac{\left(\sqrt{3}\cos\theta - \sin\theta\right)^2}{2\sqrt{3}L_1\left[\frac{1}{E_1 w_1} + \frac{2\sin^2\theta}{3E_2 w_2}\left(\cos\theta + \sqrt{3}\sin\theta\right)\right]} \tag{4.2}$$

[Note that this corrects a misprint in the previously published formula in [5] which is missing the leading 2 in the denominator]. The shear modulus is

$$G = \frac{\left(\sqrt{3}\cos 2\theta + \sin 2\theta\right)^2}{8\sqrt{3}L_1\left[\frac{1}{E_1 w_1} + \frac{2\sin^2 2\theta}{3E_2 w_2}\left(\cos\theta + \sqrt{3}\sin\theta\right)\right]}. \tag{4.3}$$

In these expressions for $S_b$ & $G$, $L_1$ is used rather than $L$ since $L_1/w_1$ is the aspect ratio of type I elements.

The Poisson ratio for the lattice may be computed from

$$\nu = \frac{S_b - 2G}{S_b + 2G} \tag{4.4}$$

and the Young's modulus is

$$E = 2G\left(1 + \nu\right) \tag{4.5}$$

Note that, in certain circumstances, the Poisson ratio will be zero or negative. For example, when $E_2 >> E_1$, the Poisson ratio reduces to

$$\nu = \frac{\cos 2\theta - \sqrt{3}\sin 2\theta}{3 + 2\left(\sqrt{3}\cos\theta + \sin\theta\right)\sin\theta} \tag{4.6}$$

As a consequence, it is zero at $\theta = \pi/12$, and negative for $\theta > \pi/12$.

The introduction of a stiff spacer, as in Figure 3, has no effect on the elastic properties of the lattice. If the spacer is a stiff component (*e.g.* composed of a solid plate rather than a set of truss or beam elements), the elastic properties of the lattice are still given by the values in Eq. (4.2) & (4.3). This situation arises because for a stiff spacer, when we neglect its deformation and treat it has rigid, both stress and elastic strain scale in the same way with the size of the spacer. To show this for the case of equibiaxial stress, the loads in Figure 12 b are

$$P = (L + \mathrm{H})\sigma_B \tag{4.4a}$$

$$Q = \frac{\sqrt{3}}{2}(L + \mathrm{H})\sigma_B \tag{4.4b}$$

where $\sigma_B$ is the applied biaxial stress. Because the spacers are rigid the forces experienced by the adjacent nodes are the same. The stresses are

$$\sigma_{11} = \frac{2Q}{\sqrt{3}L} \tag{4.5a}$$

$$\sigma_{22} = \frac{P}{L} \tag{4.5b}$$

And the change in dimensions of the lattice are

$$\Delta u_1 = \varepsilon_{11} L = \frac{1}{E}\left[\frac{2Q}{\sqrt{3}} - \nu P\right] \qquad (4.6a)$$

$$\Delta u_2 = \varepsilon_{22} \frac{\sqrt{3}L}{2} = \frac{\sqrt{3}}{2E}[P - \nu Q] \qquad (4.6b)$$

The strains are

$$\bar{\varepsilon}_{11} = \frac{\Delta u_1}{L+\mathrm{H}} \qquad (4.7a)$$

$$\bar{\varepsilon}_{22} = \frac{2\Delta u_2}{\sqrt{3}(L+\mathrm{H})} \qquad (4.7b)$$

Using (4.4), (4.5) and (4.6), with (4.7), the strains become

$$\varepsilon_{11} = \varepsilon_{22} = \frac{1}{E}[\sigma_b - \upsilon\sigma_b] \qquad (4.8)$$

Showing that the strains are not a function of the size of the spacer.

For the case of shear loading for a lattice with spacer with an applied shear stress τ, the forces in Figure 12 b are

$$P = (L + H)\tau, \tag{4.9a}$$

$$Q = \frac{-\sqrt{3}}{2}(L + H)\tau, \tag{4.9b}$$

Because the spacer is rigid, the resulting macroscopic strains are

$$\bar{\varepsilon}_{11} = \frac{1}{E}\left[\frac{Q}{\sqrt{3}(L+H)/2} - \nu\frac{P}{L+H}\right] = \frac{1}{E}[-\tau - \nu\tau], \tag{4.10a}$$

$$\bar{\varepsilon}_{22} = \frac{1}{E}\left[\frac{P}{L+H} - \nu\frac{Q}{\sqrt{3}/2(L+H)}\right] = \frac{1}{E}[\tau + \nu\tau]. \tag{4.10b}$$

This indicates that there is no stiffness penalty upon introduction of a stiff spacer.

## 4.2 In-Plane Compression Measurements

In-plane compression experiments have been used to generate stress/strain measurements. The objectives are twofold. (i) Allow calibration of the mechanical robustness and stiffness of representative lattices. (ii) Provide validation data for the ensuing finite element calculations. For these purposes, it suffices to fabricate lattices from 1mm thick plates by laser cutting. To probe the yielding and strain hardening characteristics, one set of lattices has been generated from 304 Stainless Steel. During testing, out of plane buckling was prevented by constraining the lattice between two 12.7 mm thick tempered glass plates, bolted to an aluminum frame. The experiments were performed in an MTS$^{TM}$ 810 servo-hydraulic testing system under displacement control, using a displacement rate of 0.5 mm/min. Images of the lattice were recording every 15 seconds during the tests using a CCD camera connected to an image correlation system.

Two different type II member geometries were used. The stress-strain behaviors, shown in Figure 14, reveal robust behavior, characterized by yielding followed by strain hardening. In all cases, yielding occurs in the type I members at critical stress levels in the range, $15 \le \sigma_c \le 18 MPa$ . The bright regions in the images (Figure 13) indicate the occurrence of out-of-plane plastic buckling. Unload-reload measurements reveal hysteresis and decreasing stiffness with increase in plastic strain.

## 4.3 Experimental and Finite Element Results

Stress strain curves generated from finite element modeling (FEM) are plotted alongside experimental results in Figure 14. The 304 Stainless Steel was modeled by linear elastic response followed by yielding with isotropic hardening. Twenty node biquadratic elements (C3D20R) were used in these calculations. Homogeneous strains were applied to the RVE in the 2-direction. The influence of the glass plates used to confine specimens out of plane was not modeled.

Notable features of the experimental stress-strain curves include a reduction in elastic stiffness with increasing strain past initial yield as evident in the unload-reload regions, and significant hysteresis in these regions. No reduction in stiffness is seen in models restricted to in plane deformations. Models seeded with imperfections to initiate buckling show the same reduction in stiffness with strain as experiments. Frictional interactions between the lattices and the glass plates used to constrain out of plane motion are attributed as the source of hysteresis observed in experiment. The collapse modes, plastic buckling of type I members oriented most obliquely to the loading direction, and out of plane plastic hinging in the same yielded members, are accurately captured by the FE results (Figure 15).

### 4.4 Comparison of Pinned and Bonded Stiffness

To compare pin-jointed analytical and FE bonded predictions for stiffness, the equations in Section 2 were used to identify lattice geometries with zero thermal expansion and maximum stiffness. For a given skew angle $\theta$ and lattice unit cell length $L$, Eq. (2.16) can be used to identify values of $w_1$ and $w_2$ that produce maximum stiffness for a given pair of constituent materials. Using the temperature average properties of Ti and Al (Table I-a) a variety of zero CTE lattices as predicted by Eq. (2.16) are identified (Figure 16). The associated aspect ratio of type I members, $\hat{L}_1/w_1$, decreases with increasing skew angle from 20.4 to 5.0 (Figure 16 a-d). The stiffness of the analogous pin-jointed structures, those having the same member dimensions, are plotted along with FEM results in Figure 17, where $V_{f,i}$ is the fraction of solid material of type i.

## 4.4 Discussion – Stiffness

Experimental and FE results for 304 steel lattices in axial compression show that the geometries tested are prone to out of plane deformations, suggesting relatively good in plane properties. FE analysis of an RVE shows good agreement with experiments conducted on steel lattices. To avoid the complex loading interactions between glass plates used to confine test specimens thicker lattices not prone to out-of-plane plane deformations should be tested. Lattices incorporated into other structures and attached at nodal locations will have reduced out of plane degrees of freedom, such as when they are used as the face-sheet in a sandwich panel, and will also be less prone to buckling in this manner. Additional boundary conditions or structural elements within the RVE technique can be used to model the behavior of more confined lattices.

Analytical models for pin-jointed biaxial stiffness and CTE give results that are similar to those from FE analysis of bonded lattices with slender members. Bonded lattices have increased CTE and stiffness over analytical predictions at higher relative densities. Decreasing member slenderness causes more overlap of members near joints leading to potentially larger deviations from the assumptions in Section 2 regarding the thermomechanical response of the joint region. Beam theory cannot accurately predict the deformation of members with aspect ratios less than about 10; in this case Ti and Al lattices with $\theta$ greater than ~26°. However the associated geometries still have a CTE very close to the value predicted by Eq. (3.1). Stress distributions in lattices subject to equibiaxial tensile straining show greater uniformity at lower relative densities suggesting more efficient and stretch dominated behavior. The stiffness of the pin-jointed lattice is clearly recovered in bonded lattices with slender members as predicted in Section 2.

When optimized for maximum biaxial stiffness this lattice geometry can achieve a large fraction of theoretical bounds (Figure 18). Theoretical bounds on stiffness for composites with a given effective thermal expansion coefficient [3] are plotted for twelve lattice geometries and their associated compositions. At effective CTEs near the rule of mixtures, a value of 1.0 in this plot, denser structures have a higher potential for stiffness as indicated by the yellow and light purple lines. At large deviations in effective CTE a substantial amount of bending is required to accommodate the local thermal strains, degrading the potential stiffness by more than a factor of ten relative to a bilayer of identical composition. In the case where the lower CTE constituent is more compliant than the higher CTE constituent the ability of the UCSB lattice to achieve theoretical bounds is reduced. When composed of a high temperature nickel alloy, Haynes 188, and a niobium alloy, the theoretical bounds on stiffness are ~5% of that of a bilayer with identical composition when the effective CTE is near zero.

## *5. Concluding remarks*

Modifications to the geometry and modeling assumptions of previous bonded lattice designs of the UCSB lattice have resulted in a design scheme capable of rapidly identifying geometries that inherit the CTE and stiffness properties of the parent pin-jointed structure. The pin-jointed structure has been shown to be near optimal in stiffness over a wide range of densities [4]. Similar bonded lattices have obvious advantages in terms of fabricability. The behavior of these lattices is elastic and amenable to fabrication on length scales ranging from aerospace structures to those relevant to nanotechnology.

The behavior of the bonded structure tends towards that of the pin-jointed lattice at lower relative densities in maximum stiffness lattices having slender members. At higher densities lattice members have aspect ratios too low for beam-theory based models to accurately predict their behavior. CTEs in these structures are still significantly different from the mean of the constituents. Three-dimensional computer aided design (CAD) and FE can be used to identify and fabricate rigid-jointed lattices with a tailored thermal expansion coefficient that is well predicted by modeling.

A lattice composed of Ti-6Al-4V and 7075-T6 Al was designed, fabricated and measured to have a negative thermal expansion coefficient. Design space illustrated by the analytical model developed in this work shows the possibility for realizing material systems with a wide range of CTE including significantly negative thermal expansions. Such negative CTE materials can be used in a limited capacity in systems composed mostly of more conventional positive CTE materials as space filler. The demonstrated ability of this design approach opens the door for the investigation and application of a wide family of materials with novel properties including high stiffness and low thermal expansion.

Further extension of these analytical and numerical techniques can be used to investigate the introduction of anisotropy by allowing geometry to vary amongst members of the same type in a unit cell allowing properties to be tailored in two directions. Rapid prototyping and other direct fabrication techniques can be used to fabricate volumetric lattices with properties tailored in three dimensions. The analytical and FE techniques can be extended to consider these variations

Possible combinations lattice constituent materials include ceramics, glasses, and glass ceramics. In high temperature applications the thermal strains in these materials can be tailored to match the thermal strains experienced in significantly cooler supporting substructures. A low CTE glass, such as Zerodur, used as the type 1 material will offer a large CTE ratio, $\lambda\lambda$, when paired with a wide range of other higher expansion materials making available a wide range of achievable CTE (Figure 5).

Theoretical bounds on stiffness for these types of composites indicate a large tendency for bending when the effective CTE is a large deviation from the rule of mixtures of the constituents, being ten to twenty times more compliant than a bilayer of identical composition perhaps limiting the use of these structures in critical structural applications.

Other considerations exist in the design of these systems. These include: (i) Transient heating effects resulting from mismatches in thermal conductivity between constituents, and non-uniform heating (ii) The net CTE of the lattice is a function of the relative thermal strain between sublattices which may be varying due to transients and inhomogeneous thermal loading which can affect the response (iii) Aerodynamic surfaces are often curved surfaces so that non-flat shapes with a tailored thermal expansion coefficient may be desired. The techniques developed and exercised in this paper can be extended to address these issues, and the strength and failure modes of systems can also be addressed.

### *Acknowledgments*

This research was supported by the Office of Naval Research through the MURI program “Revolutionary Materials for Hypersonic Flight,” (Contract N00014-05-1-0439).

### *References*

[1] R.S. Lakes, “Cellular solid structures with unbounded thermal expansion,” *Journal of Materials Science Letters* **15** pp. 475-477 (1996).

[2] O. Sigmund and S. Torquato, “Composites with extremal thermal expansion coefficients,” *Applied Physics Letters* **69** pp. 3203-3205 (1996).

[3] L.V. Gibiansky and S. Torquato, “Thermal expansion of isotropic multiphase composites and polycrystals,” *Journal of the Mechanics and Physics of Solids* **45** pp. 1223-1252 (1997).

[4] G Jefferson, T. A. Parthasarathy and R. J. Kerans, “Tailorable thermal expansion hybrid structures,” *International Journal of Solids and Structures* **46** pp. 2372–2387 (2009)

[5] C.A. Steeves, S.L.Lucato, M.Y. He, E. Antinucci, J.W. Hutchinson and A.G. Evans, “Concepts for structurally robust materials that combine low thermal expansion with high stiffness,” *Journal of the Mechanics and Physics of Solids* **55** pp. 1803-1822 (2007).

[6] J.N. Grima, P.S. Farrugia, R. Gatt and V. Zammit, “A system with adjustable positive or negative thermal expansion,” *Proceedings of the Royal Society A* **463** pp. 1585-1596 (2007).

[7] C.A. Steeves, C. Mercer, E. Antinucci, M.Y. He and A.G. Evans, “Experimental investigation of the thermal properties of tailored expansion lattices,” *International Journal of Mechanics and Materials Design)* **5** pp. 195–202 (2009)

[8] M. Danielsson, D. M. Parks and M. **C. Boyce, “**Three-dimensional micromechanical modeling of voided polymeric materials,” *Journal of the Mechanics and Physics of Solids* **50** pp. 351-379 (2002)

[9] K. Bertoldi *(discussion)* Harvard University, School of Engineering and Applied Sciences

[10] ABAQUS 6.9-EF Providence, RI: Simulia, 2009

[11] MATLAB 2008b Natick, MA: Mathworks, 2008

[12] M. A. Sutton, J. J. Orteu and H. W. Schreier, “Image Correlation for Shape, Motion and Deformation Measurements ,” *Springer.com* (2009)

## *Chapter I Figures*

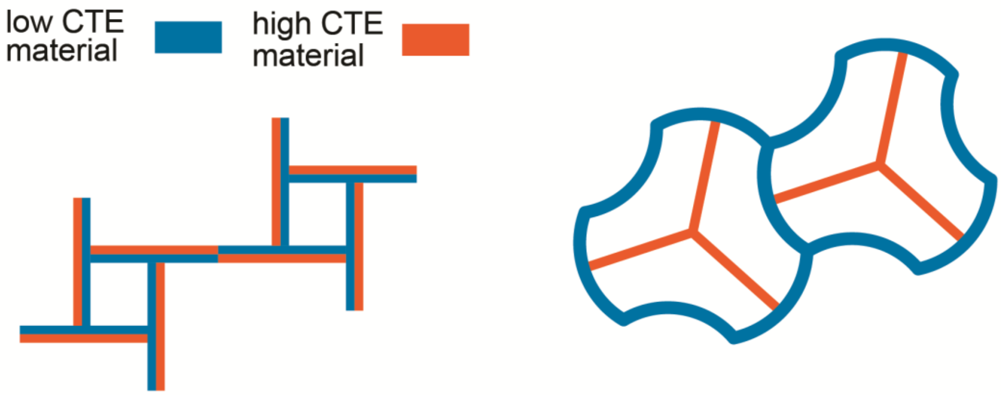

(a) Lakes lattice (c) AFRL lattice

(b) Topology optmization (d) UCSB lattice

**Figure 1 - Concepts for low thermal expansion lattices; (a) the Lakes lattice [1]; (b) the lattice obtained by topology optimization [2, 3]; (c) the AFRL design [4]; (d) the UCSB lattice [5].**

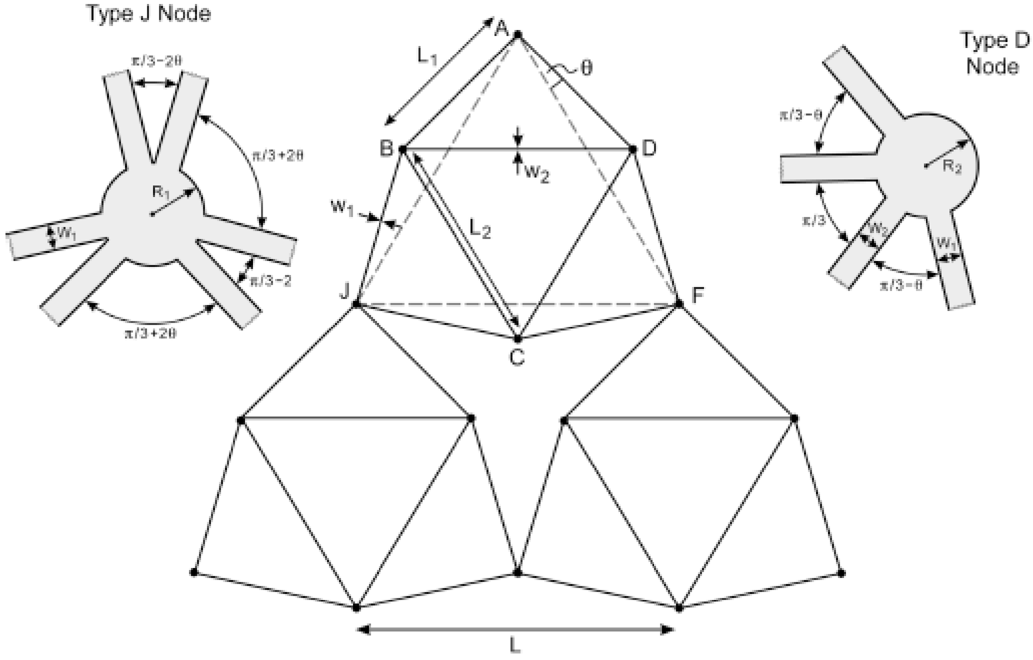

**Figure 2 - Unit cell and joint geometry.**

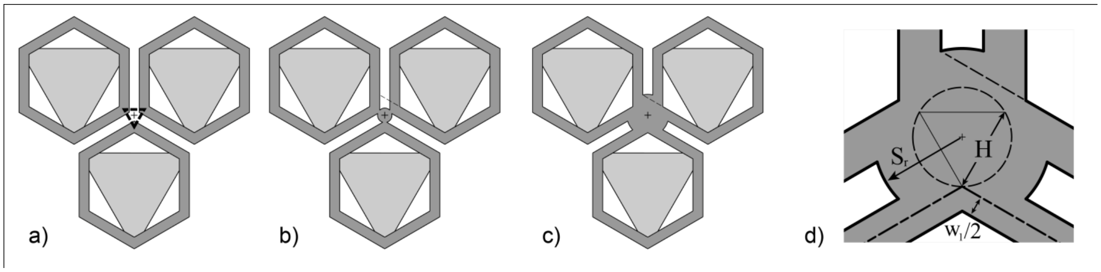

**Figure 3 - Spaced lattices with $\theta = \pi/6$, with no additional material (a), undersized stiffener (b), and appropriately sized spacer (c and d) where axial member loads can be transmitted directly to adjacent unit cells. Spacer has characteristic dimension H while the stiffener has radius $S_r$.**

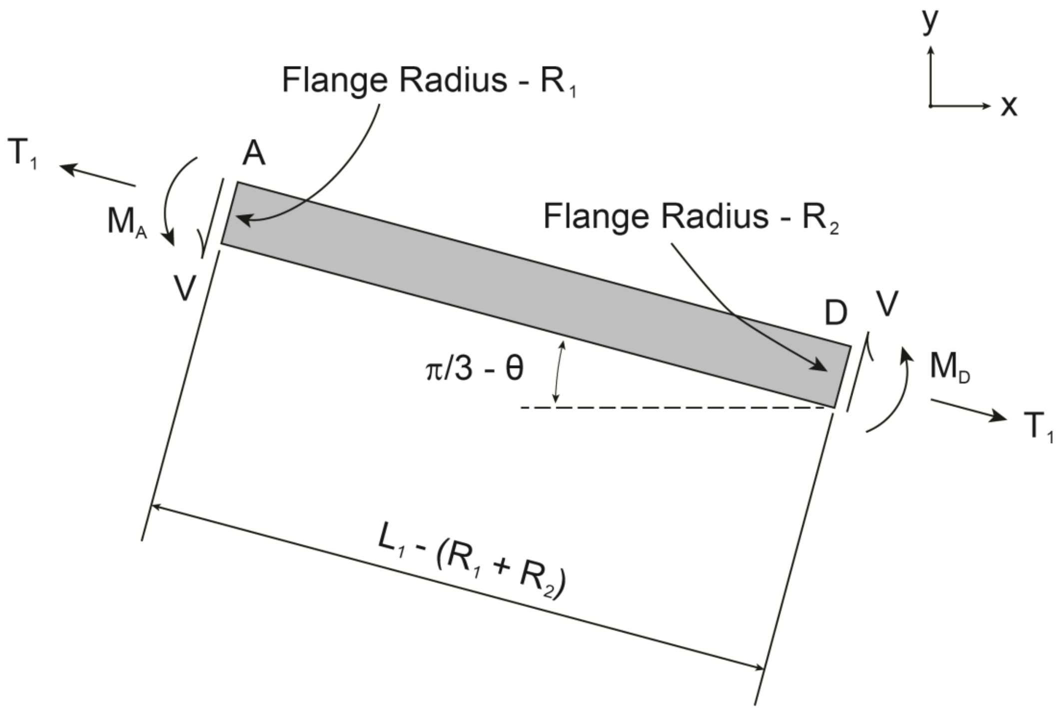

Figure 4 – Type 1 members sustain an axial load, T, shear, V, and bending moment, M.

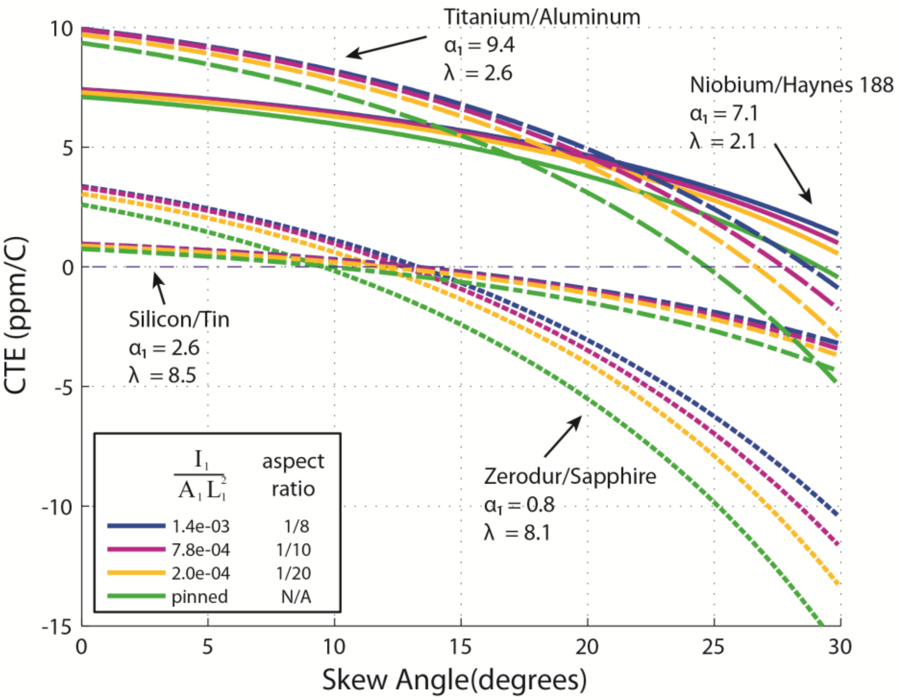

Figure 5- Lattice CTE as a function of skew angle θ and type 1 member aspect ratios.

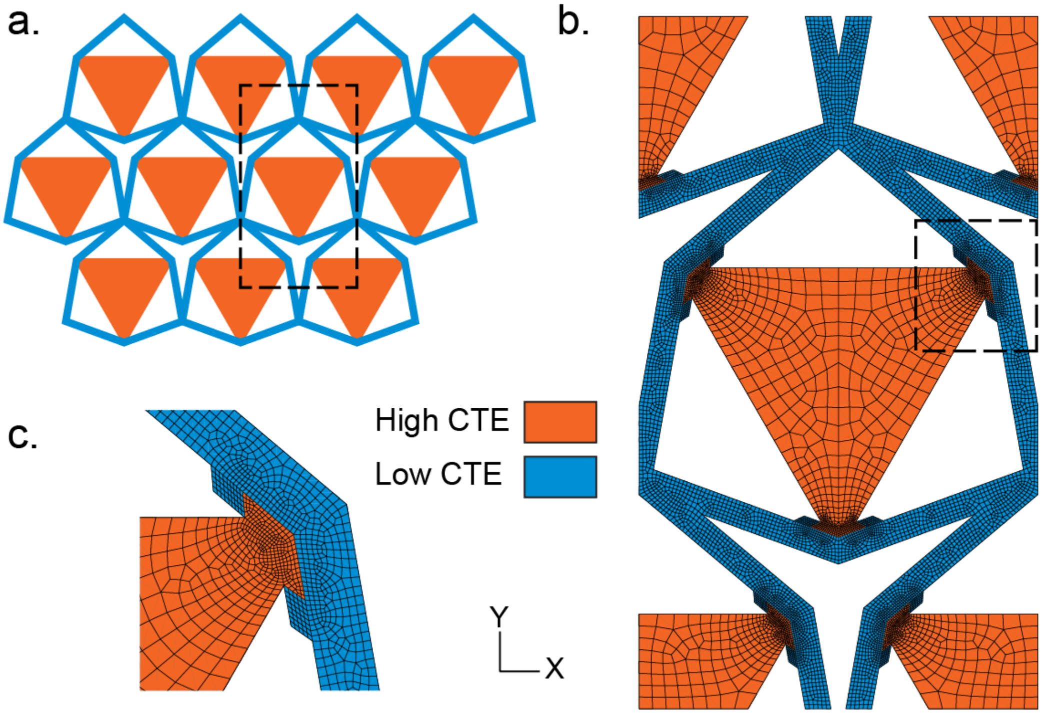

**Figure 6 – (a) Perimeter of unit cell used for computations. (b) Representative finite element mesh that consisted of 50,000 to 70,000 3-D elements. (c) Detail of a bimaterial joint region.**

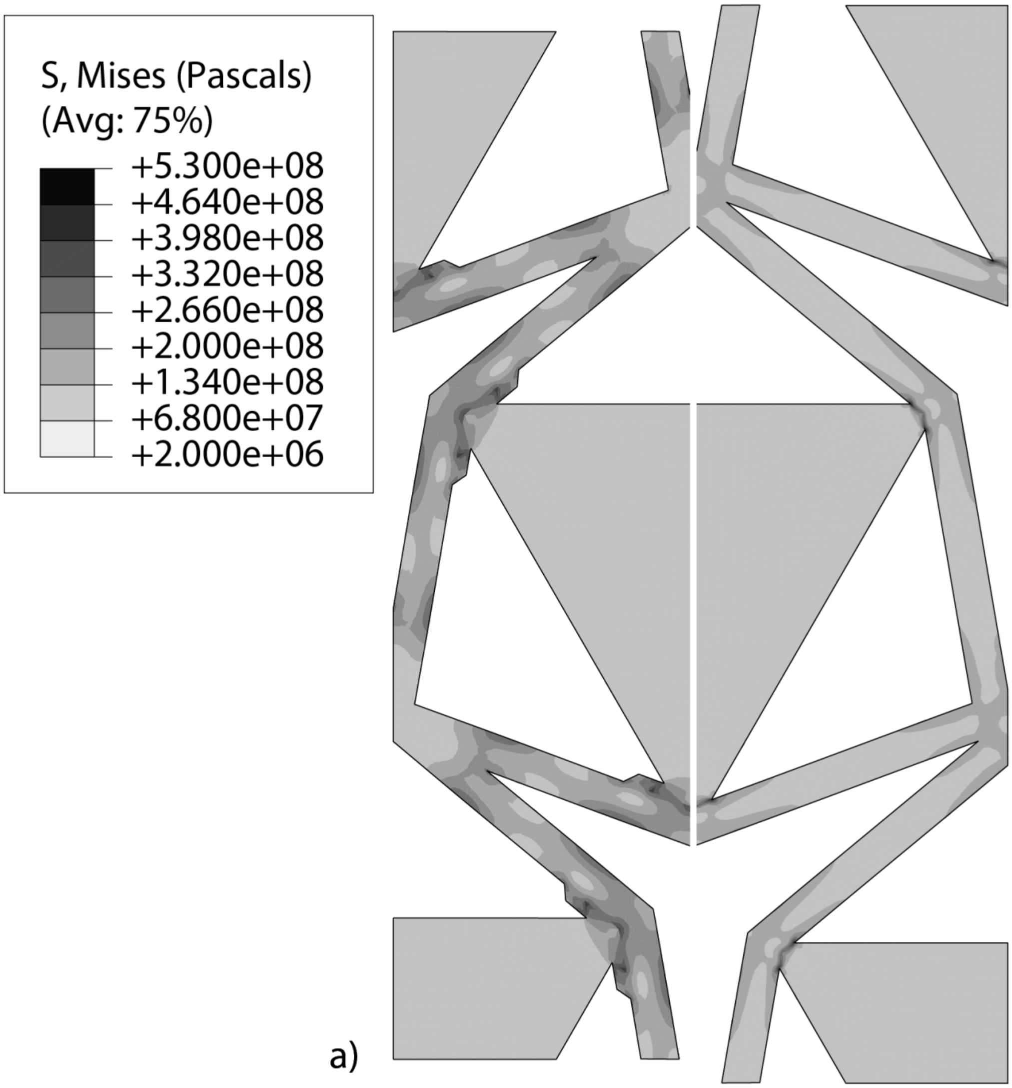

**Figure 7– Finite element thermomechanical stress distribution in Ti and Al lattices given the material properties listed in Table I and subject to a 175C temperature excursion – (a) original design, (b) new offset design.**

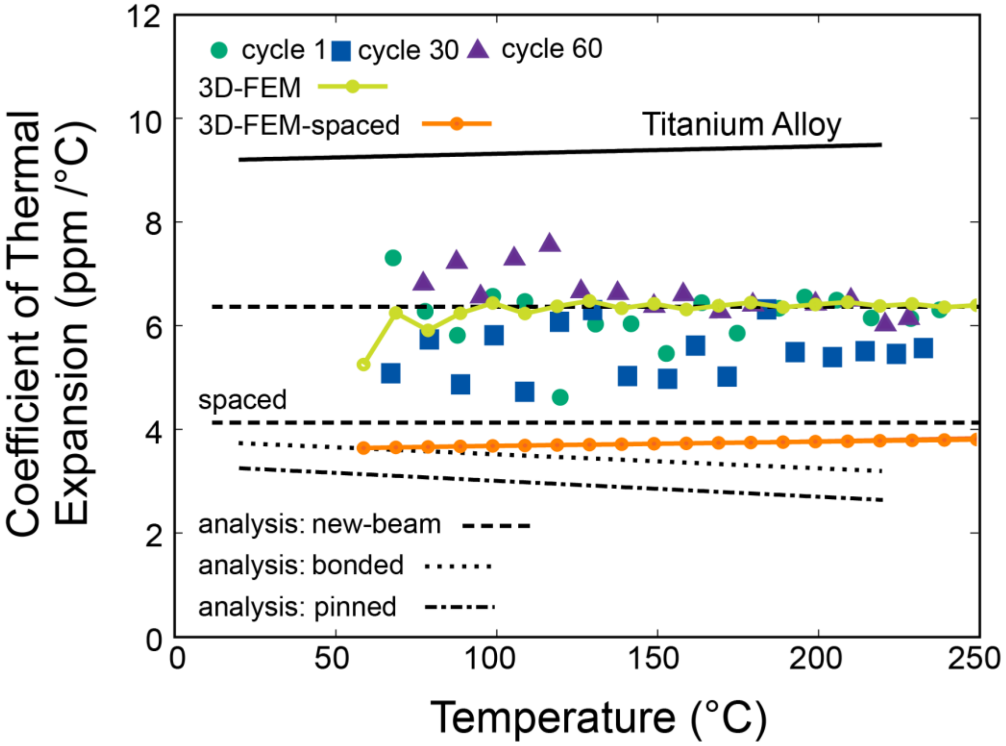

**Figure 8 - Comparison of results from finite element analysis for coefficient of thermal expansion and experiment.**

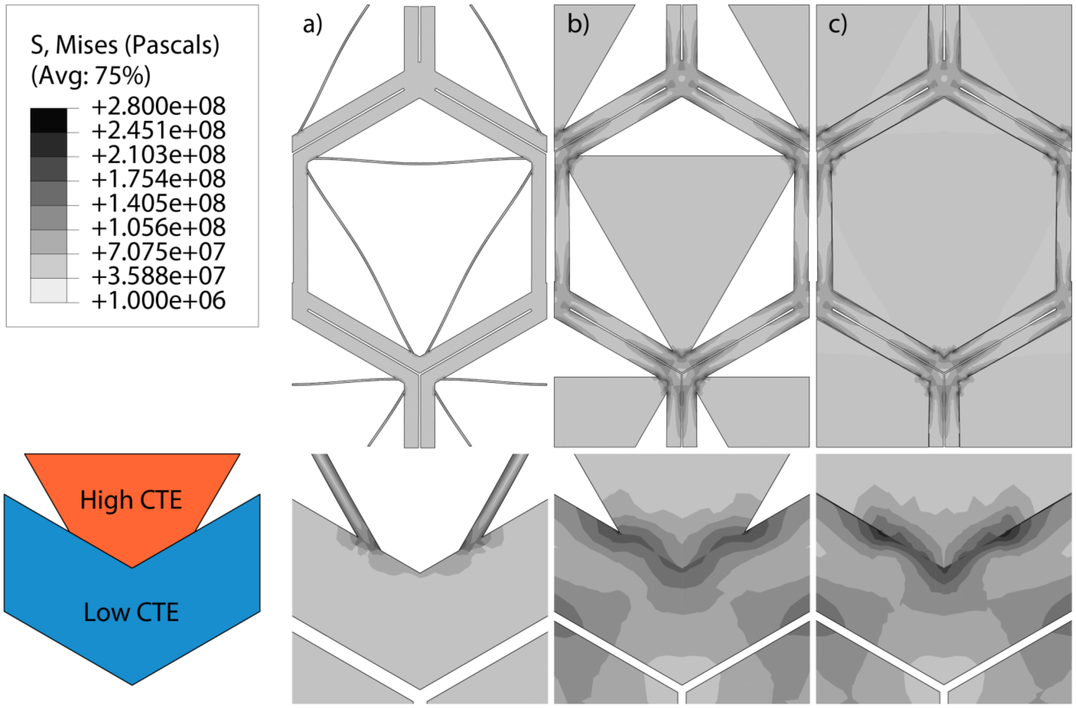

**Figure 9 – Thermal stress distributions in Ti and Al fabricated lattice geometry with thin type 1 members (a), triangular type 2 member (b), and space filling design (c).**

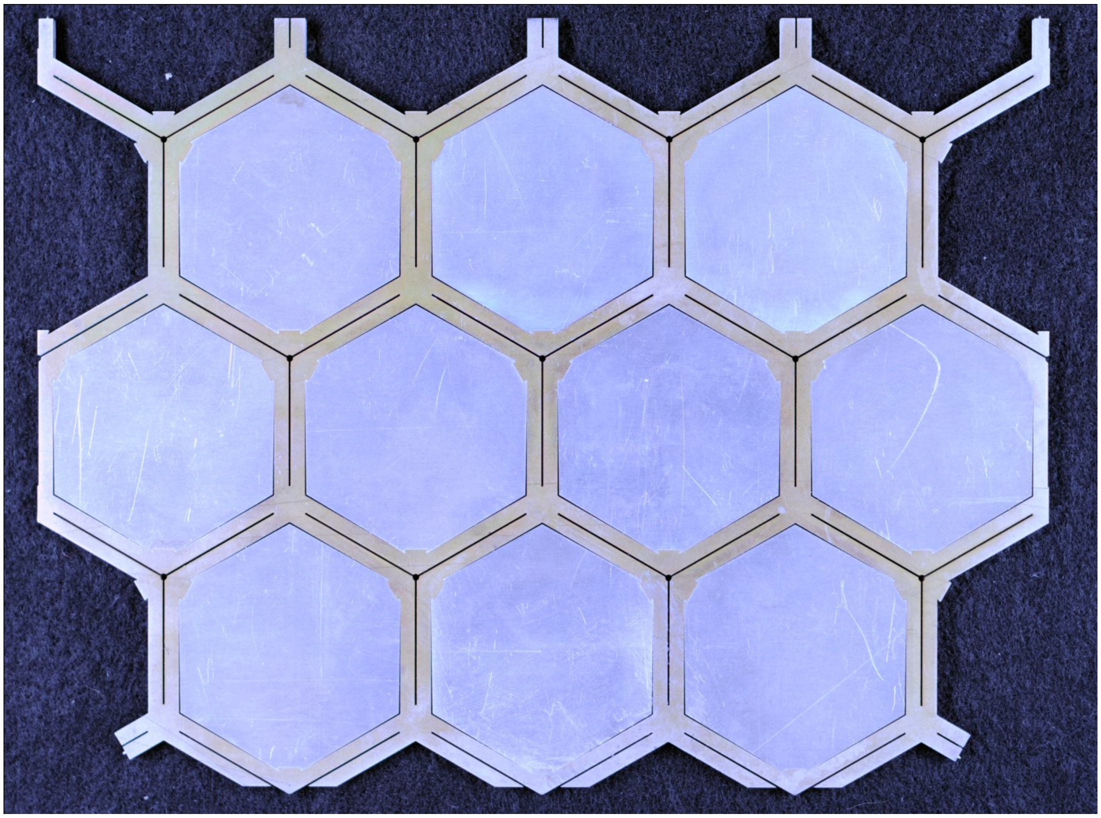

**Figure 10 – Lattices of Ti alloy (struts) and Al alloy (hexagonal units) fabricated for measurement of the coefficient of thermal expansion.**

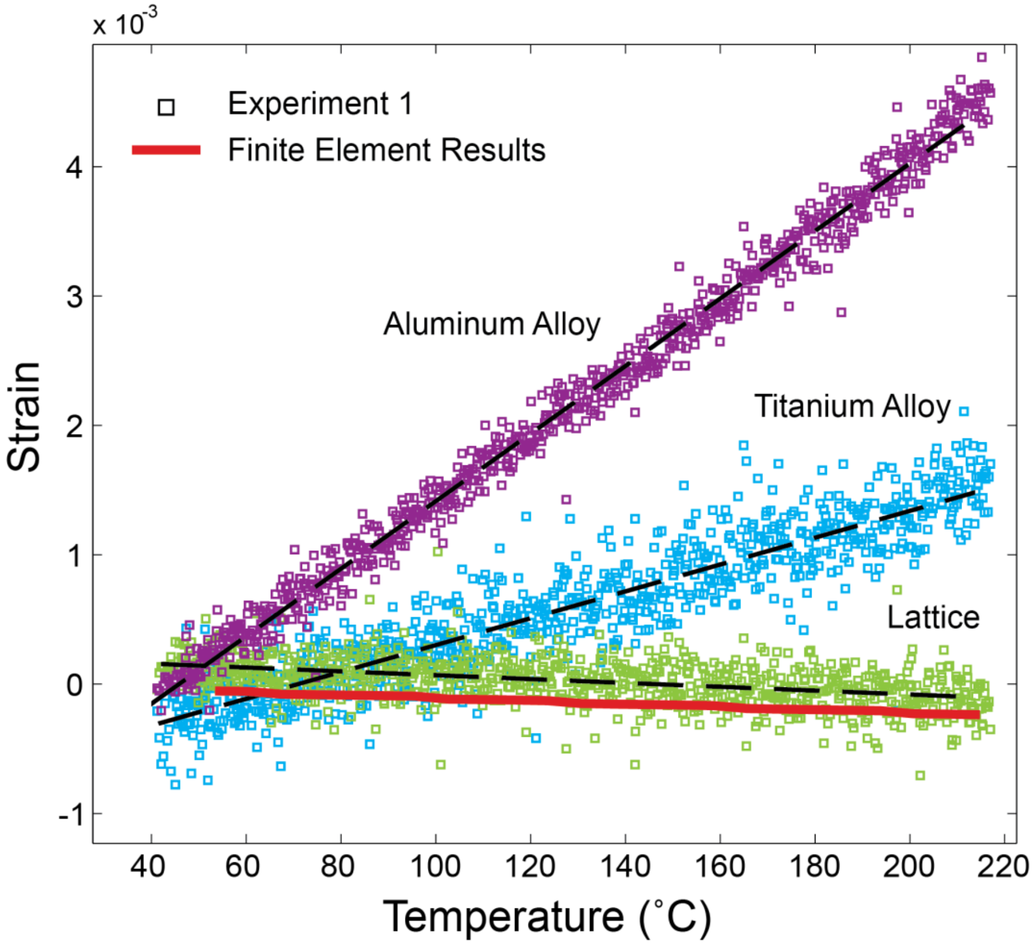

**Figure 11** - Thermal strains measured in Al alloy, Ti alloy, and the lattice. Significant scatter in Ti measurements is due to the relatively short gauge lengths that had to be used.

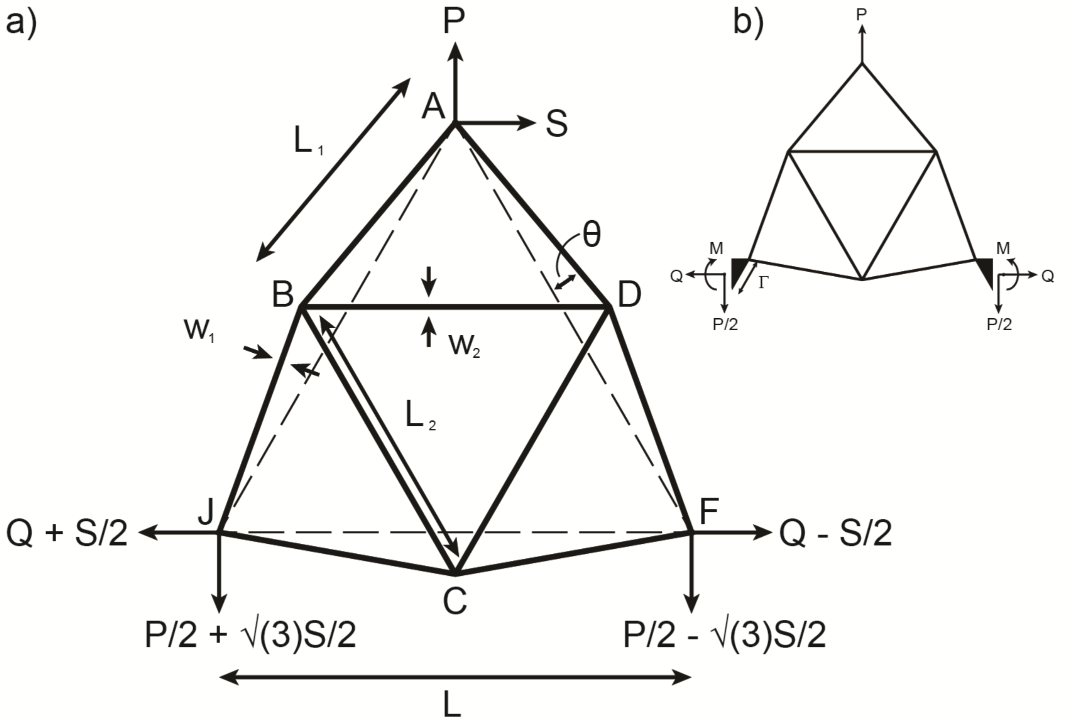

**Figure 12 – Pin-jointed unit cell subject to loads P,Q and S used in stiffness calculation (a). Spaced lattice unit cell with applied loads P and Q (b).**

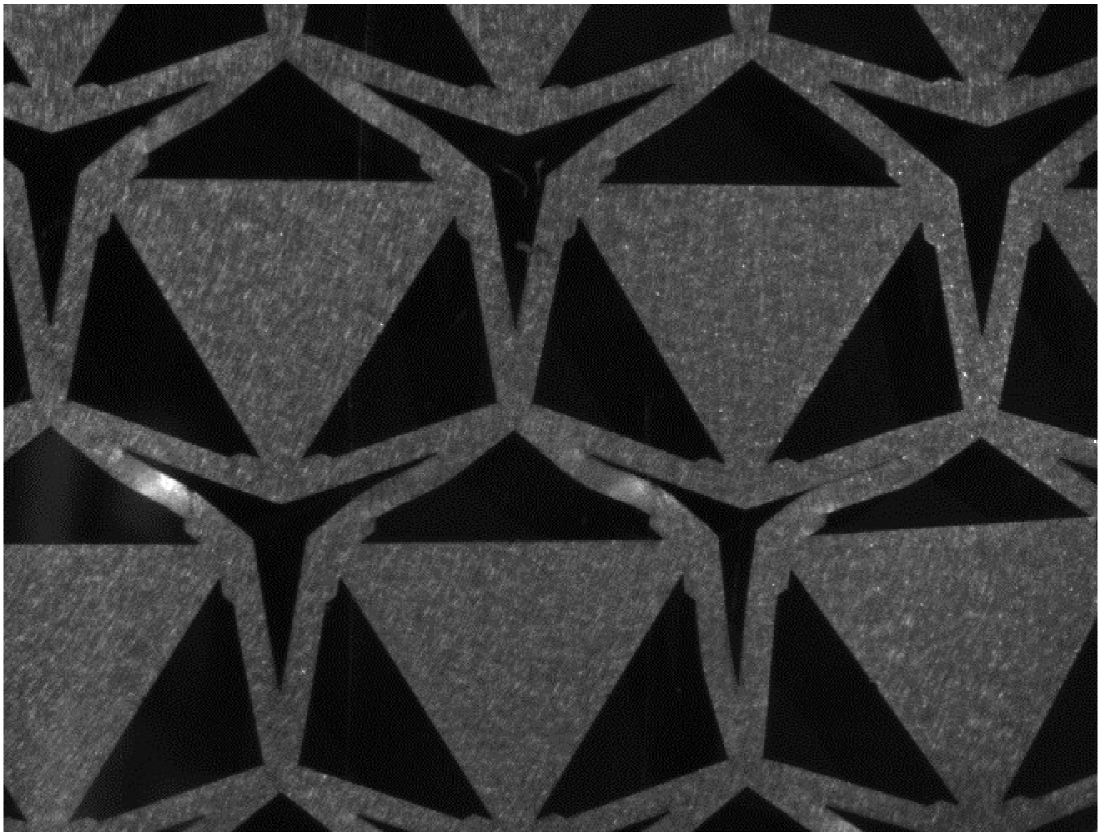

**Figure 13 – 304 stainless steel lattice compressed along the vertical axis. Bright areas indicate out of plane deformation associated with member buckling.**

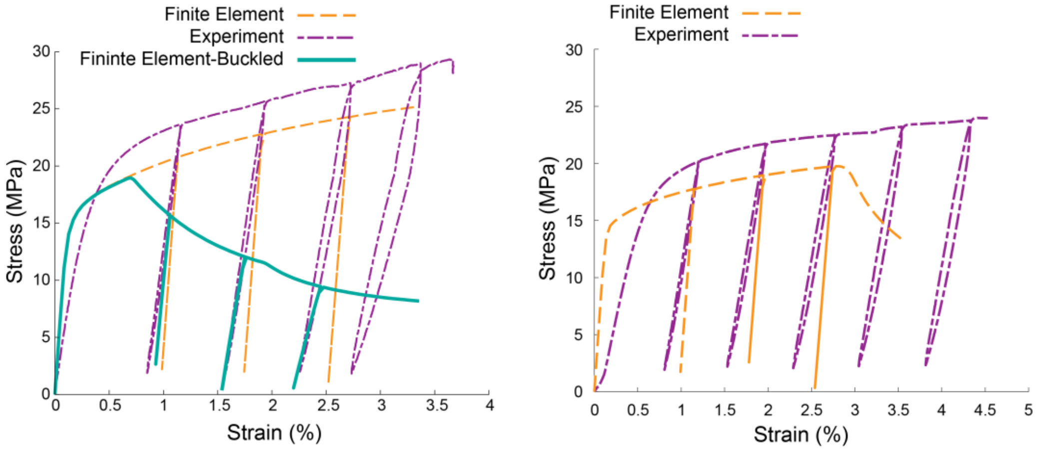

**Figure 14 – Uniaxial compression strain-stress behavior or 304 Steel lattices. (a) Triangular Type 2 element. (b) Thin Type 2 members.**

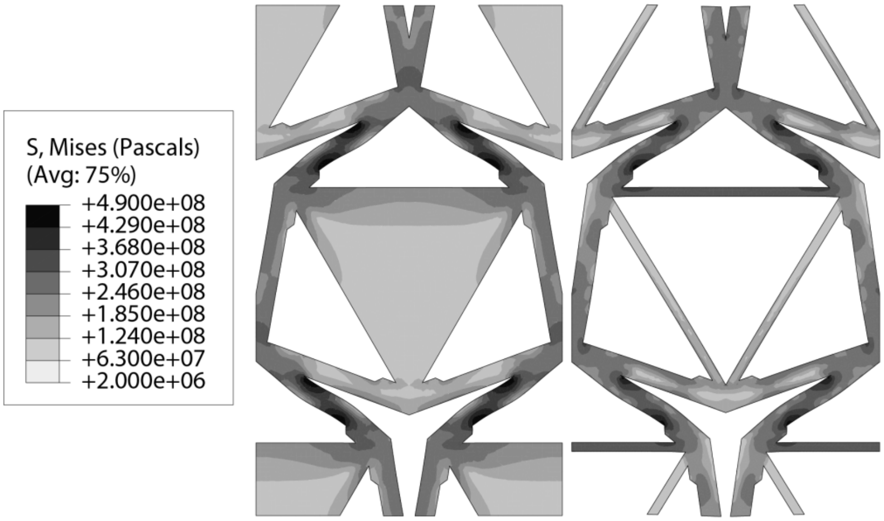

**Figure 15 – Finite element stress distributions in uniaxially compressed 303 stainless steel lattices. Yielding occurs in struts linking triangle vertices to 6-member joints a-d involves out of plane displacements. This behavior agrees well with experimental results.**

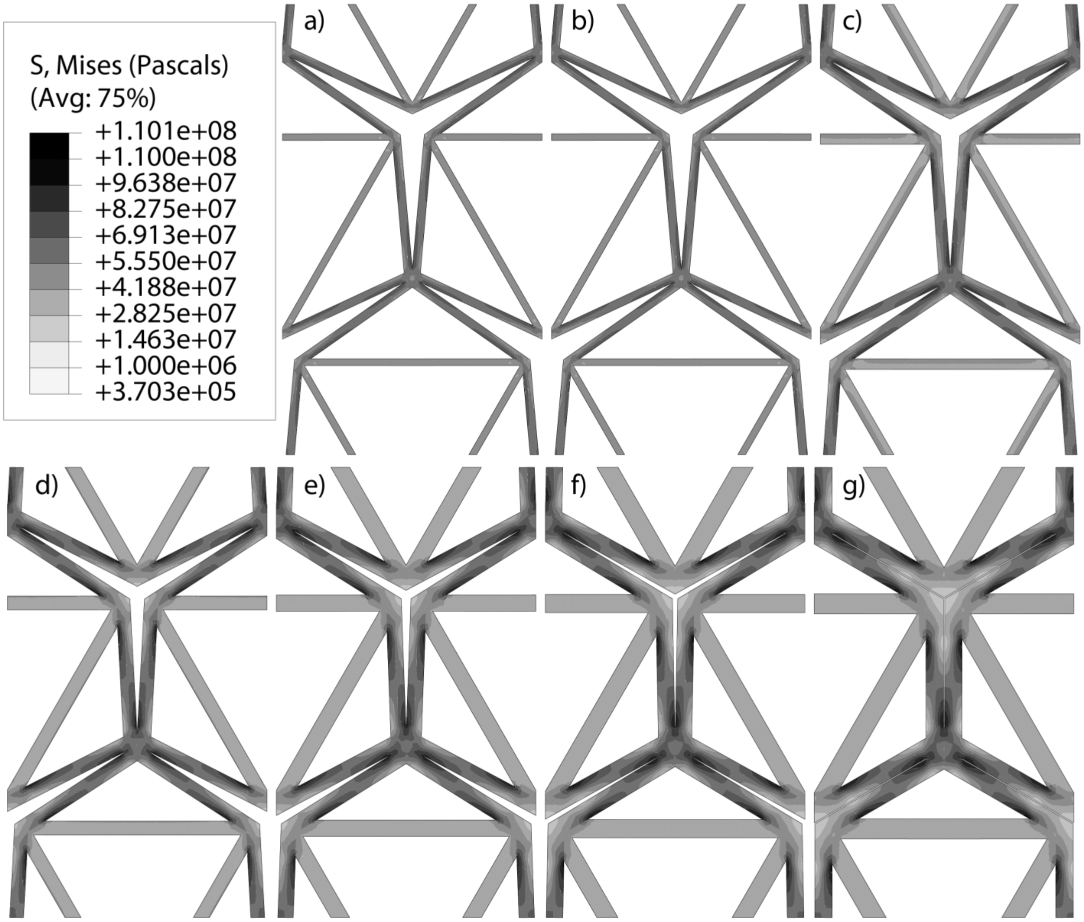

**Figure 16 –Stress distributions in lattices made from Ti alloy and Al alloy with maximum biaxial stiffness as predicted by pin-jointed analytical model, subject to 0.1% biaxial tensile strain. Skew angles range from 24.5°-30° and volume fractions of solid from 14-46% (a-g). Stress distributions become more uniform with increasing slenderness moving towards behavior similar to the pin-jointed response.**

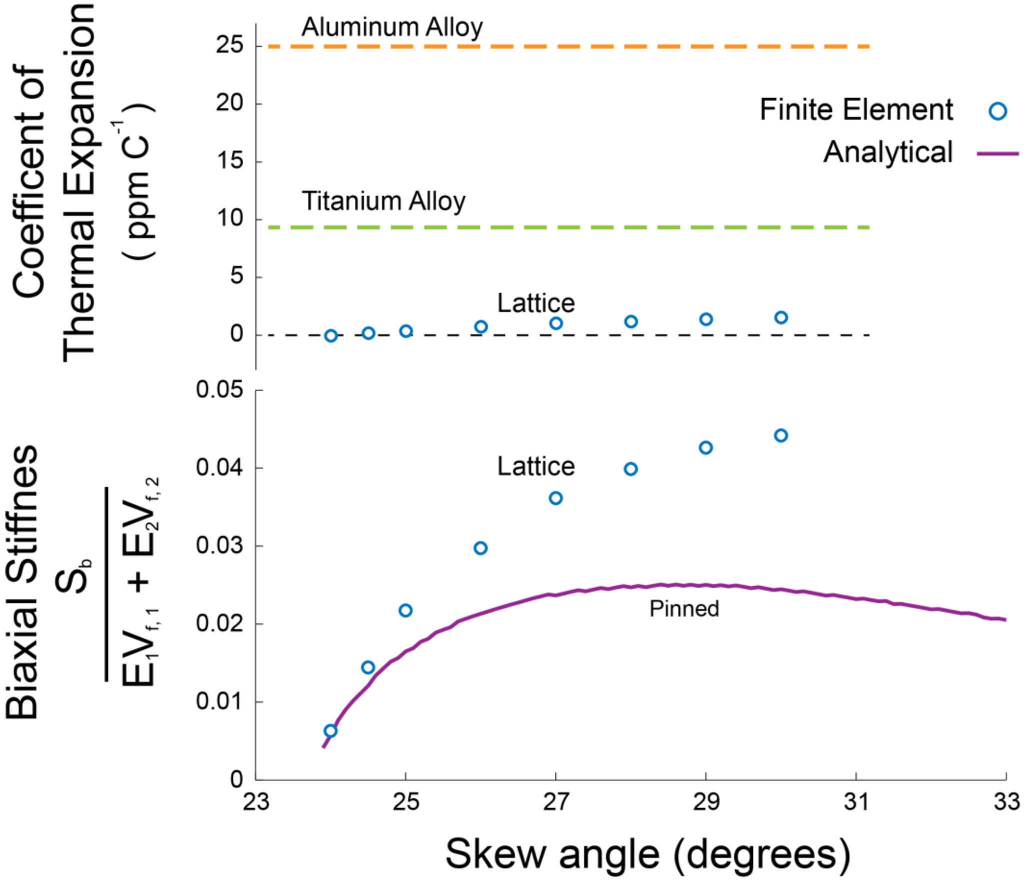

**Figure 17 – Results for the coefficient of thermal expansion and biaxial stiffness for lattices shown in Figure 16. Analytical results derived from a pin-jointed model are shown as are results from finite element analysis of lattices having bonded joints.**

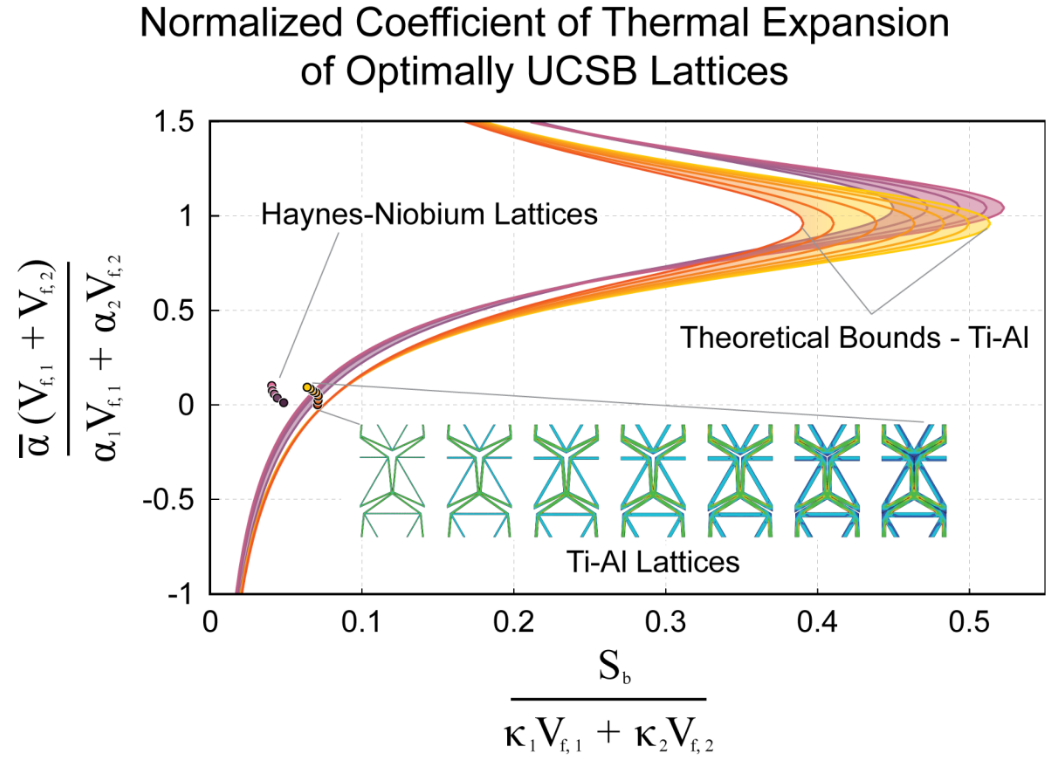

**Figure 18 – The biaxial stiffness, $S_b$, of seven lattice geometries composed of Ti6AlV4 and 7075-T6 Aluminum and five composed of Haynes and a niobium alloy along with their respective theoretical bounds on stiffness, devised by Gibiansky and Torquato (1997), which is a function of constituent properties and volume fractions. At effective CTEs near the rule of mixtures structures with a higher relative density (yellow) have a greater potential for stiffness over those with lower density (orange). At large deviations from the rule of mixtures (approaching zero CTE) the potential stiffnesses (theoretical bounds) converge. Lattices with slender members have more uniform stress and strain energy distributions and perform closest to the theoretical bound (darkest orange). Normalized biaxial stiffness is a measure of stretching indicating that lattices achieve only a small fraction of the stiffness of a bilayer of identical composition. When the low CTE constituent is more compliant than the high CTE, as in the case of two high temperature alloys, Haynes 188 and a niobium alloy, the stiffness of this material system relative to the theoretical bounds is reduced when the effective CTE is near zero(purple).**

# III. The Compressive Response of Some Idealized Foams

The compressive stiffness of a variety of 'perfect' foam topologies, most of which are based upon a spatial tessellation procedure, some described here for the first time, are calculated using three-dimensional (3D) continuum finite elements (FE) and representative volume element modeling. Using 3D models the relative density of the foams are calculated directly allowing for the results to be precisely placed in property space revealing a family of mostly stretch dominated structures, some of which achieve theoretically maximum stiffness. Novel topologies are based upon Voronoi-like tessellations producing closed-cell structures with plate-like members. A variety of foam topologies are found to have bulk moduli that are very near theoretical bounds over a range of volume fractions. One design in particular achieves, in essence, the theoretical bounds for Young's, shear and bulk modulus simultaneously, in the low density limit, exhibiting maximum isotropic stiffness. The body-centered cubic, face-centered cubic, simple cubic, octet-truss-lattice, octet-foam, quasi-random foams, and other geometries are evaluated using a strain homogenization technique to calculate their effective elastic properties. Results for known structures compare favorably with reported empirical results and analytical models, where available. Structures composed of plate-like members have a

**significantly higher potential for stiffness than open cell foams and lattices by supporting a multitude of loads through stretching where the others are composed of truss-like members which support only loads oriented along a single axis through stretching. Fabrication of geometries is achieved by additive manufacturing directly from CAD/FE models.**

## *Nomenclature:*

| | |
|---|---|
| $E_S$ | Young's modulus of solid constituent material |
| $G_S$ | Shear modulus of solid constituent material |
| $K_S$ | Bulk modulus of solid constituent material |
| $\rho_S$ | Density of solid constituent material |
| $\bar{E}_{ii}$ | Axial/Young's modulus of foam/lattice in the $i$'th direction |
| $\bar{G}_{ij}$ | Shear modulus of foam/lattice from an applied strain $\epsilon_{ij}$ |
| $\bar{K}_{ij}$ | Bulk modulus of foam/lattice calculated from $\epsilon_{ii}$ and $\nu_{ij}$ assuming isotropy |
| $\bar{\rho}$ | Density of foam/lattice |
| $\bar{\nu}_{ij}$ | Poisson ratio of foam/lattice |
| $\bar{E}$ | Average relative Young's modulus of foam/lattice |
| $\bar{G}$ | Average relative shear modulus of foam/lattice |
| $\bar{K}$ | Relative bulk modulus of foam/lattice |
| $V$ | Initial volume of RVE |

| | |
|---|---|
| $V_0$ | Deformed volume of RVE |
| $\overline{\boldsymbol{S}}$ | Macroscopic 1st Piola-Kirchoff Stress Tensor |
| $\overline{\boldsymbol{F}}$ | Macroscopic deformation gradient tensor |
| $\overline{\boldsymbol{T}}$ | Macroscopic Cauchy stress tensor |
| $\bar{\boldsymbol{\varepsilon}}$ | Macroscopic strain tensor |
| $l_{ij}$ | Wall thickness between cells $i$ and $j$ |
| $t$ | Wall thickness |
| $L_i$ | RVE dimension in direction $i$ |
| $g_i$ | Scale factor for seed $i$ |
| $\epsilon$ | Magnitude of the macroscopic strain |

## 1. Introduction

Lightweight high-performance materials such as metal foams and lattice materials are so called *hybrid materials*, material systems that combine different materials and/or materials and space in the aim of achieving novel properties, are capable of filling ‘holes’ in property space (Ashby, 2011) expanding the design capabilities of engineers with stiffer, stronger and lighter materials. While stretch dominated lattices, such as the octet-truss (Ashby, 2011; Deshpande et al., 2001), have been identified as prototypical hybrid materials offering properties such as stiffness and strength that surpass metal foams considerably, their performance does not achieve a large fraction of theoretical bounds. Topology optimization routines have been employed to identify structures with more optimal properties, (Radman et al., 2012; Sigmund, 2000) for example, in terms of individual parameters, yet it remains unclear if materials exist that achieve the theoretical bounds for Young's, shear and bulk modulus simultaneously (a material with theoretically maximum performance). While stochastic foams have already proven to outperform monolithic materials, in this study, we identify ordered foams as a class of hybrid materials capable of outperforming stretch dominated lattices and achieving theoretical bounds for Young's, shear and bulk modulus simultaneously having maximal properties, at least in the low density limit.

The relationship between ordered foams and closed cell stochastic foams is analogous to that of lattices and open cell foams. Lattices have improved structural properties over stochastic open cell foams, by a large margin, due to more ideal uniform geometry. The result is a relative homogenization of stress and strain energy distribution throughout the material from the uniformity of the structure. Ordered foams capitalize on the higher stiffness and strengths exhibited by closed cell foams over open cell stochastic foams, but have yet to be investigated to the same degree as lattices.

With advances in direct fabrication methods in the early 21st century it is now possible to create complex micron-scale structures out of aerospace grade alloys with relative ease and at low cost. Direct fabrication, or additive manufacturing, are terms used to describe the multitude of techniques that are antithetical to machining wherein material is placed selectively in space to construct a part rather than by the removal of material from a fully dense one. An attractive feature of additive manufacturing is that there is no cost associated with geometric complexity unlike machining and bonding methods. While these techniques currently have their limitations in terms of materials and geometries, posing problems when making some closed cell materials, these technical limitations will be overcome, with time, opening the possibility for new high-performance materials.

In this study we use three-dimensional (3D) computer automated design (CAD) to construct solid models of material geometries allowing a wide range of relative densities to be modeled accurately. Previous efforts to model foams and lattices have generally relied on analytical models (Deshpande et al., 2001; Gibson and Ashby, 2009; Grenestedt, 1999) and/or beam and shell finite elements (Daxner et al., 2006; Demiray et al., 2005; Deshpande et al., 2001; Fahlbusch and Becker, 2011; Fischer et al., 2009; Grenestedt and Bassinet, 2000; Grenestedt, 1999; Jang and Kyriakides, 2009a) to reduce the cost, both of labor and computational, of reaching solutions. The high computational cost alone of analyzing these types of problems with 3D models has historically made them cumbersome and unattractive. Shell models do well when applied to structures with low relative density but do poorly when applied to structures with densities that are intermediate and higher. If experimental verification of these models is desired, some interpretation must be done to construct a solid 3D design. Eventually a more accurate method is needed to guide in the development of high-performance materials. By using 3D FE the exact density of geometries is calculated allowing  a wide range of relative densities to be considered and the results placed accurately in property space. The CAD models used to generate the FE meshes can be imported into a program, such as ("Solidworks," 2012), to directly manufacture with an additive manufacturing machine.

Foams can have very low relative densities, $(\bar{\rho}/\rho_s) < 1\%$in many cases, making them excellent insulators, cushions, energy absorbers, acoustic dampers and light weight structural materials, with myriad other applications. Ordered lattice structures can outperform stochastic foams in terms of stiffness and strength (Ashby, 2011; Deshpande et al., 2001; Fleck et al., 2010; Valdevit et al., 2011; Wadley, 2006) and can serve as multifunctional systems allowing for fluid transport between cells. Ordered foams can outperform lattice structures for the same reasons stochastic closed cell foams outperform open cell foams. The random nature of stochastic foam microstructures can vary greatly depending on the forming process and constituent material resulting in vast range of properties. Factors such as surface energy, gravity and rise direction influence attributes like cell-wall thickness, local density and cell geometry. Inhomogeneities lead to localizations of stress that under load ultimately lead to failure (Jang and Kyriakides, 2009b). By designing and manufacturing foams with uniform cell walls and ideal geometries that more uniformly distribute stresses, postponing localization to higher loads, the strength and stiffness of foams can be increased dramatically. Understanding the features that lead to localization may make it possible to design geometries that have a hierarchy of ordered localization events that dictate the large strain behavior, offering improved energy absorption. Ordered foams have the potential to inherit many advantageous attributes of stochastic foams while offering increased performance in terms of stiffness and strength through more optimum material distribution.

There is an extensive historical body of work studying the properties of foams an lattices. **CELLULAR SOLIDS** (Gibson and Ashby, 2009) is an extensive study of stochastic foams compiling models and data relevant to all general foam applications. In their analysis of the stiffness of foams they used beam theory and dimensional analysis to model the compressive stiffness of cellular materials based upon the stretching of cell faces and bending of edges; this model will be used later in this work as a performance metric. Grenestedt (1999) used a similar analysis but computed an additional cubic term associated with the bending of plate like members that contributes to the stiffness. It will be shown later on in this paper that this cubic contribution is necessary to describe the stiffness of these foam topologies. Also compiled was a variety of analytical models for some 'perfect' foam geometries and FE analysis (FEA) to assess the stiffness of some idealized foams composed of polyhedra, including the BCC Kelvin foam (also included in this study). Deshpande et al. (2001) calculated the stiffness of a fully triangulated lattice known as the octet-truss (OT) using analytical and FE models. The OT is a triangulated structure that has often been used as the prototypical stretch dominated material, however it will be shown later on that ordered foams have stiffnesses far greater. A foam related to the OT, described by drawing planes between its edges, is also analyzed in this paper. Vigliotti et al. (2012) calculated the stiffness and plastic buckling strength of a variety of open and closed cell geometries using an in house FE code, describing some novel geometries, using plate and beam elements and expressing output in terms of the eigenvalues of the constituent material. While this body of work and more has been accomplished to characterize the stiffness and strength of lattices and foams, a direct comparison of a variety of high-performance structures to empirical results, especially at intermediate densities, has yet to be assembled. In this paper we will calculate the stiffness of a variety of both known and novel cellular geometries from low to intermediate density, placing the results precisely in property space in terms of stiffness and density.

Most foam models are based upon a spatial tessellation procedure. Voronoi tessellations can be used to form cellular structures that resemble stochastic materials. While they lack some features of real stochastic materials, such as curved cell faces, the effects of grain growth, gravity and processing, the approximation is often sufficient when modeling their behavior. The Voronoi tessellation of a space can be formed by growing spherical bubbles from a set of seed points that terminate their growth at every point that they meet. This procedure can be modified by altering the relative rate at which the spheres grow. A single set of seed points can then be tessellated into a continuum of geometries. When the seeding is ordered, space can be tessellated by a variety of polyhedra. Included in this design space are geometries like the octet-foam (OF) body centered cubic (BCC) and simple cubic (SC) foams studied by (Grenestedt, 1999) and many others. This modified Voronoi tessellation technique will be used to generate a variety of structures that is representative of this family of 'perfect' foams. Instead of using these geometries as simplified models for stochastic foams we will explore their properties as engineering materials.

The next section will discuss the methodology, including definition of some metrics as well as a description of the CAD and FE techniques employed. In section three the structures are illustrated and described. Section four contains the results for compressive stiffness. The final sections will discuss and then summarize the findings.

## *2. Methods*

### 2.1 Finite element method

A strain homogenization technique is used to calculate the effective mechanical properties of foam and lattice geometries using representative volume elements (RVE); this particular method is adopted from (Danielsson et al., 2002). Unit cells experience uniform macroscopic strains as if part of a continuum in an infinite body. Macroscopic strins and stresses are localized as a function of the material arrangement in the RVE which give rise to the homogenized effective properties. Boundary conditions impose homogeneous macroscopic strains, defined by the macroscopic strain tensor $\bar{\boldsymbol{\epsilon}}$, on a rectangular RVE with side lengths $L_1$, $L_2$ and $L_3$ (Figure 19-left). This technique can be applied to any model geometry, making no assumptions about symmetry, as long it is appropriately periodic as sets of periodic boundary nodes are required to impose the constraining equations.

An example mesh is pictured in Figure 19, right, showing the labeling convention for the sets of boundary nodes. Sets of boundary nodes are denoted $N_{x,y,z}$, where $x, y, z = 1,0,-1$ correspond to the base vectors. A value of 1 indicates that nodes in that set lie on a face with positive normal in the respective direction. For example, node set $N_{-1,0,1}$ has nodes with coordinates $(0, y, L_3)$, where $0 \leq y \leq L_2$, because its nodes lie on planes with normal vectors that point in the negative $\boldsymbol{x}$- and positive $z$-directions. In all there are 26 sets of boundary nodes corresponding to every permutation of $x$, $y$ and $z$, with the exception of all zeros, whose displacements are tied together in an intuitive fashion to form the periodic boundary conditions.

The displacements of nodes located on faces are linked through Equations (1) – (9),

$$u_1(N_{1,0,0}) = u_1(N_{-1,0,0}) + L_1\bar{\varepsilon}_{11}, \tag{1}$$

$$u_2(N_{1,0,0}) = u_2(N_{-1,0,0}) + L_1\bar{\varepsilon}_{12}, \tag{2}$$

$$u_3(N_{1,0,0}) = u_3(N_{-1,0,0}) + L_1\bar{\varepsilon}_{13}, \tag{3}$$

$$u_1(N_{0,1,0}) = u_1(N_{0,-1,0}) + L_2\bar{\varepsilon}_{12}, \tag{4}$$

$$u_2(N_{0,1,0}) = u_3(N_{0,-1,0}) + L_2\bar{\varepsilon}_{22}, \tag{5}$$

$$u_3(N_{0,1,0}) = u_3(N_{0,-1,0}) + L_2\bar{\varepsilon}_{23}, \tag{6}$$

$$u_1(N_{0,0,1}) = u_1(N_{0,0,-1}) + L_3\bar{\varepsilon}_{13}, \tag{7}$$

$$u_2(N_{0,0,1}) = u_2(N_{0,0,-1}) + L_3\bar{\varepsilon}_{23}, \tag{8}$$

$$u_3(N_{0,0,1}) = u_3(N_{0,0,-1}) + L_3\bar{\varepsilon}_{33}, \tag{9}$$

The nodes on edges and corners must be treated separately to avoid over constraining the model. There are only three unique edges, as all opposing edges on a face are separated by the wavelengths of the displacements in the directions of periodicity (the Bloch wave vectors) and therefore model the same material points. For similar reasons there is only one unique corner node. If the edge and corner nodes were included with their respective faces in the previous set of equations they would be over counted and over constrained.

The displacements of the edge nodes, $N_{0,-1,-1}$, $N_{-1,0,-1}$ and $N_{-1,-1,0}$, are all tied to their counterparts on the basal planes, lying on along the ***x***-, ***y***- and ***z***-axes respectively in Equations (10-37).

$$u_1(N_{0,1,1}) = u_1(N_{0,-1,-1}) + L_2\bar{\varepsilon}_{12} + L_3\bar{\varepsilon}_{13} \tag{10}$$

$$u_2(N_{0,1,1}) = u_2(N_{0,-1,-1}) + L_2\bar{\varepsilon}_{22} + L_3\bar{\varepsilon}_{23} \tag{11}$$

$$u_3(N_{0,1,1}) = u_3(N_{0,-1,-1}) + L_2\bar{\varepsilon}_{23} + L_3\bar{\varepsilon}_{33} \tag{12}$$

$$u_1(N_{0,1,-1}) = u_1(N_{0,-1,-1}) + L_2\bar{\varepsilon}_{12} \tag{13}$$

$$u_2(N_{0,1,-1}) = u_2(N_{0,-1,-1}) + L_2\bar{\varepsilon}_{22} \tag{14}$$

$$u_3(N_{0,1,-1}) = u_3(N_{0,-1,-1}) + L_2\bar{\varepsilon}_{23} \tag{15}$$

$$u_1(N_{0,-1,1}) = u_1(N_{0,-1,-1}) + L_3\bar{\varepsilon}_{13} \tag{16}$$

$$u_2(N_{0,-1,1}) = u_2(N_{0,-1,-1}) + L_3\bar{\varepsilon}_{23} \tag{17}$$

$$u_3(N_{0,-1,1}) = u_3(N_{0,-1,-1}) + L_3\bar{\varepsilon}_{33} \tag{18}$$

$$u_1(N_{1,0,1}) = u_1(N_{-1,0,-1}) + L_1\bar{\varepsilon}_{11} + L_3\bar{\varepsilon}_{13} \tag{19}$$

$$u_2(N_{1,0,1}) = u_2(N_{-1,0,-1}) + L_1\bar{\varepsilon}_{12} + L_3\bar{\varepsilon}_{23} \tag{20}$$

$$u_3(N_{1,0,1}) = u_3(N_{-1,0,-1}) + L_1\bar{\varepsilon}_{13} + L_3\bar{\varepsilon}_{33} \tag{21}$$

$$u_1(N_{-1,0,1}) = u_1(N_{-1,0,-1}) + L_3\bar{\varepsilon}_{13} \tag{22}$$

$$u_2(N_{-1,0,1}) = u_2(N_{-1,0,-1}) + L_3\bar{\varepsilon}_{23} \tag{23}$$

$$u_3(N_{-1,0,1}) = u_3(N_{-1,0,-1}) + L_3\bar{\varepsilon}_{33} \tag{24}$$

$$u_1(N_{1,0,-1}) = u_1(N_{-1,0,-1}) + L_1\bar{\varepsilon}_{11} \tag{25}$$

$$u_2(N_{1,0,-1}) = u_2(N_{-1,0,-1}) + L_1\bar{\varepsilon}_{12} \tag{26}$$

$$u_3(N_{1,0,-1}) = u_3(N_{-1,0,-1}) + L_1\bar{\varepsilon}_{13} \tag{27}$$

$$u_1(N_{1,1,0}) = u_1(N_{-1,-1,0}) + L_1\bar{\varepsilon}_{11} + L_2\bar{\varepsilon}_{12} \tag{28}$$

$$u_2(N_{1,1,0}) = u_2(N_{-1,-1,0}) + L_1\bar{\varepsilon}_{12} + L_2\bar{\varepsilon}_{22} \tag{29}$$

$$u_3(N_{1,1,0}) = u_3(N_{-1,-1,0}) + L_1\bar{\varepsilon}_{13} + L_2\bar{\varepsilon}_{23} \tag{30}$$

$$u_1(N_{-1,1,0}) = u_1(N_{-1,-1,0}) + L_2\bar{\varepsilon}_{12} \tag{31}$$

$$u_2(N_{-1,1,0}) = u_2(N_{-1,-1,0}) + L_2\bar{\varepsilon}_{22} \tag{32}$$

$$u_3(N_{-1,1,0}) = u_3(N_{-1,-1,0}) + L_2\bar{\varepsilon}_{23} \tag{33}$$

$$u_1(N_{1,-1,0}) = u_1(N_{-1,-1,0}) + L_1\bar{\varepsilon}_{11} \tag{34}$$

$$u_2(N_{1,-1,0}) = u_2(N_{-1,-1,0}) + L_1\bar{\varepsilon}_{12} \tag{35}$$

$$u_3(N_{1,-1,0}) = u_3(N_{-1,-1,0}) + L_1\bar{\varepsilon}_{13} \tag{36}$$

$$u_3(N_{1,-1,0}) = u_3(N_{-1,-1,0}) + L_1\bar{\varepsilon}_{13} \tag{37}$$

The displacements of the corner nodes are tied to the node at the origin, $N_{-1,-1,-1}$ in (38)-(58).

$$u_1(N_{1,1,1}) = u_1(N_{-1,-1,-1}) + L_1\bar{\varepsilon}_{11} + L_2\bar{\varepsilon}_{12} + L_3\bar{\varepsilon}_{13} \tag{38}$$

$$u_2(N_{1,1,1}) = u_2(N_{-1,-1,-1}) + L_1\bar{\varepsilon}_{12} + L_2\bar{\varepsilon}_{22} + L_3\bar{\varepsilon}_{23} \tag{39}$$

$$u_3(N_{1,1,1}) = u_3(N_{-1,-1,-1}) + L_1\bar{\varepsilon}_{1} + L_2\bar{\varepsilon}_{23} + L_3\bar{\varepsilon}_{33} \tag{40}$$

$$u_1(N_{-1,1,1}) = u_1(N_{-1,-1,-1}) + L_2\bar{\varepsilon}_{12} + L_3\bar{\varepsilon}_{13} \tag{41}$$

$$u_2(N_{-1,1,1}) = u_2(N_{-1,-1,-1}) + L_2\bar{\varepsilon}_{22} + L_3\bar{\varepsilon}_{23} \tag{42}$$

$$u_3(N_{-1,1,1}) = u_3(N_{-1,-1,-1}) + L_2\bar{\varepsilon}_{23} + L_3\bar{\varepsilon}_{33} \tag{43}$$

$$u_1(N_{-1,1,-1}) = u_1(N_{-1,-1,-1}) + L_2\bar{\varepsilon}_{12} \tag{44}$$

$$u_2(N_{-1,1,-1}) = u_2(N_{-1,-1,-1}) + L_2\bar{\varepsilon}_{22} \tag{45}$$

$$u_3(N_{-1,1,-1}) = u_3(N_{-1,-1,-1}) + L_2\bar{\varepsilon}_{23} \tag{46}$$

$$u_1(N_{1,1,-1}) = u_1(N_{-1,-1,-1}) + L_1\bar{\varepsilon}_{11} + L_2\bar{\varepsilon}_{12} \tag{47}$$

$$u_2(N_{1,1,-1}) = u_2(N_{-1,-1,-1}) + L_1\bar{\varepsilon}_{12} + L_2\bar{\varepsilon}_{22} \tag{48}$$

$$u_3(N_{1,1,-1}) = u_3(N_{-1,-1,-1}) + L_1\bar{\varepsilon}_{1} + L_2\bar{\varepsilon}_{23} \tag{49}$$

$$u_1(N_{1,-1,1}) = u_1(N_{-1,-1,-1}) + L_1\bar{\varepsilon}_{11} + L_3\bar{\varepsilon}_{13} \tag{50}$$

$$u_2(N_{1,-1,1}) = u_2(N_{-1,-1,-1}) + L_1\bar{\varepsilon}_{12} + L_3\bar{\varepsilon}_{23} \tag{51}$$

$$u_3(N_{1,-1,1}) = u_3(N_{-1,-1,-1}) + L_1\bar{\varepsilon}_{1} + L_3\bar{\varepsilon}_{33} \tag{52}$$

$$u_1(N_{-1,-1,1}) = u_1(N_{-1,-1,-1}) + L_3\bar{\varepsilon}_{13} \tag{53}$$

$$u_2(N_{-1,-1,1}) = u_2(N_{-1,-1,-1}) + L_3\bar{\varepsilon}_{23} \tag{54}$$

$$u_3(N_{-1,-1,1}) = u_3(N_{-1,-1,-1}) + L_3\bar{\varepsilon}_{33} \tag{55}$$

$$u_1(N_{1,-1,-1}) = u_1(N_{-1,-1,-1}) + L_1\bar{\varepsilon}_{11} \tag{56}$$

$$u_2(N_{1,-1,-1}) = u_2(N_{-1,-1,-1}) + L_1\bar{\varepsilon}_{12} \tag{57}$$

$$u_3(N_{1,-1,-1}) = u_3(N_{-1,-1,-1}) + L_1\bar{\varepsilon}_{13} \tag{58}$$

In the cases where models do not have corner or edge nodes the corresponding sets of equations are omitted.

To prevent ridged body rotations the symmetry of the macroscopic strain tensor,

$$\frac{1}{2}\left(\frac{\delta\bar{u}_i}{\delta x_j} - \frac{\delta\bar{u}_j}{\delta x_i}\right) = 0, \tag{59}$$

is ensured by omitting the lower triangular components, $\bar{\varepsilon}_{21}$, $\bar{\varepsilon}_{31}$ and $\bar{\varepsilon}_{32}$ in equations (1)-(58) where they have been replaced by , $\bar{\varepsilon}_{12}$, $\bar{\varepsilon}_{13}$ and $\bar{\varepsilon}_{23}$ respectively, effectively setting $\bar{\varepsilon}_{ij} = \bar{\varepsilon}_{ji}$. Ridged body translations are prevented by fixing the displacements, $u_1 = u_2 = u_3 = 0$, for one node in the model.

The effective stresses are extracted using the principle of virtual work,

$$\delta W^{ext} = \delta W^{int}. \tag{60}$$

The internal virtual work is calculated by noting that the macroscopic first Piola-Kirchhoff stress tensor, $\overline{\boldsymbol{S}}$, *is* work conjugate to the macroscopic deformation gradient tensor, $\overline{\boldsymbol{F}}$. The internal virtual work is,

$$\delta W^{int} = V_0 \overline{\boldsymbol{S}} \cdot \delta \overline{\boldsymbol{F}}, \tag{61}$$

where $V_0 = L_{1,0}\, L_{2,0}\, L_{3,0}$, is the initial volume of the RVE and $L_{i,0}$ are the initial dimensions of the RVE. The relationship between $\bar{\boldsymbol{\varepsilon}}$ and $\overline{\boldsymbol{F}}$ is

$$\overline{\boldsymbol{F}} = \bar{\boldsymbol{\varepsilon}} + \boldsymbol{I}, \tag{62}$$

with $\boldsymbol{I}$ being the 2nd order identity tensor and $\bar{\boldsymbol{\varepsilon}}$ is the macroscopic strain tensor.

The macroscopic first Piola-Kirchhoff stress is calculated from the local stress by,

$$\bar{\boldsymbol{S}} = \frac{1}{V_0}\int_{V_0} \boldsymbol{S} dV_0, \tag{63}$$

were $\boldsymbol{S}$ is the local first Piola-Kirchhoff stress tensor.

Components of $\bar{\boldsymbol{\varepsilon}}$ are accounted for computationally as the displacements of *virtual nodes;* nodes which are not otherwise attached to any part. The displacements of the virtual nodes and strains are related through

$$\bar{\varepsilon}_{ij} = \xi_j^i, \tag{64}$$

where $\xi_j^i$ is the displacement of virtual node $i$ in the $j^{\text{th}}$ direction.

The external virtual work is calculated from the displacements of the virtual nodes and their work conjugate reaction forces, $\Xi_{ij}$,

$$\delta W^{ext} = \sum_{i=1}^{3}\sum_{j=1}^{3} \Xi_{ij}\delta\xi_j^i. \tag{65}$$

By selectively prescribing components of $\bar{\boldsymbol{\varepsilon}}$ as displacement boundary conditions on the virtual nodes, all stress states compatible with uniform macroscopic strains can be modeled. The components of $\bar{\boldsymbol{S}}$ are found by combinging equations (60)-(65) to get,

$$\frac{1}{V_0}\Xi_{ij} = \bar{S}_{\boldsymbol{ij}}, \tag{66}$$

The macroscopic Cauchy stress and the macroscopic first Piola-Kirchhoff stress is related through,

$$\bar{\boldsymbol{T}} = \frac{V}{V_0}\bar{\boldsymbol{S}}\boldsymbol{F}^{-\mathbf{1}}, \tag{67}$$

where $V$ is the deformed volume of the unit-cell and $\bar{\boldsymbol{T}}$ is the macroscopic Cauchy stress. Because the strains at which the elastic properties are calculated are small, $\bar{\boldsymbol{S}} \approx \bar{\boldsymbol{T}}$**,** and the components of $\bar{\boldsymbol{S}}$ are used instead.

The implementation of this method in practice has been done in the context of the commercial finite element analysis (FEA) and computer automated design (CAD) package (“ABAQUS,” 2013). This software has the capacity to execute scripts that allow for the automation of the majority of commands involved in creation of models that are generally accessible through the graphical user interface, Abaqus CAE. Unit-cell geometries are generated using the built in CAD module, and in a few instances a dedicated commercial CAD package ("Solidworks," 2012). FE problems are described in text files that are typically generated by Abaqus CAE. It was necessary to pass information between the Abaqus script and a general purpose mathematics package, Matlab ("Matlab," 2013), using text files, to overcome limitations in Abaqus scripting capabilities. Ordered sets of boundary nodes are required for the use of the *equations* functionality in Abaqus needed in the implementation of Equations (1)-(58), however this requirement cannot be met with Abaqus scripting in the version that is current at the time this document was authored ("ABAQUS," 2013). Matlab was used additionally to generate the various input files associate with the different loading conditions used to calculate the mechanical properties, as well as for post processing of some results. Model generation was largely automated taking a few seconds to generate the simplest geometries and a few minutes for the most complex.

Stiffness calculations are found to be insensitive to the selection of unit cell for a given periodic geometry. It should be noted that in the case of calculating the strength and the large strain behavior of lattice and foam structures under compression, unit cell selection is of importance because of cell wall impingement associated with the onset of densification. In this study the effects of densification are not explored making unit cell selection somewhat arbitrary. As boundary node sets need to be sorted for the boundary conditions unit cells were usually selected to minimize the number of boundary nodes in order to reduce the computational time taken to generate input files. The mesh generating algorithms in Abaqus do not number nodes in a manner amenable with the institution of the boundary conditions (BC) so an extra step must be taken to spatially sort the node sets. The algorithm employed to sort the node sets checks the distance between nodes so that the time required scales with the square of the number of nodes.

Models are relatively large in size ranging from ~5.0x$10^3$ to ~6.5x$10^5$ elements, and ~4.0 x$10^4$ to ~1.2 x$10^6$ nodes. Most models are composed of 10-noded quadratic tetrahedral elements, type C3D10 in Abaqus, while the remainder used 20-noded quadratic brick elements (C3D20R). Non-linear geometry is considered through the activation of the *nlgeom* flag in Abaqus allowing for bifurcation and other nonlinear events to be a captured. The memory requirements were ~50 Gb for large simulations, and ~70 Gb in the most extreme case. A simulation was typically run on 4 ~3 GHz cpus and took on the order of hours to run. A large computing cluster was used to handle the majority of the work.

## 2.1 Stiffness and Isotropy

To characterize and quantify the stiffness of these materials the effective elastic properties $\bar{E}, \bar{G}$, $\bar{K}$ and $\bar{\nu}$ are calculated. These are calculated from the macroscopic stresses and strains by

$$\bar{E}_{ii} = \frac{\bar{S}_{ii}}{\bar{\varepsilon}_{ii}}, \qquad \text{under applied strain} \qquad \bar{\varepsilon}_{ii} = \epsilon, \tag{68}$$

$$\bar{G}_{ij} = \frac{\bar{S}_{ij} + \bar{S}_{ji}}{4\bar{\varepsilon}_{ij}} = \frac{\bar{S}_{ij} + \bar{S}_{ji}}{2\gamma_{ij}}, \qquad \text{under applied strain} \qquad \bar{\varepsilon}_{ij} = \frac{\bar{\gamma}_{ij}}{2} = \epsilon, \tag{69}$$

$$\bar{K} = \frac{\bar{S}_{ii}}{3\bar{\varepsilon}_{ii}}, \qquad \text{under applied strains} \quad \bar{\varepsilon}_{11} = \bar{\varepsilon}_{22} = \bar{\varepsilon}_{33} = \epsilon, \tag{70}$$

$$\bar{\nu}_{ij} = -\frac{\bar{\varepsilon}_{jj}}{\bar{\varepsilon}_{ii}}, \qquad \text{under applied strain} \qquad \bar{\varepsilon}_{ii} = \epsilon, \tag{71}$$

where $\epsilon$ is the magnitude of the applied strain; all with no summation. The need to average the stresses in equation (69) arises from the manner in which FE method computes the solution. For the case of pure shear the boundary conditions are $\xi_j^i = \xi_i^j = \epsilon$ however the means by which the displacements are tied results in only one virtual node experiencing a reaction force. In reality equilibrium requires $\bar{S}_{ij} = \bar{S}_{ji}$. For materials with cubic symmetry there are only three independent elastic constants *E*, *G* and $\nu$. Almost all the structures studied in this paper possess cubic symmetry and further, are nearly isotropic.

The bulk modulus can also be calculated from the axial modulus and Poisson ratio, assuming isotropy, as

$$\bar{K}_{ij} = \frac{\bar{E}_{ii}}{3(1 - 2\bar{\nu}_{ij})}, \tag{72}$$

with no summation. This is done as a check on the direct bulk calculations.

To quantify the isotropy of these materials a metric based upon the effective elastic properties is developed. While isotropy has a clear definition in the case of materials with cubic symmetry, not every material in this study has this property. Materials with cubic symmetry have three independent components of the stiffness matrix, $C_{1111}, C_{1122}$ and $C_{1212}$, when the axes of symmetry are parallel to the base vectors. Such a material is isotropic if the ratio of $(C_{1111} - C_{1122})/2C_{1212} = 1$. To devise a metric for isotropy that does not rely on any symmetry an equation that relies upon a ratio of the normalized average effective moduli is used,

$$a = 1 - \left|1 - \left(\bar{E}_{avg}/E_S\right)/\left(\bar{G}_{avg}/G_S\right)\right|, \tag{73}$$

where $a = 1$ for an isotropic material and $a \leq 1$. Although the Poisson ratio is not a factor in Equation (73) for materials with cubic material symmetry, the ratio $\left(\bar{E}_{avg}/E_S\right)/\left(\bar{G}_{avg}/G_S\right)$ is qualitatively the same as $(C_{1111} - C_{1122})/2C_{1212}$ and are nearly equivalent when $a \gtrsim 0.7$. Equation (73) gives slight preference to, that is, $a$ is greater for, materials that are stiffer in shear than axially for a given ratio of $\left(\bar{E}_{avg}/E_S\right):\left(\bar{G}_{avg}/G_S\right)$.

## 2.2 Theoretical bounds and modeling

To help quantify the stiffness two sets of theoretical bounds are employed. The tightest bounds on stiffness of isotropic multiphase materials were derived by (Hashin and Shtrikman, 1963). The bounds on bulk and shear moduli are respectively,

$$\frac{K_{HSU}}{K_s} = \frac{4G_s(\overline{\rho}/\rho_s)}{4G_s + 3K_s(1 - \overline{\rho}/\rho_s)}, \tag{74}$$

$$\frac{G_{HSU}}{G_s} = \frac{(9K_s + 8G_s)(\overline{\rho}/\rho_s)}{20G_s + 15K_s - 6(K_s + 2G_s)(\overline{\rho}/\rho_s)}, \tag{75}$$

where the subscripts *s* denotes properties of the solid and $\bar{\rho}$ is the density of the lattice/foam material. An upper bound on Young's modulus can be found from (74) and (75) by assuming isotropic linear elasticity. In a more general case where one phase is empty space the bounds reduce to,

$$\frac{\overline{K}}{K_s} = \frac{\overline{\rho}}{\rho_s}, \tag{76}$$

$$\frac{\overline{G}}{G_s} = \frac{\overline{\rho}}{\rho_s}, \tag{77}$$

which are identical to the Voigt bounds.

Using beam theory and dimensional analysis (Gibson and Ashby, 2009), and similarly by (Grenestedt, 1999), postulated that the stiffness of closed cell foams is dependent upon the local modes of deformation in the mesostructure; more specifically the bending of cell edges and stretching of cell faces. In the Gibson and Ashby model (G-A) material is partitioned between edges and faces so that material is either bent or stretched but not both. The formulas derived for Young's and shear moduli are,

$$\frac{\bar{E}}{E_s} = \left(\frac{\bar{\rho}}{\rho_s}\right)^2 \phi^2 + \frac{\bar{\rho}}{\rho_s}(1-\phi), \tag{78}$$

$$\frac{\bar{G}}{G_s} = \left(\frac{\bar{\rho}}{\rho_s}\right)^2 \phi^2 + \frac{\bar{\rho}}{\rho_s}(1-\phi), \tag{79}$$

where $(1-\phi)$ is the fraction of the material located in cell faces and $\phi$ is the remaining fraction residing in the edges. The contribution to the stiffness from the bending of edges is of second order illustrating the importance of stretching behavior in high performance structures.

Grenestedt's analysis, also using beam theory and dimensional analysis, derived the following relationship between Young's modulus and density for a foam,

$$\frac{\bar{E}}{E_s} \propto \left(\frac{\bar{\rho}}{\rho_s}\right)^m, \tag{80}$$

where $m$=1 for stretching controlled mesostructures, $m$=2 for bending or twisting controlled rod-like mesostructures and $m$=3 for bending controlled plate-like mesostructures (Grenestedt, 1999). The word *mesostructures* has been used in place of the original *microstructures*. In this study we refer to microstructural features on the scale that includes grain boundaries, inclusions and twins, foam topologies are defined on the mesoscale while loads and part geometries on macroscale.

In an effort to gauge the performance of foam topologies in a manner compatible with the work of (Ashby, 2011) and (Grenestedt, 1999) data is fit to third order polynomial functions with positive coefficients,

$$\frac{\bar{E}(\bar{\rho})}{E_s}, \frac{\bar{G}(\bar{\rho})}{G_s} = C_1\left(\frac{\bar{\rho}}{\rho_s}\right) + C_2\left(\frac{\bar{\rho}}{\rho_s}\right)^2 + C_3\left(\frac{\bar{\rho}}{\rho_s}\right)^3, \tag{81}$$

with the constraints $\bar{E}(0) = 0$ and $\bar{E}(\rho_s) = E_s$, similarly for $\bar{G}$. Here $C_1 + C_2 + C_3 = 1$ and can perhaps be thought of in a way consistent with both the analysis of (Gibson and Ashby, 2009) and (Grenestedt, 1999) thinking of the coefficients in Equation (81) like those in Equations (78) and (79), partitioning the material by orientation and mode of deformation, the $C_i$ being the relative fractions.

## 2.2 Tessellation procedure

Foam geometries are created using a modified Voronoi tessellation procedure, with two exceptions, the octet-truss and the dodecahedral-pyramidal foam (DDPF) which were generated using the CAD package ("Solidworks," 2012). Seed points are distributed in a finite 3-D space and lines are drawn between neighbors. These lines are then bisected by perpendicular planes. Each seed is then enclosed by a cell whose edges are defined by the nearest intersections of those planes. By varying the number and position of seed points and the position of the planes along the connecting lines a diverse range of geometries can be generated that in turn exhibit a wide range of behavior.

A number of point seeds, *n*, are placed into a rectangular space that will become the representative volume element (RVE) with coordinates are $x_i^j, i = 1,2,3; j = 1,2, \dots, n.$ Periodic structures are generated by copying the point seeds 26 times into, what would be, every adjacent RVE sharing an edge and/or face and/or corner with the primary RVE. This process is done by creating 27 instances of each seed point by adding every permutation of a vector $\boldsymbol{v} = (v_1\hat{\boldsymbol{x}}_{\boldsymbol{1}}, v_2\hat{\boldsymbol{x}}_{\boldsymbol{2}}, v_3\hat{\boldsymbol{x}}_{\boldsymbol{3}})$ ,where $v_i = -1, 1, 0$, to the seed coordinates $\boldsymbol{x}^k$ where *k* is seed point index, $k = 1,2, \dots, n$. If this seeding is done in a random fashion the result resembles real stochastic materials, to first order. If the seeding is done in an ordered fashion the result is analogous to the first brillouin zone of the crystal structure. Foams based upon the body centered cubic (BCC), face centered cubic (FCC) and diamond crystal structures are studied in later sections.

Topologies are made by a subtraction process in the CAD environment where an initial volume of material is systematically eroded. Foams are created by first constructing the reciprocal polyhedrons that define each cell. To construct the cell associated with seed $i$, the vector,

$$\boldsymbol{d}^{i,j} = \boldsymbol{x}^{j} - \boldsymbol{x}^{i}, \tag{82}$$

that extends between seed points $i$ and $j$ is found. To model the growth of different seeds at different rates each seed is assigned a growth factor, $g_i$, $i$=1,2,…,$n$, which is used to calculate the relative placement of the partitioning plane between seed pairs. The vector $\boldsymbol{d}^{i,j}$ is scaled by an amount determined by the growth factors, $g_i$ and $g_j$, and then reduced in length again by half of the wall thickness.

$$\boldsymbol{p}^{i,j} = \left(\frac{g_i}{g_i + g_j} - \frac{\ell_{i,j}}{2\left|\boldsymbol{d}^{i,j}\right|}\right)\boldsymbol{d}^{i,j}. \tag{83}$$

The resultant vector $\boldsymbol{p}^{i,j}$ and the perpendicular plane it describes define two half-spaces. The half space not containing seed point $\boldsymbol{x}^{i}$ is removed creating a facet and the process is repeated for every seed point in the set $B_i$, that contains all the neighboring seed points to $\boldsymbol{x}^{i}$. After repeating this for all the seeds in the primary RVE and adjacent RVEs the resulting cells are assembled and then subtracted from the fully dense RVE resulting in a closed cell material.

The number of seed points in the set of neighbors, $B_{i,}$, must be chosen carefully in the case where the growth factors $g_i \neq g_j$ for $i, j \in 1,2, \dots, n$. Seeds that are not nearest neighbors by distance can interact in this scenario creating additional facets on the reciprocal polyhedron of a cell which increases the relative density of the resulting foam. Seed points in $B_i$ are grouped by their distance, $\left\|\boldsymbol{d}^{i,j}\right\|$, which corresponds to a type of facet, and the number of facet types for cell $k$ is the coordination number, $b_k$.

The wall thickness, $\ell_{i,j}$, associated with the partition between seeds $i$ and $j$ are set to a constant value, $\ell_{i,j} = t$, for all the seed points in each model.

Randomly seeded geometries will serve as a benchmark for ordered foam performance and will be introduced in section 3.1. A "hard sphere" point seed algorithm is used to populate the RVE with seed points. A radius, $r$, is ascribed to each seed to enforce a minimum distance between seed points of $2r$. The radius is calculated from the fractional volume of the seed point in the RVE (Equation 84) which is then scaled by an amount, $\beta$, which is the packing density. The radius, $r$, is then,

$$r = \beta \left( \frac{3}{4\pi} \frac{V_0}{n} \right)^{\frac{1}{3}}. \tag{84}$$

Seeds are placed sequentially into the RVE by a pseudo-random number generator. A seed attempt is retried if upon the addition of a seed, two spheres are found to impinge upon each other. After a prescribed number of attempts the algorithm restarts the entire seeding process; this value was set to be on the order of

10 based upon experience. The initial seed is always placed at the origin to avoid the creation of noncontiguous RVE geometries.

## *3. Structures*

### 3.1 Quasi-random foams

Random distributions of seeds, in cubic unit cells of unit dimension, are used to generate structures that appear similar to stochastic foams (Figure 19). Quasi-random (QR) foam RVEs resemble unit cells of stochastic materials however are characteristically different in that they possess uniform cell wall thicknesses, lack curvature and have inherent periodicity. The performance of these structures will serve as a benchmark for comparison with foams with significantly more order and to lattice structures.

Two examples of quasi-random topologies are pictured in Figure 19 along with their associated meshes. The structures have wall thickness of 1% and 2% (left and right respectively), that is, they have $t/l = 1\%$ and 2%. The mesh density, as seen in Figure 19, bottom, is dictated by the wall thickness, as the characteristic element dimension is the wall thickness in thin walled models. Typically the characteristic element dimension is ~0.01-0.02 in models with $t/l > 2\%$ although no more than eight elements were used through the thickness of a cell wall. The computational cost of analyzing models with thinner walls of lower relative density but higher mesh density was seen as too great for this investigation. The models in Figure 19 have 2% wall thickness with 143,542 elements, 263,581 nodes and 790,740 total variable (degrees of freedom plus Lagrange multipliers)  and 1% wall thickness with 650,007 elements, 1,206,305 nodes and 3,618,912 total variables.

To achieve a narrow distribution of cell volumes and aspect ratios QR foams are based upon dense packings of spheres. The packing densities ranged from $0.5 < \beta < 0.61$ (Table 1) which is in the range of jammed packings of spheres, ~0.49-0.64 (Torquato and Stillinger, 2010). A jammed packing of spheres is one that is disordered but does not have any mechanisms when compressed, that is, no spheres slide upon another under a macroscopic load. The arrangement of seed points itself does not likely correspond to a jammed packing as the likelihood of randomly generating such a structure is extremely low. The relatively high density of the hard spheres however produces a reasonably uniform yet random distribution of seed points. The coordination number, $b$, for each seed was chosen to be large enough to account for all the necessary facets but does not necessarily represent the number of facets on each cell, typically $b \approx 60$.

## 3.2 BCC Foam

The body centered cubic (BCC) foam, formed from the Voronoi tessellation of the BCC crystal structure (Figure 21, left), analogous to the first brillouin zone, has served as an idealization for real stochastic foams due to its relative simplicity and nearly isotropic properties, for example see (Daxner et al., 2006; De Giorgi et al., 2010; Fahlbusch and Becker, 2011; Fischer et al., 2009). The reciprocal polyhedron is a truncated octahedron – a type of tetrakaidecahedron (14-sided polyhedron) -- This structure is also known as the Kelvin foam as it was devised by Lord Kelvin in 1887 as the solution to the minimization of surface energy of an array of bubbles (Thomson, 1888). Lord Kelvin's actual solution has curved walls but the curvature is so slight that it is not discernible to the naked eye. Using shell finite elements (Grenestedt, 1999) found that the BCC foam has a bulk modulus that is more than 99% of the Hashin-Shtrikman (H-S) upper bound at relative densities up to 10%.

**Table 1. – Quasi-random foam parameters**

**Seed Parameters**

| Model name | *RF20-1%-1* | *RF20-1%-2* | *RF12-2%-1* | *RF20-2%-1* | *RF20-2%-2* | *RF12-4%-1* |
|---|---|---|---|---|---|---|
| Number of seeds (n) | 20 | 20 | 12 | 20 | 20 | 12 |
| Wall thickness ($t/L$) (%) | 1.0 | 1.0 | 2.0 | 2.0 | 2.0 | 4.0 |
| $\beta$ (from Eqn. 84) | 0.50 | 0.50 | 0.50 | 0.50 | 0.50 | 0.61 |
| Scale factors (g) | 1.0 | 1.0 | 1.0 | 1.0 | 1.0 | 1.0 |
| Coordination (b) | 30 | 30 | 30 | 30 | 30 | 30 |
| Poison's ratio $\nu_s$ | 0.3 | 0.3 | 0.3 | 0.3 | 0.3 | 0.3 |
| Density ($\bar{\rho}/\rho_S$) (%) | 7.65 | 7.67 | 12.53 | 14.69 | 14.70 | 24.25 |
| Ratio: biggest/ smallest grain | 2.43 | 2.63 | 1.94 | 2.36 | 2.89 | 3.08 |

## 3.3 Simple Cubic foam

The simple cubic (SC) foam is formed by the tessellation of a seeding of a single point in a cubic unit-cell. The unit cell is chosen so that the vertex is located at the center of the RVE (Figure 21, right). The most characteristic feature of the SC lattice is the high degree of material alignment where 1/3 of the material lies in a plane aligned with each base vector. When stressed along these axes 2/3 of the material will be under uniform compressive or tensile stress resulting in highly stretch dominated behavior. The very simple arrangement of material in the SC will provide insight into the role of material alignment in regards to stiffness and isotropy in a later section. In the low density limit the SC foam achieves the Hashin-Shtrikman (H-S) upper bound for bulk modulus (Grenestedt, 1999).

## 3.4 FCC

The reciprocal polyhedron of the face centered cubic (FCC) foam is a rhombic dodecahedron (Figure 22, top-right) – a twelve sided polyhedron with identical rhombic faces. This structure was first identified by Plateau (1873). While it was mentioned by (Daxner, n.d.) as a model for closed cell foams, an investigation into its mechanical properties was not found. It has been referred to as a 3-D honeycomb due cross-sections being characteristically hexagonal (Figure 22). The regularity of the geometry results in nearly isotropic stiffness.

### 3.5 Diamond

Using the diamond crystal structure as a seeding produces cells with four octagonal and 12 triangular faces (Figure 25, top-center). They are truncated tetrahedrons whose four vertices are each replaced by three triangular faces arranged pyramidally. As will be seen from the results in section 4, the diamond foam (DF) is characterized by portions that are highly aligned (Figure 25, middle-right, bottom-left and bottom-center) and regions that are not (Figure 25, center and bottom-right).

### 3.6 Octet-truss & -foam

The octet-truss (OT) structure (Figure 24, top-left) is a fully triangulated truss structure shown to have stretch dominated shear stiffness (Deshpande et al., 2001). It consists of a central octahedron with corners that lie on the center faces of a cubic unit cell. Each face of the octahedron shares as a face with a tetrahedron whose opposite corner lies on a corner of the unit cell. Its stretch dominated behavior results in stiffness and strength that exceeds that of comparable metal foams by factors of 3-

10 (Deshpande et al., 2001). It has been identified as an uniquely efficient material, as it is a triangulated and stretch dominated truss structure composed of members of a single length, and has been included in this study as benchmark for comparison with other designs.

The octet-foam (OF) is an analogous closed cell foam to the OT. It shares the same edges and vertices as the OT but has walls that connect the edges of the tetrahedrons. Out of the structures investigated by (Vigliotti and Pasini, 2012) it was one of the highest performing in terms of stiffness and strength and deemed the highest performing overall due to its nearly isotropic properties. Our findings however, supported both quantitatively and qualitatively, discount the claim of near isotropy.

The OF and the DF are related through their seeding pattern. If the four internal seeds of the DF, those that do not lie on an RVE face, are mirrored into the remaining four unoccupied octants the seeding pattern for the OF is formed. The tessellation into the OF is done by ascribing a relative growth factor to the corner and face-centered octahedral cells of $g = 2$.

### 3.7 BFC foam

By using the FCC seeding and adding a body centered seed point results in the geometry shown in Figure 23. This foam possess three types of cells – a cubic cell that resides at the center of the chosen RVE, this is surrounded by six 14-sided polyhedra (Figure 23 - dark green & dark blue) each having two square faces, four rhombohedral faces and eight triangular faces (this shape being a truncated rhombic dodecahedron), and a dodecahedral cell at the corners of the RVE. This structure can been seen as a hierarchical material having a SC unit cell surrounded by a matrix of different, more compliant, morphology. The SC foam is found to be stiff relative to the BCC and FCC foams, making for a distinct heterogeneity in properties between cells. This can be exploited to achieve a multiphase collapse mechanism where the first phase is the elastic or plastic collapse of the compliant phase/cells and partial densification followed by the interaction of the stiffer phase and an increase in stiffness and strength.

### 3.9 Dodecahedral-pyramidal foam

The dodecahedral-pyramidal foam (DDPF) gets its name from the reciprocal polyhedrons being a centrally located dodecahedron surrounded by, and sharing faces with, 12 four-sided pyramidal cells. This is similar to the OF unit cell which consists of octahedrons who share faces with tetrahedrons arranged in a BCC pattern, where the dodecahedral triangulated foam consists of rhombic dodecahedra who share faces with rhombic pyramids, also arranged in a BCC pattern.

Despite any perceived geometric complexity, the DDPF geometry bears some simple relations born from its highly ordered nature. The aspect ratio of the base of the rhombic pyramids is $\sqrt{2}$. The faces are obtuse isosceles triangles whose ratio of edge lengths is $\sqrt{3}/2$. The long edge of the triangular faces forms the long ridge of the rhombic pyramids and has equal length to the short dimension of the pyramid base. The rhombic dodecahedron has 12 identical rhombohedral faces and stacks by itself to fill space in an FCC fashion. The reciprocal unit cell is analogous to the first stellation of the rhombic dodecahedron, also known as Escher's Solid due to its appearance in many of the artist's work, however the original cell walls of the dodecahedron are retained in this case.

Another similarity between the OF and the DDPF is seen when examining an alternate unit cell of the OF (Figure-8, top-right). It is formed from two interpenetrating rhombohedral prisms whose aspect ratios are $\sqrt{2}/2$ and serves as the inspiration for the DDPF. The dodecahedral triangulated foam is formed analogously by three interpenetrating square prisms (Figure 26, top-left). To our knowledge this geometry has not yet been investigated for its mechanical properties. This geometry was created manually with the ABAQUS CAD module.

### 3.9 X-Foam

The X-Foam (XF) is a sister structure to the DDPF in that it also consists of three interpenetrating orthogonal prismatic members whose cross-sections are also composed of orthogonal members, but differ in the relative orientation of cross-sections. This geometry tessellates space into skewed tetrahedrons whose adjacent edges differ in length by a factor of $\sqrt{3}/2$. To our knowledge this is the first description and analysis of this structure**.** This geometry was created manually with the ABAQUS CAD module.

### 3.10 OF+SC Foam

The OF+SC foam is a combination of, what will be shown to be, the two most anisotropic materials; the OF being stiff in shear and the SC being stiff axially, tessellating space into regular and irregular tetrahedra. The result is a material with highly aligned and but well distributed material. The OF and SC parts were formed separately where the SC wall thickness is chosen to match the dimension of the OF on the edge on the unit cell, equal to $\sqrt{3}t$, where $t$ is the wall thickness of the OF foam. To our knowledge this is the first description of this material.

# *4. Results*

The results section is broken down in the following manner: A baseline result of sorts is formed by comparing the FE predictions for foams formed from the quasi-random distribution of seed points to available data for the axial and shear stiffnesses of polymer and metal foams as well as analytical models. Next, four previously studied designs, the BCC, FCC, SC, and OF, are shown to compare favorably with historical results to further validate the modeling scheme. Through this investigation some insight is gained into the morphological features that give rise to higher performance designs. The following set of results then introduces five novel designs. Three of these foams, the XF, DDPF and OF+SC, are found to have maximal stiffness, that is, the sum of their Young's, shear and bulk moduli approaches the sum of the respective Hashin-Shtrikman (H-S) upper bounds as the relative density (cell wall thickness) approaches zero.

Three classes of materials are identified including two classes of high performance foams. High-performance foams have a stiffness approximately equal to the ideal isotropic stretch dominated foam or lattice, where one third of the material is stretched under an arbitrary load, as described in (Ashby, 2011). Foams with maximal-performance have a total stiffness that converges, at the low density limit, to that of an isotropic material that achieves the H-S upper bound for axial, shear and bulk modulus. The remaining group contains the materials that have stiffness less than that of the high-performances materials; all closed cell foams were within ~5% of the high performance group while only truss structures and foams with walls removed (omitted for brevity) are in the lowest performance group.

The simple cubic (**SC**), Octet-foam (**OF**), X-foam (**XF**), dodecahedral-pyramidal-foam (**DDPF**) and the **OF+SC** designs all have maximal stiffness. The quasi-random (**QR**), body centered cubic (**BCC**), face centered cubic (**FCC**) and Body+Face centered (**BFC**) are high-performance, having stiffnesses similar to that predicted for stretch dominated lattices. The diamond foam (**DF**), for reasons discussed in section 4.3, is the only material that is a hybrid of sorts between maximal- and high-performance foams. Only one material, the octet-truss (**OT**), was found to be in the low-performance class.

The stiffness of **QR** foams are shown to be consistent with empirical results for stiff foams, analysis by (Gibson and Ashby, 2009), as well as FE results for similar foams studied by (Roberts and Garboczi, 2001). Results for the **BCC** and **SC** foams are consistent with results obtained by (Grenestedt, 1999). Results for the **OT** truss are consistent with those obtained by (Deshpande et al., 2001) at low densities. At higher relative densities results obtained in this study suggest the structure is stiffer than previously predicted.

## 4.1 Quasi-Random Foam Stiffness

The axial, shear and hydrostatic stiffness of quasi-random (**QR**) foam geometries agree well with experimental results, analytical predictions for stretch dominated foams (Figure 29) and a FE study of similar structures (Figure 31). The stiffnesses reported are the tangent moduli at macroscopic stains of $\epsilon = \bar{\varepsilon}_{ii} = 0.1\%$. For the shear case the stiffness is measured at an applied shear strain is $\bar{\gamma}_{ij} = \epsilon/2$ and for the hydrostatic case the volumetric strain is $e = 3\epsilon$. While absolute strains of 0.1% are not generally considered infinitesimally small the tangent moduli are found to be constant for macroscopic strains, $\epsilon \lesssim 0.4\%$, in all cases.

Quasi-random foam geometries were generated as a benchmark for more ordered geometries and not necessarily to be representative of stochastic foams. Seed points are based upon random dense packings of spheres using the hard sphere seeding algorithm detailed in Section 2.2. Unlike stochastic foams these structures have uniform wall thicknesses, a narrow distribution of cell sizes and aspect ratios, and no curved features. The structure of stochastic foams are heavily influenced by the chemistry and process of foaming and solidification resulting in local variations in cell wall thickness, cell size, aspect ratio, curvature and potentially material properties influenced by crosslinking or solidification upon cooling. Although there are many differences between the geometries of stochastic foams and these **QR** foams their stiffness are quantitatively consistent in the case of stiff stochastic foams.

Normalized axial stiffnesses for six quasi-random foam geometries are plotted along with aggregated empirical data for closed cell foams taken from (Gibson and Ashby, 2009) (Figure 29). Three axial moduli are calculated for each model corresponding to a compressive stress applied normal to three orthogonal faces of the RVE. Average values differ only slightly from $E_{11}, E_{22}$ and $E_{33}$ even though models consist of only either 12 or 20 unique cell geometries, and the uniformity of the cells is perhaps not so low (Table 2). There is more scatter in the various moduli for the geometries composed of 12 cells versus those composed of 20 cells but this difference is only significant at the highest relative density plotted, $(\bar{\rho}/\rho_S) =$ 24.3%. Two curve fits are shown using Equations (78) and (79) using $\phi = 0.6$ and $\phi = 0.0$ (Figure 29), the former being the curve fit used in (Gibson and Ashby, 2009) to match empirical data for stiff foams and the latter corresponding to open cell foams. FE results agree well with analytical models and are quantitatively consistent with the behavior of real stochastic foams. In an isotropic material the response from axial and shear loading cannot differ substantially due to the relatively small difference between principal stress states in the two cases which should not result in a dramatic change in behavior. It is unclear why the measured shear stiffnesses are so low.

Normalized shear stiffnesses, $(\bar{G}/G_S)$, are nearly identical in value to the normalized axial stiffnesses, $(\bar{E}/E_S)$ (Figure 31, left and center) making them nearly isotropic by Equation (73) (Table 2). The normalized bulk moduli, $(\bar{K}/K_S)$, is also nearly identical in magnitude, although the bulk modulus is not included in the isotropy calculation. The bulk moduli are very close to the Hashin-Shtrikman (H-S) upper bound for bulk modulus (Figure 29, right pane, heavy dashed lines) (Equation 74). The moduli are calculated in two ways, 1) directly from the application of a volumetric stress, and 2) from the application of an axial stress and the assumption of isotropy. Two effective bulk moduli are calculated from the two Poisson ratios associated with the application of an axial stress for a total of six Poisson ratios and six bulk moduli which are then averaged. The average of the six bulk moduli yields a value nearly identical to that found from direct calculations involving a volumetric strain.

Examples of stress distributions are shown in Figure 30. What are plotted are local stress normalized by the applied Von Mises (VM) stress, or the applied stress in the case of hydrostatic loading as the VM stress is zero (in either case a homogeneous material will have a normalized stress of unity), at macroscopic strains of $\epsilon = 0.1\%$, scaled 100x for clarity. The distribution of stress between the 12-cell model with $\bar{\rho} = 12.53\%$ (Figure 30, top) and the 20-cell model with $\bar{\rho} = 7.65\%$ (bottom) are qualitatively the same. The magnitude of stress concentrations are inversely proportional to the relative density due to the fact that local strain energy densities increase with decreasing relative density for a given macroscopic strain energy density.

Stress concentrations are lower under macroscopic hydrostatic loading (Figure 30, left) than under axial or shear cases (left and middle respectively). Uniform stress distributions coupled with mostly affine strains are characteristic of stretch dominated behavior. In fact, the six **QR** foams listed in Table 2 have bulk moduli within 8% of the H-S upper bound. Strain energy densities are fairly uniform in the hydrostatic case relative to axial and shear loading.

***Table 2. Quasi- Random Properties***

| Name - | *RF20-1%-1* | *RF20-1%-2* | *RF12-2%-1* | *RF20-2%-1* | *RF20-2%-2* | *RF12-4%-1* |
|---|---|---|---|---|---|---|
| $(\bar{E}_{11}, \bar{E}_{22}, \bar{E}_{33})/E_s$ (%) | 2.7, 2.8, 2.9 | 2.8, 2.9, 2.8 | 4.7, 4.9, 5.0 | 5.7, 5.7, 5.9 | 5.7, 5.7, 5.9 | 11.5, 10.3, 10.4 |
| $(\bar{G}_{12}, \bar{G}_{13}, \bar{G}_{23})/G_s$ (%) | 2.8, 2.8, 2.8 | 2.8, 2.7, 2.8 | 4.6, 5.0, 4.7 | 5.8, 5.9, 5.8 | 5.7, 5.8, 5.8 | 10.9, 10.4, 10.5 |
| $\bar{E}_{avg}/E_s$ (%) | 2.8 | 2.8 | 4.9 | 5.8 | 5.8 | 10.7 |
| $\bar{G}_{avg}/G_s$ (%) | 2.8 | 2.8 | 4.8 | 5.8 | 5.8 | 10.6 |
| $\bar{K}/K_s$ (%) | 2.9 | 2.9 | 4.9 | 5.9 | 5.8 | 10.1 |
| $\bar{K}/K_{HSU}$ (%) | 94.4 | 95.3 | 95.6 | 95.4 | 94.5 | 92.9 |
| Poison's ratio $\bar{\nu}_{avg}$ | 0.306 | 0.304 | 0.303 | 0.303 | 0.303 | 0.288 |
| Isotropy $(a)$ | 0.998 | 0.964 | 0.982 | 0.991 | 0.995 | 0.986 |
| Density $\bar{\rho}$ (%) | 7.65 | 7.67 | 12.53 | 14.69 | 14.70 | 24.25 |

The Poisson ratio of quasi-random foams is ~1/3 (Table 2) which matches the semi-empirical formula offered by (Gibson and Ashby, 2009),

$$\bar{\nu} \approx \frac{1}{3}. \tag{85}$$

The average Poisson ratio of 0.301 is nearly that of the constituent, $\nu_s = 0.3$. While the octet-truss was found to be insensitive to the Poisson ratio of the constituent material (Deshpande et al., 2001) the stiffness of the BCC foam varies by

~25% going from $\nu_s = 0.45$ to 0.0 (Grenestedt, 1999). In this study $\nu_s = 0.3$ and is not varied for the sake of brevity.

In a remarkable result Equations (78) and (79) fit nearly perfectly with results for the average axial, shear and bulk moduli respectively when $(\bar{\rho}/\rho_S) \lesssim 25\%$, using $\phi = 2/3$ (Figure 31). The R$^2$ values are 0.998, 0.997 and 0.987 for the axial, bulk and shear moduli respectively for relative densities below ~25%. Plotted for contrast are third-order polynomial curve fits for $(\bar{E}/E_S), (\bar{G}/G_S)$ and $(\bar{K}/K_S)$ which only diverge from Equations (78) and (79) for $(\bar{\rho}/\rho_S) \gtrsim 40\%$ for $(\bar{E}/E_S)$ and $(\bar{G}/G_S)$. These third-order fit shows excellent agreement with the FE results for similar quasi-random foams studied by (Roberts and Garboczi, 2001). The performance of the **QR** foams is consistent with the assumption that in stretch dominated isotropic materials in three-dimensional space one third of the material will be favorably oriented to support an applied compressive load. That is, one third of the material will be in nearly pure tension or compression while the remainder will be largely bent. For the **QR** foams with $(\bar{\rho}/\rho_S) \lesssim 25\%$ the axial and shear stiffnesses are nearly perfectly predicted by this assumption and the application of Equations (78) and (79).

## 4.2 BCC, FCC, SC, OF and OT Stiffness

Having established the isotropic stretch dominated nature of foams generated from quasi-random arrangements of seed points using the hard sphere model we turn our attention to more ordered geometries. Shown in Figure 32 are the results for the **BCC**, **FCC**, simple cubic (**SC)**, octet-foam (**OF**) and octet-truss (**OT**). Finite element results are plotted along with associated third-order polynomial curve fits and theoretical upper bounds. Plots of $(\bar{E}/E_S)$ and $(\bar{G}/G_S)$ against $(\bar{\rho}/\rho_S)$ indicate the performances of the **SC** and **OF** are not limited by the H-S upper bounds (Figure 32, top row). The **BCC**, **FCC**, **OF** and **SC** foams all have bulk moduli very near the H-S upper bound (HSUB) on bulk modulus over the range of relative densities studied.

The **SC** foam and the **OF** have stiffnesses in excess of the HSUB on axial and shear moduli respectively. The H-S bounds were developed for nearly isotropic materials while the **OF** and **SC** foams have a high degree of anisotropy, being the two most anisotropic of the geometries studied. However there remains a relationship with the performance of all materials as there is an apparent tradeoff between axial and shear stiffness relative to the HSUB. The **SC** foam as an example has the highest axial modulus and the lowest shear modulus. This tradeoff is quantified in Figure 35 and discussed later in section 4.3.

The bulk moduli of the **BCC**, **FCC**, **SC** and **OF** nearly all achieve, but never exceed, the HSUB (Figure 32, upper-right). To visually expand the tightly grouped results the effective bulk modulus is normalized by the HSUB (Figure 32, bottom-right). The results for the bulk modulus of the **SC** and **BCC** foams agree with those obtained by (Grenestedt, 1999) in the low density limit, however our model predicts $(\bar{K}/K_{HSU}) = 99.4\%$ at $(\bar{\rho}/\rho_S) = 10\%$ while their model predicts a slightly higher value of $(\bar{K}/K_{HSU}) = 99.7\%$ at that density. Although these materials are not isotropic, the bound on bulk modulus is still applicable for these and all materials. The reason for this is discussed most appropriately while analyzing the **SC** foam later in this section, but stems from the fact that bulk stiffness does not depend on isotropy. Because the Voigt bound is rigorous for all materials it is used to further normalize results for axial and shear moduli (Figure 32, bottom-left and -center).

Plots of $(\bar{E}/E_S)/(\bar{\rho}/\rho_S)$ and $(\bar{G}/G_S)/(\bar{\rho}/\rho_S)$ (Figure 32, bottom-left and –center) are largely measure of the stretch dominated nature of a material and may be interpreted by considering the contours of Equations (78) and (79) for different values of ϕ (dashed lines, left and center respectively). When these equations are divided by the relative density, $(\bar{\rho}/\rho_S)$, the result is linear with $(\bar{\rho}/\rho_S)$ where the $y$-intercept is the stretching component of the stiffness. For instance, ~1/3 of the material in the isotropic **QR** foams is stretched under load making the $y$-intercept in these plots for their shear and axial performance both ~1/3. Plots of $(\bar{E}/E_S)/(\bar{\rho}/\rho_S)$

and $(\bar{G}/G_S)/(\bar{\rho}/\rho_S)$ represent the stiffness efficiency of a material as the achievement of the Voigt bound indicates uniform stretching.

The isotropy, $a$, for all ten foam geometries are plotted in Figure 36, left. The definition of isotropy, Equation (73), allows for the consideration of materials without cubic symmetry. It is qualitatively and nearly quantitatively identical to the ratio $(C_{1111} - C_{1122})/2C_{1212}$. If used in place of $\left(\bar{E}_{avg}/\bar{G}_{avg}\right)$ in Equation (73) the results for the **BCC** foam differ by only ~1-2%. The boundary conditions used to calculate $C_{1111}$, $C_{1122}$ and $C_{1212}$ are detailed in (Grenestedt, 1999). The greater the degree of anisotropy the more the two ratios deviate but never to the degree that significantly influences this results of this study.

To help quantify the behavior of these foams FE data is fit to third order polynomial curves. The coefficients are forced to be positive and pass through the real data points of (0,0) and (1,1), corresponding to empty space and a fully dense solid respectively (Equation 81). The positive coefficients were enforced to conform with analysis by (Gibson and Ashby, 2009; Grenestedt, 1999) who that found the stiffness of foams is the summation of contributions from material being bent and stretched. The accuracy of the curve fits is very good with the average $R^2$ value being 0.9999 and RMSE values all fits are less than 0.0078; the average RMSE is 0.00187. The same curve fits are plotted top and bottom (left and center) (Figure 32). Due to the scaling in the bottom row plots of $(\bar{E}/E_S)/(\bar{\rho}/\rho_S)$ and $(\bar{G}/G_S)/(\bar{\rho}/\rho_S)$

the third order accuracy of the curves is apparent highlighting the discrepancies, notably in the axial stiffness of the **OT** and the shear stiffness of the **SC**.

***Table 3. Curve Fit Coefficients of Equation (81) – Young's Modulus***

| Name - | $C_1$ (%) ▼ | $C_2$ (%) | $C_3$ (%) | $R^2$ | RMSE ($10^{-4}$) |
|---|---|---|---|---|---|
| OT | 14.8 | 0 | 85.2 | 1.0000 | 13.62 |
| BCC | 33.5 | 12.5 | 54.0 | 1.0000 | 2.22 |
| QR | 33.8 | 36.4 | 29.8 | 0.9997 | 24.65 |
| DF | 33.9 | 0 | 66.0 | 0.9999 | 24.83 |
| FCC | 34.7 | 19.9 | 45.4 | 1.0000 | 1.79 |
| BFC | 34.8 | 37.0 | 28.2 | 1.0000 | 26.33 |
| OF | 35.5 | 0 | 64.5 | 1.0000 | 17.02 |
| XF | 44.9 | 0 | 55.6 | 1.0000 | 25.05 |
| DDPF | 45.3 | 0 | 54.7 | 1.0000 | 22.25 |
| OF+SC | 51.6 | 0 | 48.4 | 1.0000 | 19.52 |
| SC | 71.7 | 0 | 28.3 | 1.0000 | 1.04 |

***Table 4. Polynomial Curve Fit Coefficients –Shear Modulus***

| Name - | $C_1$ (%) ▼ | $C_2$ (%) | $C_3$ (%) | $R^2$ | RMSE ($10^{-4}$) |
|---|---|---|---|---|---|
| OT | 24.4 | 30.0 | 45.6 | 1.0000 | 2.38 |
| QR | 32.4 | 45.7 | 21.9 | 0.9995 | 77.63 |
| FCC | 32.6 | 45.4 | 22.0 | 1.0000 | 1.20 |
| SC | 33.0 | 0 | 66.7 | 1.0000 | 1.27 |
| BFC | 33.6 | 30.1 | 36.2 | 1.0000 | 2.18 |
| BCC | 34.1 | 49.3 | 16.5 | 1.0000 | 2.46 |
| DF | 49.3 | 41.8 | 8.8 | 0.9999 | 37.17 |
| OF+SC | 53.7 | 0 | 46.3 | 1.0000 | 6.24 |
| XF | 58.8 | 0 | 41.2 | 1.0000 | 10.23 |
| DDPF | 59.4 | 0.7 | 39.9 | 1.0000 | 7.08 |
| OF | 65.2 | 0 | 34.6 | 1.0000 | 19.07 |

The curve fit coefficients for all eleven foam geometries are listed in **Table 3** and **Table 4**, results are ordered by the linear term. While the G-A models, Equations (78) and (79), define stiffness in terms of a linear and quadratic component many of the models (curve fits) do not, perhaps surprisingly, involve a quadratic term. Instead the curve fits have just a linear and cubic dependence. This is more consistent with (Grenestedt, 1999) who attributes a cubic contribution from the bending of plate-like members in closed cell foams.

The **SC** foam has almost precisely the expected stretching components ($C_1$): two thirds of the material under axial compression, plus an additional amount for the stretching of the remaining perpendicular plane from the Poisson effect, and one of three walls under shear (Table 3 & 4).

The **SC** foam has the highest axial modulus of all foam geometries, and likely any material with cubic symmetry, but it is also the most anisotropic. All of the material is equally partitioned into orthogonal planes that are aligned with the base vectors. Under axial macroscopic loading two regions of relatively uniform stress develop (Figure 33, top-left). Two of three cell walls are placed in nearly pure compression with relatively high strain energy density while the remaining orthogonal wall is placed in tension, to accommodate the lateral Poisson expansion, and at a relatively low strain energy density. Under these conditions it can be expected that two-thirds of the material will contribute to the stiffness in a manner directly proportional to the relative density while the remaining bit of material will make a small contribution to the stiffness with no significant bending taking place anywhere. Plotted in Figure 32, bottom-left, is the axial stiffness for the **SC** foam along with contours (light-dashed lines) of Equation (78) for different values of $\phi$. The linear term in Equation (81), also the $y$-intercept, is 0.71, which agrees well with this analysis in the low density limit where the cubic term makes a negligible contribution.

The shear stiffness of the **SC** foam is also well predicted, having a linear stretching component of $C_1$=0.33. In both polynomial models for axial and shear stiffness there is no quadratic term indicating the stiffness is best predicted assuming only the stretching and bending of cell walls, contrary to the G-A model. The apparent third order behavior may be due, in part, to partitioning of strain energy and nonlinear changes in geometry. At higher relative densities relatively more material resides in edges and vertices than at lower densities. In the case of macroscopic shear the edge material in the highly stressed cell walls is constrained by unstrained material in the intersecting wall at low strain (Figure 33, bottom-right). The constrained material in the edge has a lower strain energy density than it would if it resided in the cell wall; material in vertices is further restrained by the other intersecting wall and possesses an even lower strain energy density. The relative strain energy densities in the vertices, edges and faces in the cell walls under maximum stress are ~1.0:2.2:4.7 for macroscopic shear loading at $t/L$ =20%. The result is a relative degradation in performance with increasing relative density proportional to the volumes of material in walls, edges and vertices and their strain states. This is certainly a competing factor with the proportional increase in stiffness with relative density in Equation (81). In a more accurate model the components would themselves be a function of relative density, $C_i = C_i(\bar{\rho}/\rho_S)$.

Previous work has shown that the bulk modulus of the **SC** foam achieves the H-S upper bound in the low density limit (Grenestedt, 1999). At the lowest density FE calculation, $(\bar{\rho}/\rho_S) = 5.88\%$, the effective bulk modulus is 99.4% of the HSUB with the performance approaching the bound as $(\bar{\rho}/\rho_S) \rightarrow 0$ (Figure 32, bottom-right). As relative density increases there is a monotonic decrease in performance relative to HSUB on bulk modulus, which is a characteristic of all geometries. As the wall thickness goes to zero the relatively inhomogeneous regions of strain energy density associated with the edges and vertices shrink to zero and the system approaches a state of uniform strain energy density. In this case where $(\bar{\rho}/\rho_S) \rightarrow 0$, $(K_{HSU}/K_S)/(\bar{\rho}/\rho_S) \rightarrow {\sim}0.38$ which is low compared to $(E_{HSU}/E_S)/(\bar{\rho}/\rho_S) \rightarrow {\sim}0.50$ and $(G_{HSU}/G_S)/(\bar{\rho}/\rho_S) \rightarrow {\sim}0.53$. This indicates that in a structure composed of plate-like members subject to macroscopic hydrostatic compression, such that all the walls are uniformly compressed in their plane, can at most have a strain energy density that achieves $\lesssim 40\%$ of the stiffness of a uniform continuum having equivalent elastic properties and density, $E = E_S(\bar{\rho}/\rho_S)$, $\rho = \bar{\rho}$ and $\nu = \bar{\nu}$. This is a substantially lower potential than the axial and shear moduli. It seems that hydrostatic straining/confinement of material on the local level is necessary to achieve macroscopic bulk stiffness.

The relationship between the performance of the **SC** foam and the Voigt and H-S upper bounds are made clearer through a simple thought experiment. For simplicity, consider the low density limit where the material fraction in edges and vertices is negligible. Under an axial load two thirds of the material experiences a uniform stress, while the remaining material is relatively unstressed. The majority of the strain energy is stored through stretching making the stiffness of this material is at least 2/3 of the Voigt bound, a value of at least 0.66 in Figure 32. Imagine then transferring the material from the unstressed region to the stressed region. The result is a material with uniform strain energy density that achieves the Voigt bound, well exceeding the HSUB. It is clear that no further rearrangement of material will allow for a higher average strain energy density. If the axial load is then removed and a shear stress is applied on an orthogonal plane, the structure will provide no resistance as the rotational stiffness of

the walls are zero. This can be envisioned by taking the stress state depicted in Figure 33, top-center, and transferring the highly stressed material under compression to the orthogonal planes being bent and at relatively low stress. The stiffness will be entirely determined by the bending of plate-like members that will provide no resistance in the low density limit, where the wall thicknesses go to zero. It is evident then that there is an inherent tradeoff between directional stiffness and isotropy. It is for this same reason that the bounds on bulk modulus still applies to anisotropic materials as unlike the case of axial and shear loading, there is no opportunity to compromise stiffness in one direction for compliance in another.

The performance of the **BCC** and **FCC** foams are similar to that of the **QR** foams (Figure 32, bottom-left and -center). All three are based upon dense sphere packings and are all nearly isotropic. The **FCC** is more isotropic than the **BCC,** performing nearly identically to the **QR** foams, with which it shares the same shear stiffness qualitatively (Figure 32, center). While these curve fits seem to overlap the coefficients differ significantly (Table 4). Historically the **BCC** foam has been used as a simple model for stochastic foams however the **FCC** model is found to be closer in performance. The **BCC** foam has likely received more use because a slight variant, the Kelvin foam, a **BCC** foam with imperceptibly curved walls, was the long standing solution to the problem of minimizing surface energy in an array of bubbles (Thomson, 1888). Both the **BCC** and **FCC** have stretch dominated near isotropic performance where ~1/3 of the material is stretched irrespective of the loading direction.

While the **FCC** and **QR** foams qualitatively share the same shear stiffness their coefficients in Equation (81) for shear modulus are quite different (Table 4). The stretching component of the **FCC** foam is nearly what is expected from the geometry, $C_1 = 32.6\% \approx 1/3$. Under macroscopic shear loading the principal stress align with one third of the cell walls placing them primarily in tension or compression, while the remaining walls deform primarily through bending. The normalized strain energy densities in the center of a wall being stretched and being bent are however 1.3 and 0.5 respectively in the **FCC** foam with $t/L = 2\%$ (Figure 34, top-center) indicating that some stretching is taking place in all walls. This simple partitioning of material into static regions being bent and stretched, as in Equations (78) and (79), does not fully account for the more complex behavior seen the **FCC** and **BCC** foams. From the curve fit coefficients in **Table 3** and **Table 4** it seems clear that a combination of second and third order contributions are necessary to account for the stiffness of many of these foam geometries; and no model's stiffness is well predicted by just first and second order contributions, as the data sets do not lie along contours of Equations (78) and (79) (Figure 32, bottom-left and –center), with the exception of the **QR** foams, and those that share similar performance, at low densities, as discussed in the previous section.

The apparent tradeoff between axial and shear performance in every material seen in Figure 32, relative to the HSUB, is seen in all materials. In the case of the **FCC** and **BCC** foams their performances parallel each other, with $(|\bar{E}_{BCC} - \bar{E}_{FCC}|/E_S) \approx (|\bar{G}_{BCC} - \bar{G}_{FCC}|/G_S) \approx$ 2-3%, with their bulk moduli being nearly identical. To help quantify the total stiffness of these materials their performance can be related to an ideal isotropic material having shear, axial and bulk moduli that are equal to the theoretical bounds derived by (Hashin and Shtrikman, 1963).

In Figure 35 two measures of the total stiffness are plotted,

$$\Omega = \frac{\bar{E} + \bar{G} + \bar{K}}{E_{HSU} + G_{HSU} + K_{HSU}}, \tag{86}$$

$$\Psi = \frac{a(\bar{E} + \bar{G} + \bar{K})}{E_{HSU} + G_{HSU} + K_{HSU}}. \tag{87}$$

On the right (Equation (86)) the summation of the axial, shear and bulk moduli are normalized by the sum of the moduli of the ideal material,(a material that achieves the H-S bounds for bulk, shear and Young's modulus); this same quantity is plotted again multiplied by the isotropy, $a$ (Figure 35, left) (Equation (87)). In both cases a material with maximum isotropic stiffness will have a value of unity. The scaling factor, $a$, is somewhat arbitrary in magnitude and may overly penalize anisotropic materials, but serves as a means of differentiating the tightly grouped performances plotted in Figure 35, right.

The total stiffness of the **BCC** and **FCC** foams is found to be the same, $\boldsymbol{\Omega_{FCC}} \approx \boldsymbol{\Omega_{BCC}}$, differing by only ~0.5% at $(\bar{\boldsymbol{\rho}}/\boldsymbol{\rho_S}) = \mathbf{50\%}$ and converging as $(\bar{\boldsymbol{\rho}}/\boldsymbol{\rho_S}) \to \mathbf{0}$ (Figure 35, right). Not only are the total stiffness of the **BCC** and **FCC** nearly identical but are also nearly identical to that of the **QR** and **BFC** foams. The **QR** perform slightly better than the more ordered foams at $(\bar{\boldsymbol{\rho}}/\boldsymbol{\rho_S}) \gtrsim \mathbf{35\%}$ which is likely due to poorer mesh quality at the two highest relative densities calculated for the **QR** foams as a result of limitations in the meshing scheme employed. Plots of Ω appear to arrange the materials into distinct groups.

There are three regimes of material performance (Figure 35, right). Most notably there is a group of materials whose performance converges on unity, $\Omega \rightarrow \sim 1$, at the low density limit. Only one of these materials is isotropic yet they all have a total stiffness that is bounded by the H-S bounds. There is a monotonic decay in performance with increasing relative density in all designs suggesting a fundamental limit and laxity of the HSUB. A design created by topology optimization to be isotropic with have maximum shear modulus (Radman et al., 2012) has $\bar{G}/G_{HSU} = 98.8\%$, $\bar{E}/E_{HSU} = 96.2\%$ and has a total stiffness, $\Omega = 93.8\%$ at $(\bar{\rho}/\rho_S) = 40\%$, coincident with the performance of the **OF+SC** foam (Figure 35, right), discussed in the next section. All of the designs with maximal performance, which in this group includes only the **SC** and **OF**, have cell walls that are continuous between neighboring cells, unlike other designs.

The defining characteristic of the maximum performance designs is the continuous nature of the cell walls. This feature of the **OF** can be more clearly seen in an alternative unit cell constructed from two interpenetrating thin walled prismatic members with rhombohedral cross-sections (Figure 26, top-right). This unit cell is formed by truncating four parallel edges of the unit cell pictured in Figure 24, top-center, so as to remove half the material. Both the **SC** and **OF** are very stiff in the directions aligned with their cell walls.

The **OF** may possess the highest shear stiffness possible for a material with cubic symmetry as all of the material is aligned with a principal stress direction resulting in a material that is nearly uniformly stressed through stretching (Figure 37, top-center). Only the material in the edges and vertices experiences a variation in stress state. In the low density limit where the material in the edges and vertices goes to zero the structure would possess uniform strain energy density. Being that there is no other arrangement of material that can possess a higher average strain energy density under shear loading the **OF** must possess maximum shear stiffness in the low density limit. A similar argument can be made that the **SC** foam possessing the maximum axial stiffness of any material with cubic symmetry. In the next section it will be shown that a combination of the **SC** and **OF** produce foam with maximal isotropic stiffness.

## 4.3 Dodecahedral-Pyramidal Foam, X-Foam, Body+Face Centered, Diamond and OF+SC Stiffness

Having calculated the stiffness of some familiar structures and finding them to agree, where results are available, with empirical data and a variety of modeling approaches, some confidence is had in exploring the results for the novel geometries presented in this section. The Dodecahedral-Pyramidal Foam (**DDPF**) and X-Foam (**XF**) are cousin to the **OF** and also in the group with maximum stiffness, having

$\Omega \rightarrow 1$ as $(\bar{\rho}/\rho_S) \rightarrow \mathbf{0}$. The Body+Face Centered (**BFC**) foam possess near isotropic stiffness with a performance that mimics the more disordered **QR** foams, having stiffnesses $(\bar{E}/E_S)/(\bar{\rho}/\rho_S)$ and $(\bar{G}/G_S)/(\bar{\rho}/\rho_S) \rightarrow \sim 1/3$ as $(\bar{\rho}/\rho_S) \rightarrow 0$. The Diamond foam (**DF**) possess unique properties in that its shear stiffness, $(\bar{G}/G_S)$, does not conform well to the polynomial model (Equation (81)). Its antisymmetric nature allows for complementary buckling at low relative densities. As $t/L$ increases compliant mechanisms have members that both shorten and thicken, stiffening the system significantly, causing energy to be stored through stretching instead of bending. A combination of the two stiffest and most anisotropic foams, the **SC** and **OF** (**OF+SC**), results in an isotropic foam that also has maximal stiffness giving it very appealing properties. All of these designs have $\bar{K}/K_{HSU}$ →~1 as $(\bar{\rho}/\rho_S) \rightarrow 0$, identical to the high performance designs, with the slight exception of the **DF** having $\bar{K}/K_{HSU} \rightarrow 0.95$, this despite having a range of performances and geometric characteristics.

The dodecahedral pyramidal foam (**DDPF**) and X-Foam (**XF**) have nearly identical elastic properties. They are both created by the extrusion of three orthogonal cross-sections that are themselves composed of orthogonal members (Figure 38, blue circles and squares); the **OF** is similarly composed of two orthogonal cross-sections. They are also in the maximal performance group having half the anisotropy of the **OF**, also being stiffer in shear than axially (Figure 38). Their bulk stiffness also approaches the HSUB as $(\bar{\rho}/\rho_S) \rightarrow 0$. Strain energy distributions in the two materials are nearly identical (Figure 37, 2nd and 3rd rows), with the **DDPF** (2nd row) having higher strain energy concentrations under axial and hydrostatic loading, suggesting a higher strength.

A third novel material, also having maximal performance, is a combination of the simple cubic (**SC**) and the octet-foam (**OF**) (**OF+SC**). A superposition of the materials with the highest axial and shear moduli yield a material whose axial, shear and bulk modulus all approach the respective HSUB as the relative density approaches zero (Figure 38). At $(\bar{\rho}/\rho_S) = 11.6\%$, the lowest relative density calculated, the **OF+SC** foam has $\bar{E}/E_{HSU} = 99.9\%$, $\bar{G}/G_{HSU} = 97.1\%$ and $\bar{K}/K_{HSU} = 98.3\%$ giving it a total stiffness, $\Omega$ =98.4% and isotropic stiffness,$\Psi =$ 96.7%, having isotropy, a = 0.983. The properties of the **OF+SC** foam make it an ideal core material for a sandwich panel.

The wall thicknesses are not uniform as the **OF+SC** foam is formed from the superposition of two independently formed geometries. The thickness of the **SC** foam cell walls was chosen to match the edge length of **OF** on the boundary edges of the **RVE,** equal to $\sqrt{3}t$, where *t* is the wall thickness of the **OF**. When the wall thickness of the **SC** is only $\sqrt{2}t$, so that all {1-0-0} cross-section members have the same apparent thickness, the isotropy drops to, $a = 0.889$ at $(\bar{\rho}/\rho_S) = 10.2\%$. The **SC** wall thickness of $\sqrt{3}t$ is the most isotropic **OF+SC** foam and a maximum value in the sense of preserving the basic geometric features. When the **SC** walls exceed this thickness they will impinge on the cells of the **OF** foam truncating the corners of the tetrahedrons. Scaling the relative wall thickness of the **SC** foam does not decrease the total stiffness, Ω, so that the anisotropy can be varied continuously between that of the **OF+SC** and **OF** foams to suit the application requirements while maintaining performance.

The diamond foam **(DF)** is the only geometry with substantial asymmetry and whose behavior is not well predicted by the cubic polynomial model. In the low density limit the shear stiffness approaches that of the **Q-R** foams but increases rapidly approaching that of the stiffest material in shear, the **OF**, when $(\bar{\rho}/\rho_S) \gtrsim 0.3$. The $R^2$ values of the curve fits (Table 3 & 4) are still very high but the different trends are seen when plotted in terms of $(\bar{E}/E_S)/(\bar{\rho}/\rho_S)$ and $(\bar{G}/G_S)/(\bar{\rho}/\rho_S)$ (Figure 38). Cross-sections reveal that the majority of the material in the **DF** is aligned in two orthogonal directions with the exception of short ligaments oriented at 45 degrees**.** As the wall thickness increases these ligaments both thicken and shorten, decreasing their aspect ratio dramatically, which increases their bending stiffness (Figure 40). As these members stiffen, compliant mechanisms in the system stiffen considerably, causing the shear stiffness of the foam to increase substantially approaching that of the stiffest material in shear, the **OF**. The presence of compliant mechanisms in a structure like the **DF** can degrade the stiffness of an otherwise highly aligned and stiff structure. The asymmetry of the design results in complementary bending of cell walls degrading stiffness relative to the degree of alignment similar to stochastic foams whose measured stiffness is often below theoretical values. This complementary buckling may result in uniform collapse and a constant collapse stress following yielding; preliminary results are in agreement with this hypothesis.

The Body+Face Centered (**BFC**) has near isotropic stiffness similar to the **Q-R** foams (Figure 38). The performance mimics that of the **QR** foams over the range of relative densities plotted in Figure 38, only lagging slightly behind in shear at higher relative densities. The **BFC** is almost isotropic and stretch dominated as are the **QR** foams but possess a much simpler geometry with more uniform strain energy distribution suggesting much higher strengths. Systems that operate near an optimum are also often near the border of a regime so it may be that the **BFC** foam will fail less catastrophically than foams in the group with maximal performance. Stretch dominated foams that do not have maximal stiffness may be more stable in their response and less likely to fail by dynamic buckling. An interesting feature of the **BFC** foam is that it can be thought of as a hierarchical structure, or two-phase system, with a stiff cubic unit cell at the center of the RVE, surrounded by a matrix of relatively compliant cells. Its large strain behavior may prove interesting when the cubic sublattice interacts to stiffen and/or strengthening the structure, depending on whether the local strains are elastic or plastic. The near isotropic stretch dominated nature of the **BFC** foam along with its two phase nature make it an interesting candidate for further study.

## *5. Discussion*

The ten ordered foam geometries studied, along with the **QR** foams, can be placed into three groups based upon their performance: there is a group with maximal performance, that in the low density limit, has a total stiffness that approaches the H-S bounds showing that the upper bounds are simultaneously achievable. There is a group with suboptimal but still stretch dominated properties where about one third of the material is stretched regardless of loading direction, and a third group comprising the remainder of the materials whose performance is less than this. As relative density increases there is a decrease in performance relative to these bounds for materials with maximum stiffness; although still achieving ~95% at $(\bar{\rho}/\rho_S) = 60\%$. The deviation in performance from the theoretical bounds in maximal performance designs is due to reduced strain energy densities in the material in edges and vertices whose relative volume fractions increase with increasing wall thickness. This may represent a fundamental limit in performance not captured by the H-S bound on bulk modulus, but this remains unproven.

The **DF** is an outlier, performing between the maximal and high performance groups. Its shear stiffness, $(\bar{G}/G_S)$, and total stiffness, $\Omega$, rise rapidly with $(\bar{\rho}/\rho_S)$ at low densities. The total stiffness is above the high performance group at low densities approaching the performance of the maximal group asymptotically, beginning to decrease with relative density when $(\bar{\rho}/\rho_S) \gtrsim 40\%$ (Figure 35). The high performance group has a total stiffness greater than the **DF** when $(\bar{\rho}/\rho_S) > 52\%$ indicating that the antisymmetric nature of the **DF** results in an extremely low energetic barrier to buckling, seen by the suppression of bending at similar relative densities in the high performance foams.

The **OF** was also identified by (Vigliotti and Pasini, 2012) to be extremely stiff, (and strong) being the stiffest of the materials they studied. They did however report that the properties did not vary much with orientation wherein our analysis found the **OF** to be the second most anisotropic. As they did not report a measure of isotropy no direct comparison has been done. The nearly uniform strain energy distributions in the **OF** (Figure 37, top-row) do suggest a high strength in agreement with their findings.

All of the highest-performance designs share the common feature in that they are all composed of continuous sheets of material. In aerospace applications cellular materials are required to have pores that allow for gas transport during atmospheric pressure changes. It may still be the case that adding porosity selectively, such as small circular holes in the center of faces for example, may not compromise the stiffness significantly. The influence of such porosity will be left for another study.

In previous literature the **OT** has be used as a prototypical stretch dominated lattice yet its performance compares unfavorably against stretch dominated foams in terms of axial and bulk stiffness and, as a result, total stiffness as well. The high shear stiffness of the **OT** results from the alignment of principal stress with the axis of truss members when under a macroscopic shear load. Truss members undergo pure axial stretching only when macroscopic principal stress are aligned with the longitudinal axis, while comparatively, sheets of material can support the range of macroscopic stresses that resolve into principal stresses that lie in its plane by pure stretching. Therefore, in the space of possible macroscopic loads the number of loads supported through stretching is far greater for materials composed of plate-like members than for those composed of truss- or rod-like members. Members must be connected in a manner where no mechanisms are present, that is, no bending of cell faces takes place without stretching of similar magnitude, such as in auxetic foams for example. In closed cell materials the bending of edges is associated with the stretching of faces so that even in loading scenarios where principal stresses do not favorably align with edges and faces, significant stretching still takes place. As a result, stretch-dominated closed cell foams far outperform stretch dominated lattices in terms of isotropic stiffness, and likely strength.

While the inherent bending dominated nature of truss structures explains the low axial stiffness of the **OT** it is unclear why the bulk modulus is low as it undergoes only affine straining, similar to the foams, yet has a bulk modulus that is only a small fraction of the HSUB (Figure 32). The magnitude of its normalized bulk modulus, $\bar{K}/K_S$, is comparable to that of $\bar{E}/E_S$ and $\bar{G}/G_S$, but axial and shear deformations involve significant bending while the hydrostatic deformations do not. The best explanation is that material in a closed cell foam is on average more constrained by neighboring material when compared to truss structures. Local principal strains then involve smaller lateral contractions or expansions from the Poisson effect, the net effect of which is a greater macroscopic stiffness. Because the dimensionality of the connectedness of truss members is lower that for plate-like members, and effective bulk stiffness depends on local hydrostatic constraint, it makes sense that the hydrostatic stiffness of all truss structures will be relatively low. For a similar reason the axial and shear stiffness of truss structures is expected to be inherently lower than for closed cell materials.

It is of note that the H-S bound on bulk, Young's and shear modulus achieve significantly different fractions of the Voigt bounds at the low density limit, achieving 38.3%, 52.6% and 50.0% respectively. This indicates that at the low density limit an ideal material that achieves these bounds simultaneously will have half of the material being stretched under an axial load, 52.6% of it stretched under a shear load and only 38.3% of it stretched under a hydrostatic load. This is because a cellular material with vanishingly thin walls will store no energy through bending when macroscopically deformed, therefore all the strain energy stored must be through stretching. Compare this to the properties of the isotropic solid constituent material that has properties $\bar{E} = \bar{G} = \bar{K} = 1$ and the isotropic (by Equation 73) **Q-R** foams that have $\bar{E} \approx \bar{G} \approx \bar{K} \approx C(\bar{\rho})$. It is reasonable to expect that all isotropic materials have this property yet clearly a material that achieves the H-S bounds, which were developed for "nearly" isotropic materials, does not have. And while $E_{HSU} \approx G_{HSU}$, $K_{HSU}$ is substantially smaller even though in designs that perform very near the HSUB no substantial bending occurs under hydrostatic compression. The bounds on Young's modulus are not rigorously derived yet a higher or lower value would be inconsistent with this analysis and results in this study, specifically Figure 35, right.

The effects of cell wall curvature have not been addressed as these structures have been qualified as "perfect" in this sense, possessing none. Cell wall curvature in ordered foams made through additive manufacturing will likely be minimal as the tolerances are small fractions of the resolution. It was shown in (Simone and Gibson, 1998) that the **BCC** foam suffers a 10% reduction in stiffness at $(\bar{\rho}/\rho_S) = 10\%$ when the midpoint deflection of a hexagonal wall is ~125% of the wall thickness. This effect decreases with increasing relative density and will unlikely be significant in designs produced through additive manufacturing.

Many current additive manufacturing techniques have difficulty generating closed cell topologies due to the enclosing of precursor material, in the case of bath sintering and solidification processes, or support structures, in filament processes, as cell topologies are generated. Combining a method of direct material placement, by sputtering of a slurry of precursor and binder or molten material, closely followed by sintering and densification, may allow for the inevitable realization of arbitrary closed cell materials. In aerospace applications where systems can undergo large pressure variations, venting of gasses must be accommodated by small ports in the cell walls of core materials, such as honeycombs, which can also be used to extract dissolvable support structures reducing significantly the barrier to production using some methods. The impact of porosity in cell walls will be left for a future study. Even with the relative infancy of  additive manufacturing at this time there is not a large barrier to producing these materials.

When the stiffness of these ordered foams, as calculated with FE, are compared with existing stochastic foams and stretch dominated lattices an improvement of more than one order of magnitude can theoretically be realized (Figure 41). The **OF+SC** foam is isotropic and has Young's modulus that nearly scales with $E/\rho$. When foams are composed of an aerospace grade aluminum alloy matrix composite, a currently utilized constituent material for aerospace structural honeycombs, and their stiffness is compared to the universe of available nearly isotropic materials (those that could theoretically serve as a constituent material for ordered foams and lattices) the **OF+SC** foam increases property space significantly in the direction of lightweight stiff materials (Figure 42). While additive manufacturing with Beryllium is not yet possible, and poses many significant challenges, the material properties of the **OF+SC** foam, composed of beryllium, potentially push the boundaries of property space very far in the direction of lightweight stiff materials. With such outstanding motivation and opportunity to create such high performance materials, and the myriad other applications additive manufacturing techniques will benefit, the production of ordered foams will undoubtedly be realized.

Additive manufacturing is not however the only way to produce these materials. Structures can be parsed into non-closed cell sections and then bonded together to form a closed structure. Molding, stamping, and traditional machining can then be used to produce geometries using almost any material that can be subsequently bonded. On larger scales, such as in the hull of a large marine vehicle, cells can be assembled by bonding together (though welding, brazing or with adhesives) components sizes on the order of cell faces. This can be combined with mechanical interlocking features, such as dovetail joints, to enhance structural integrity.

## 6. Conclusions

An RVE FE scheme employing 3D continuum elements was used to model closed cell materials of low to intermediate densities, producing reliable and consistent results that can be precisely placed in property space, finding results to match well with historical findings. This scheme is limited at low densities by mesh resolutions that scale with the cell wall thickness in closed cell geometries, making problems involving geometries with $(\bar{\rho}/\rho_S) \lesssim 7\%$ too large for this generalized study. The only limitation at higher relative densities is the creation of a periodic boundary mesh, which limited the resolution of the **QR** foams when $(\bar{\rho}/\rho_S) \gtrsim 50\%$, as this step was manual and inefficient in this context. In the case of more ordered geometries ensuring periodicity of the boundary mesh is more trivial.

A variety of topologies were investigated showing the possibility for materials to simultaneously achieve theoretical upper bounds for Young's, shear and bulk modulus, offering some novel materials with novel properties. Results agree well, in most cases, with cubic polynomial models indicating the stiffness of these hybrid materials comes from a complex combination of bending and stretching of material located in cell walls, edges and vertices. While the models developed by G-A (Gibson and Ashby, 2009) and (Grenestedt, 1999), through the application of Equations (78), (79) and (81), yield good predictions for the stiffness of foams based upon the partitioning of material by states of deformation and the associated strain energy density, FE models reveal large regions of unstressed material in some designs not contributing significantly to the stiffness and not accounted for by these approaches.

While the **OT** has been a prototypical hybrid material its performance compares poorly against closed cell materials that actually achieve an isotropic stiffness where ~1/3 of the material deforms through stretching. Lattice structures can serve as dual function materials, accommodating gas or fluid storage as well as being structural, however their stiffness, and likely strength, has a much lower potential than ordered closed cell foams. Truss structures primarily support loads through bending, even in the most ideal cases, and have poor local hydrostatic confinement driving their total stiffness performance far below closed cell materials. Hybrid open cell materials composed of plate like members, for example the **BFC** foam with the cubic cell walls removed, can outperform truss structures by $\gtrsim 20\%$ at $(\bar{\rho}/\rho_S)$ =12%, offering mostly increase bulk stiffness (this was excluded from this paper for brevity); such structures are worthy of further investigation.

Some of the geometries presented offer unique and interesting properties. The antisymmetric nature of the **DF** and the associated preferential buckling mechanism, that is independent of cell wall curvature, has the potential to offer a very consistent yielding and post yield behavior, making it a good candidate as an energy absorbing material. The **BFC** foam is nearly isotropic and stretch dominated giving it the properties of theoretical stretch dominated lattices and stretch dominated quasi-random foams. The simple geometry relative to stochastic materials and hierarchical nature make the **BFC** foam an interesting candidate for further study. The **OF+SC** foam offers maximum isotropic stiffness making it an ideal hybrid material. As the core material in a sandwich panel it would surpass the performance of metal foams and theoretical stretch dominated lattices by more than a factor of ten in some cases. If design requirements favor an anisotropic material the relative cell wall thickness can be scaled between the **OF** and **SC** substructures, modifying the degree of isotropy over a wide range without compromising total stiffness. Unlike designs produced through topology optimization, which do not surpass the performance of ordered foams, these ordered foams are scalable in relative density without affecting their properties substantially. Large stress concentrations are associated with edges and vertices can be mitigated by increasing the radius of curvature of corners and edges through manual manipulation of models or by using an ordered foam geometry as the seed for a topology optimization scheme.

The three main groups of materials identified are diverse in topology yet are grouped by nearly identical total stiffness, characterized by their reliance on bending to support macroscopic loads (Figure 35). Materials exhibit a wide range of isotropies as a function of cell geometry yet the total resistance to deformation is determined by the relationship between neighboring cells and not the cell shape. In the case of strength and post yielding behavior the cell shape will play a strong role. All that remains to be done to fabricate and test these materials is the selection of a suitable direct fabrication method, as the CAD models used are directly amenable to additive manufacturing. There are currently many commercial solutions that have individual limitations that pose challenges in the creation of some geometries that still need to be overcome. As direct manufacturing becomes more common place in specialty and commercial manufacturing, ordered foam geometries will undoubtedly find many engineering applications. In a coming study the strength will be investigated, including the large strain behavior.

## Acknowledgements

We acknowledge support from the Center for Scientific Computing at the CNSI and MRL: an NSF MRSEC (DMR-1121053) and NSF CNS-0960316.

## References

ABAQUS, 2013.

Ashby, M., 2011. Hybrid Materials to Expand the Boundaries of Material-Property Space. J. Am. Ceram. Soc. 94, s3–s14.

Danielsson, M., Parks, D.M., Boyce, M.C., 2002. Three-dimensional micromechanical modeling of voided polymeric materials. J. Mech. Phys. Solids 50, 351–379.

Daxner, T., n.d. Finite Element Modeling of Cellular Materials.

Daxner, T., Bitsche, R.D., Böhm, H.J., 2006. Space-Filling Polyhedra as Mechanical Models for Solidified Dry Foams. Mater. Trans. 47, 2213–2218.

De Giorgi, M., Carofalo, A., Dattoma, V., Nobile, R., Palano, F., 2010. Aluminium foams structural modelling. Comput. Struct. 88, 25–35.

Demiray, S., Becker, W., Hohe, Jö., 2005. Strain-energy based homogenisation of two- and three-dimensional hyperelastic solid foams. J. Mater. Sci. 40, 5839–5844.

Deshpande, V.S., Fleck, N.A., Ashby, M.F., 2001. Effective properties of the octet-truss lattice material 49, 1747–1769.

Fahlbusch, N., Becker, W., 2011. EffectiveMechanical Properties of Closed-Cell Foams Investigated with aMicrostructural Model and Numerical Homogenisation, in: Altenbach, H., Eremeyev, V.A. (Eds.), Shell Like Structures. Springer Berlin Heidelberg, Berlin, Heidelberg, pp. 549–560.

Fischer, F., Lim, G.T., Handge, U. a., Altstadt, V., 2009. Numerical Simulation of Mechanical Properties of Cellular Materials Using Computed Tomography Analysis. J. Cell. Plast. 45, 441–460.

Fleck, N. a., Deshpande, V.S., Ashby, M.F., 2010. Micro-architectured materials: past, present and future. Proc. R. Soc. A Math. Phys. Eng. Sci. 466, 2495–2516.

Gibson, L.J., Ashby, M.F., 2009. Cellular Solids: Structure and Properties. 1997.

Gibson, L.J., Ashby, M.F., Harley, B.A., 2010. Cellular materials in nature and medicine. Cambridge University Press.

Grenestedt, J.L., 1999. Effective elastic behavior of some models for “perfect” cellular solids. Int. J. Solids Struct. 36, 1471–1501.

Grenestedt, J.L., Bassinet, F., 2000. Influence of cell wall thickness variations on elastic stiffness of closed-cell cellular solids 42, 1327–1338.

Hashin, Z., Shtrikman, S., 1963. A VARIATIONAL APPROACH TO THE THEORY OF THE ELASTIC BEHAVIOUR OF MULTIPHASE MATERIALS * 11.

Jang, W.-Y., Kyriakides, S., 2009a. On the crushing of aluminum open-cell foams: Part II analysis. Int. J. Solids Struct. 46, 635–650.

Jang, W.-Y., Kyriakides, S., 2009b. On the crushing of aluminum open-cell foams: Part I. Experiments. Int. J. Solids Struct. 46, 617–634.

Matlab, 2013.

Radman, a., Huang, X., Xie, Y.M., 2012. Topological optimization for the design of microstructures of isotropic cellular materials. Eng. Optim. 1–18.

Roberts, a. P., Garboczi, E.J., 2001. Elastic moduli of model random three-dimensional closed-cell cellular solids. Acta Mater. 49, 189–197.

Sigmund, O., 2000. A new class of extremal composites. J. Mech. Phys. Solids 48, 397–428.

Simone, a. E., Gibson, L.J., 1998. The effects of cell face curvature and corrugations on the stiffness and strength of metallic foams. Acta Mater. 46, 3929–3935.

Solidworks, 2012.

Thomson, S.W., 1888. On the Division of Space with Minimum Partitional Area. Acta Math. 11, 121–134.

Torquato, S., Stillinger, F.H., 2010. Jammed hard-particle packings: From Kepler to Bernal and beyond. Rev. Mod. Phys. 82, 2633–2672.

Valdevit, L., Jacobsen, A.J., Greer, J.R., Carter, W.B., 2011. Protocols for the Optimal Design of Multi-Functional Cellular Structures: From Hypersonics to Micro-Architected Materials. J. Am. Ceram. Soc. 94, s15–s34.

Vigliotti, A., Pasini, D., 2012. Stiffness and strength of tridimensional periodic lattices. Comput. Methods Appl. Mech. Eng. 229-232, 27–43.

Wadley, H.N.G., 2006. Multifunctional periodic cellular metals. Philos. Trans. A. Math. Phys. Eng. Sci. 364, 31–68.

## Chapter II Figures

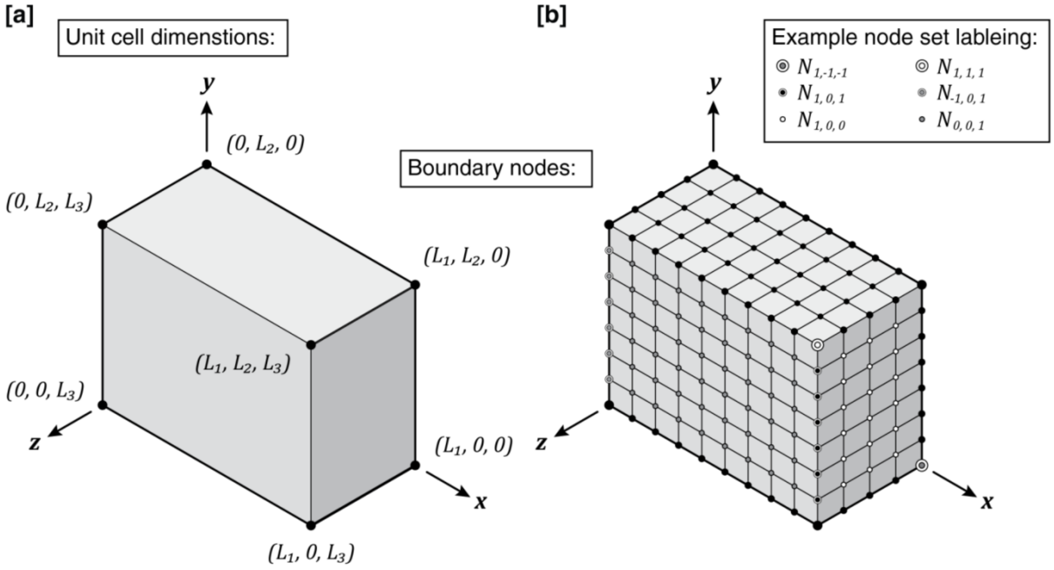

**Figure 19 - Representative volume element with dimensions (left) and example boundary mesh illustrating node set labeling convention (right). All the results in this paper pertain to models with $L_1 = L_2 = L_3 = 1$.**

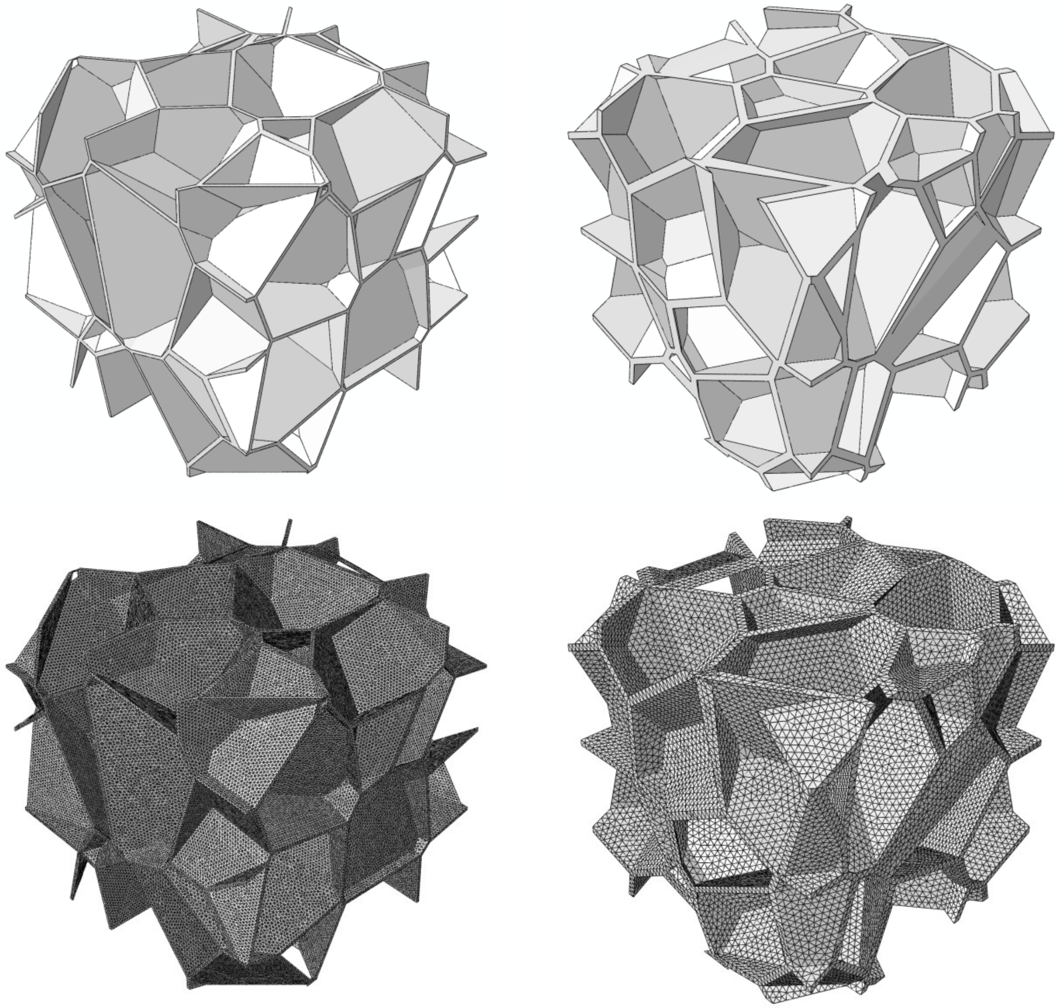

**Figure 20 - RVE of quasi-random foams and their associated meshes (RF20-1%-1, left & RF20-2%-2, right). The structures have wall thicknesses, $t/l = 1\%$ (left) and $t/l = 2\%$ (right). The foam on the right has 143,542 10-noded tetrahedral elements with a total of 263,581 nodes while the model on the left has 650,007 elements and 1,206,305 nodes.**

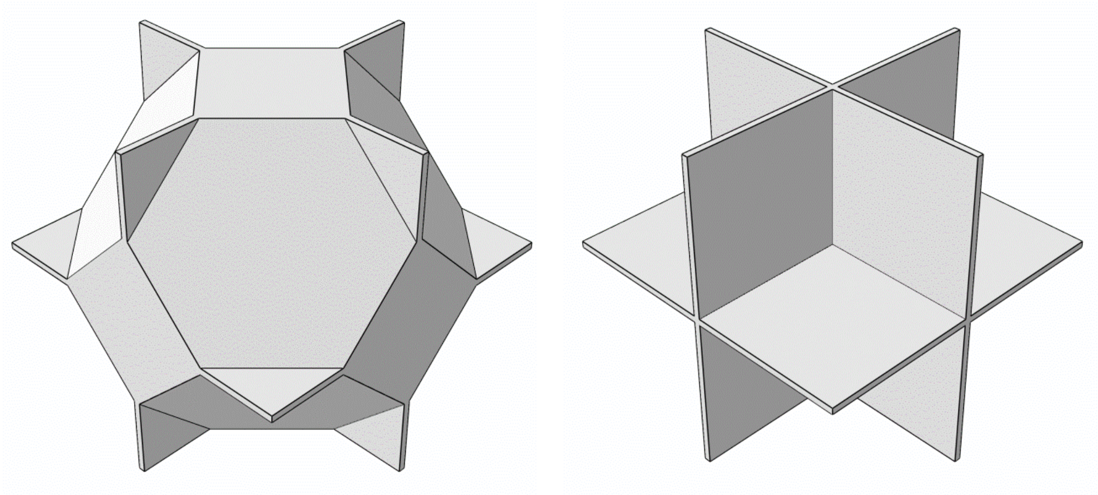

**Figure 21 - RVEs of foams made from the BCC seeding pattern with t/*L*=2% wall thickness (left) and simple cubic (SC) foam with t/*L*=2%.**

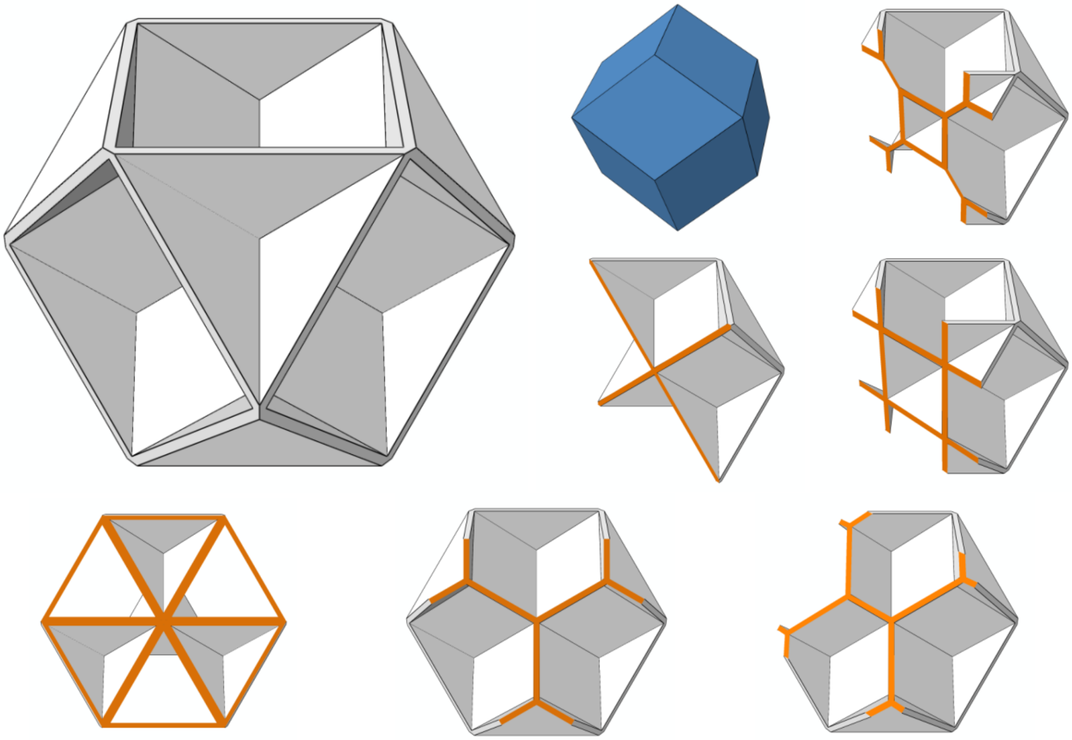

**Figure 22 - Face centered cubic (FCC) unit-cell (top-left) and the reciprocal polyhedron (top-center), a rhombic dodecahedron. It has been called a 3-D honeycomb due to its cross section in the {1-1-0} directions being hexagonal (bottom-right) and some cross-sections in the {1-1-1} as well (bottom-center). Slices in the {1-0-0} directions reveal orthogonal members spaced at intervals of *L*/4 oriented at 45 degrees relative to each other (middle-center and –right). As one steps through the material the cross-sections can be seen to morph between one another (top-right). Likewise the {1-1-1} cross-sections morph between triangulated sections (bottom-left) and hexagonal ones (bottom-center).**

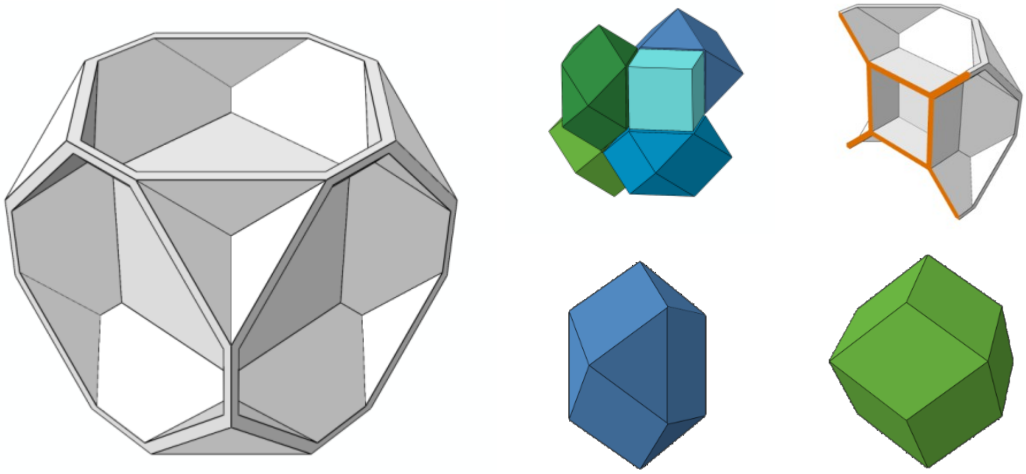

**Figure 23 – The BFC foam (left) is based upon an FCC seeding pattern with an added body centered seed. The result is a central cubic cell (light blue) and 6 other dodecahedra that have 2 square, 8 triangular and 4 rhomboid faces (dark green and dark blue) and rhombohedral dodecahedra lying at the corners of the unit cell (light green, bottom-right).**

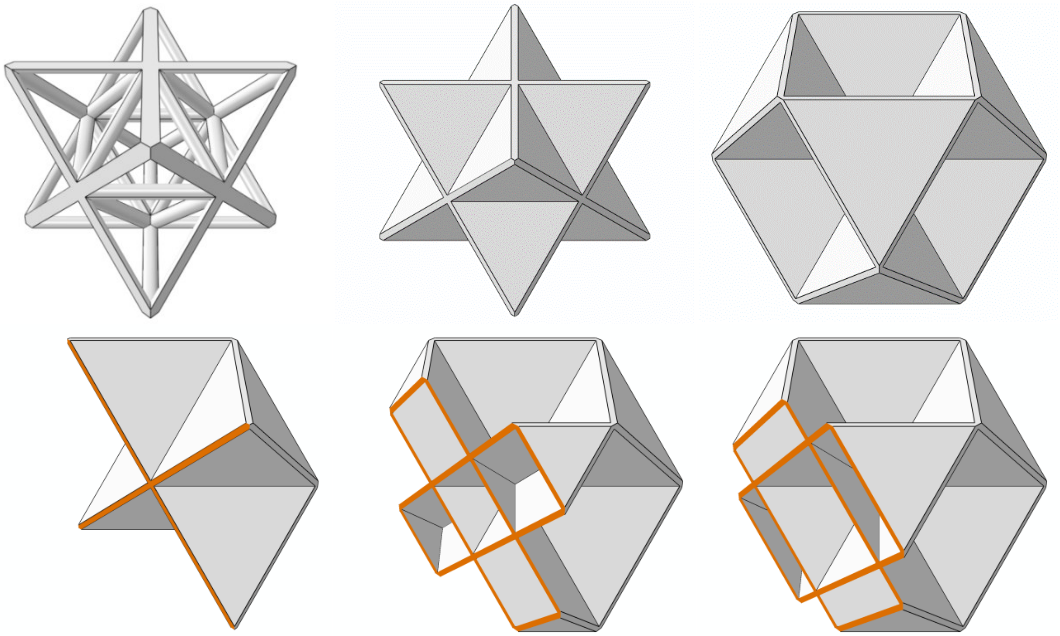

**Figure 24 - Octet-truss (top-left) and two different unit cells of the octet-foam (top-center and -right). Cross-sections of the octet-truss foam are composed of orthogonal members in the {1-0-0} directions (bottom row). Cuts in the {1-1-1} directions (not pictured) are triangulated.**

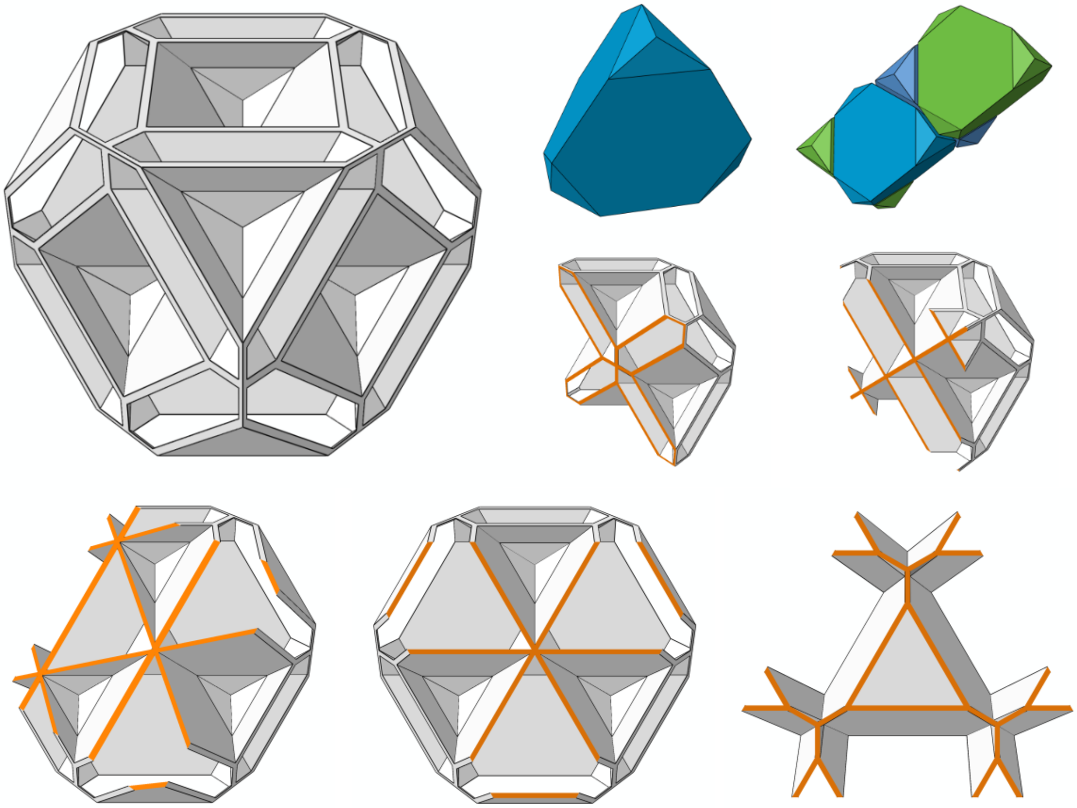

**Figure 25 – Unit cell of foam based upon a diamond crystal structure (top-left). The reciprocal polyhedron is a truncated tetrahedron (top-center). Cells are arranged so that the nearly hexagonal faces of adjacent cells are rotated relative to each other by 60 degrees so that cells stack in an alternating fashion (top-right). Select cross-sections in the {1-1-0} (bottom-left) and {1-1-1} directions (bottom-center and -right) are triangulated. Cross-sections in the {1-0-0} direction at *L*/4 and 3*L*/4 are rectangular (middle-right); the short and long axis of the rectangles alternates with intervals of *L*/2.**

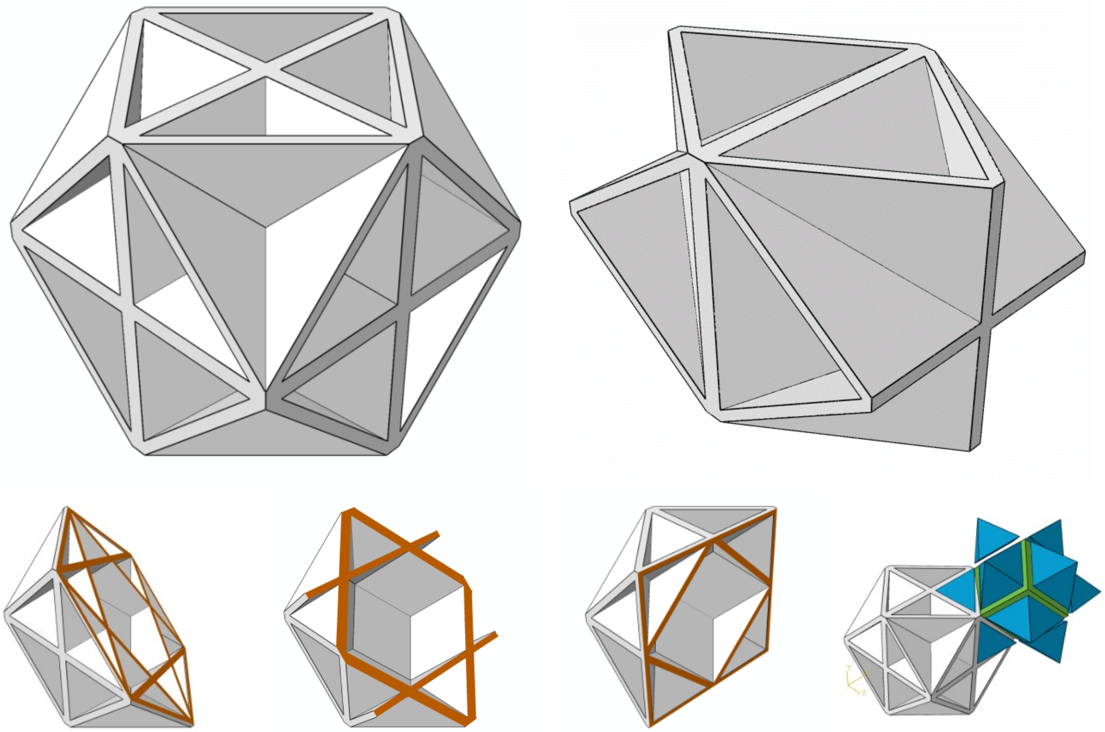

**Figure 26 – Unit cell of dodecahedral-pyramidal foam (DDPF) (top-left) is cousin to the Octet-Foam (OF) (alternate unit cell pictured top-right). The OF consists of two orthogonal interpenetrating prismatic rhobohedral elements while the DDPF consists of three orthogonal interpenetrating square prismatic elements. The reciprocal unit cells of the DDPF (bottom-right)are a dodecahedron (green) that share faces with 12 pyramidal cells (blue). Cross-sections in the {1-1-1}, {1-1-0} and {1-1-1} directions are shown along the bottom (left to right respectively). Dodecahedral cells are arranged in BCC fashion sitting at the corners and center of the unit cell.**

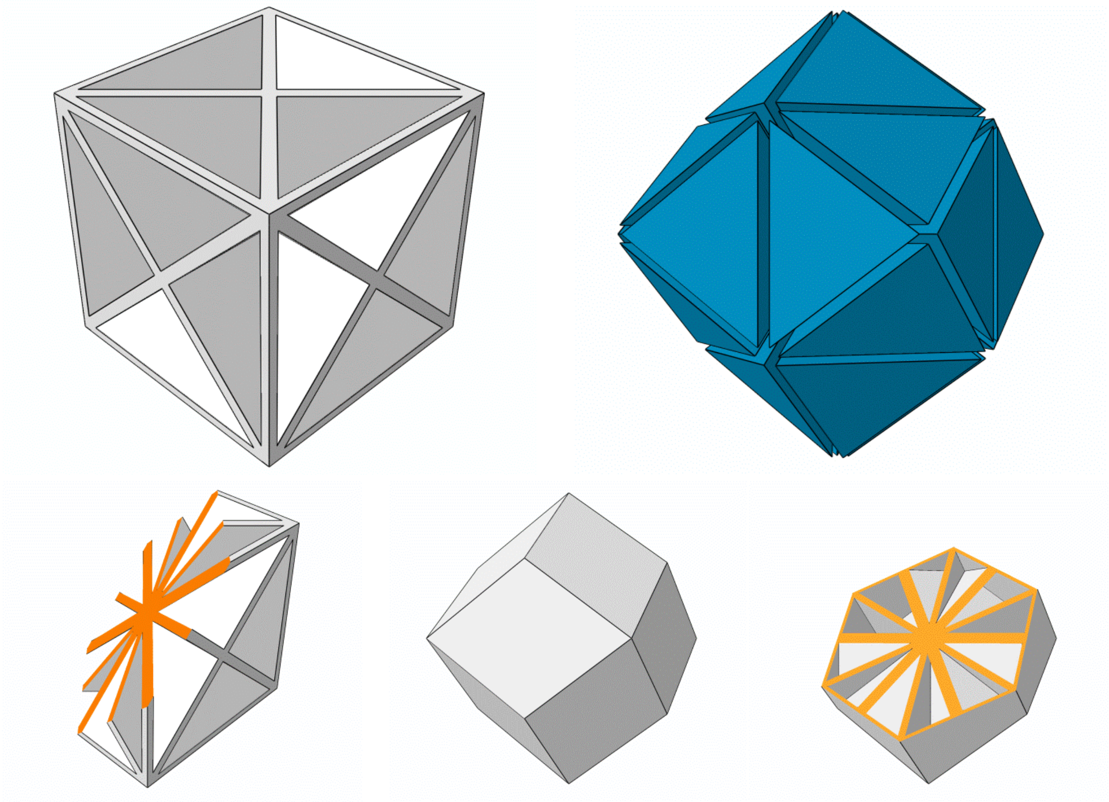

**Figure 27 - X-Foam: Unit cell (top-left), packing of reciprocal polyhedrons (top-right) (12 tetrahedral cells pack to form a dodecahedral shape), {1-1-1} slice through unit cell (bottom-left), alternate unit cell that fills space with FCC packing (bottom-center) and slice of alternate unit cell (bottom-right).**

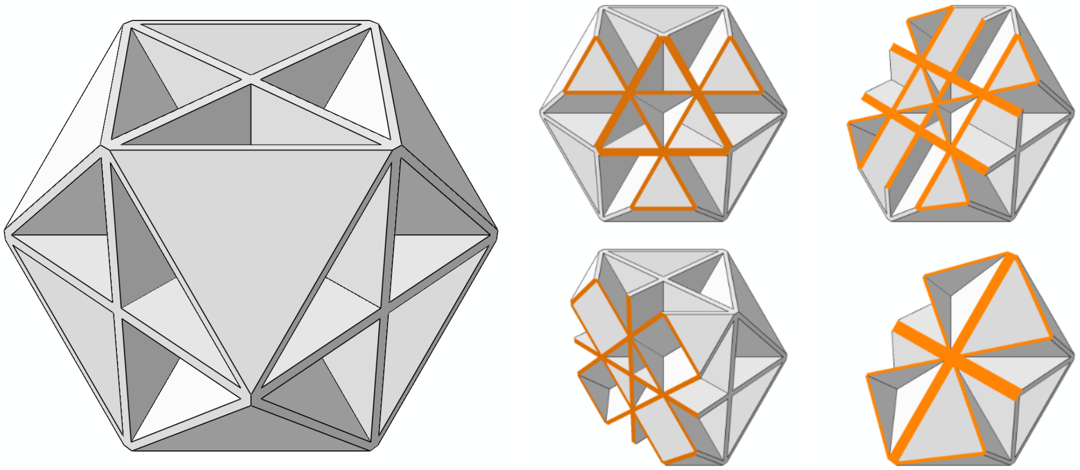

**Figure 28 - OF+SC foam unit cell (left) is formed from the superposition of the Octet-foam (OF) and the simple cubic (SC) foam. Cross-sections (right) show fairly uniform material alignment.**

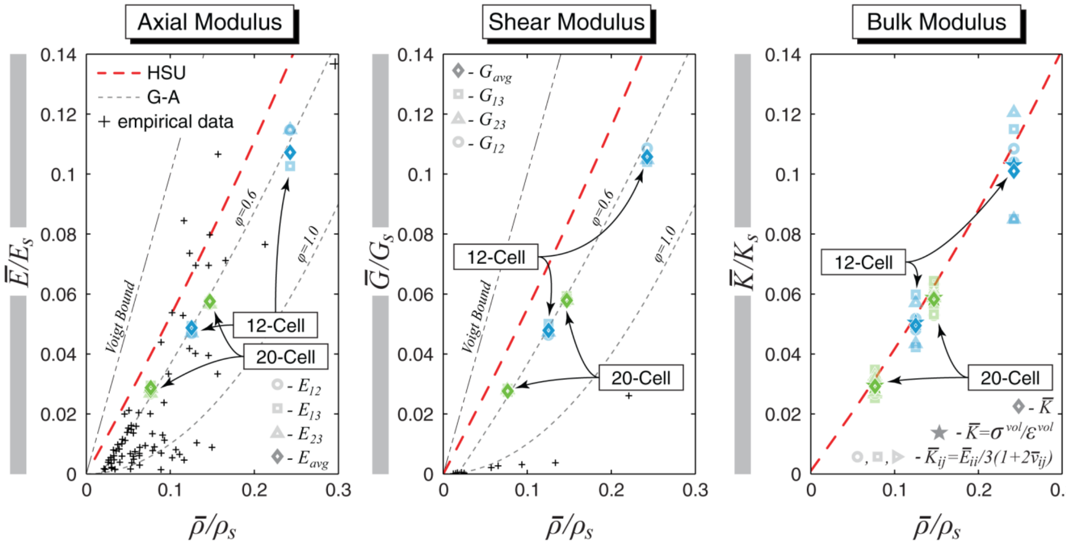

+ - *(Gibson and Ashby, 2009) - empirical data for closed cell foams*

**Figure 29 - Axial, shear and hydrostatic stiffness of Quasi-Random (QR) foams normalized by the properties of the bulk material. The Hashin-Shtrikman upper bounds (HSU) are plotted in heavy dashed lines, along with contours of Equations (78) and (79) for different values of ϕ (left and center). The axial stiffness of the QR foams is consistent with empirical data taken from (Gibson et al., 2010) and from the curve fit used for stiff foams (ϕ=0.6). Anisotropy was minimal in models with 20 cells and only significant in the model with 12 cells at the highest relative density ($\bar{\rho} = 24\%$). The normalized shear moduli are nearly identical in value to the axial moduli making these structures nearly isotropic by equation (73). The limited empirical data available for the shear stiffness is inconsistent with analysis and FE results for foams which both predict higher stiffnesses (center). The average bulk modulus (diamonds), calculated from the 6 values obtained from the axial calculations (circles, boxes and triangles), only differ appreciably from the values obtained from direct calculations (stars) in the 12 cell model at the highest relative density.**

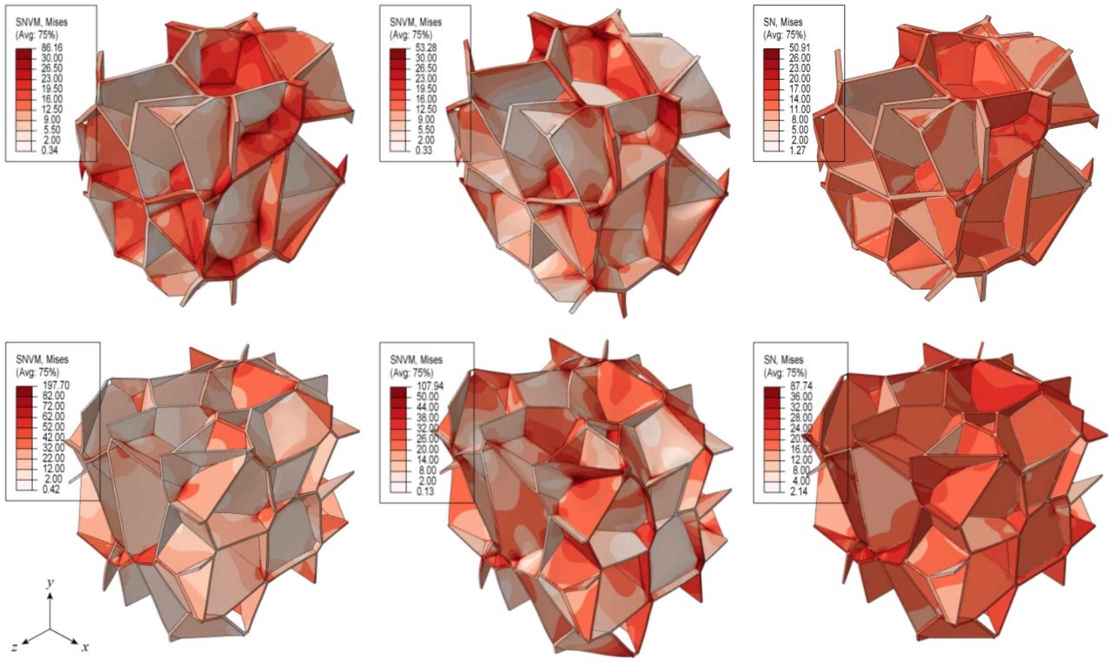

**Figure 30 - Stress distributions in foams with 12 cells and $t/L = 2\%$ (top) and 20 cells and 1% wall thickness (bottom) subjected to uniaxial compressive stress in the x-direction (left), a macroscopic shear stress $\tau_{xy}$ (center) and a compressive hydrostatic stress (right). Local stresses are normalized by the macroscopic Von Mises stress in the axail and shear case and the applied stress in the hydrostatic case.**

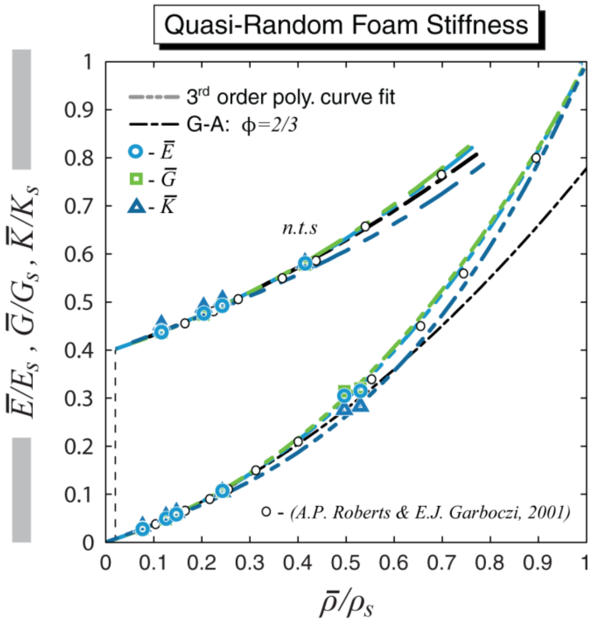

**Figure 31 - Normalized axial, shear and bulk moduli for quasi-random foams. Curve fits for $(\bar{E}/E_S)$ and $(\bar{G}/G_S)$ for $(\bar{\rho}/\rho_S) \lesssim 25\%$ are nearly identical to Equation (78) and (79) with $\phi = 2/3$. At higher relative densities a cubic term is necessary to describe the behavior. FE data from (Roberts and Garboczi, 2001) for similar quasi-random foams are in excellent agreement. FE mesh quality was poorer above $(\bar{\rho}/\rho_S) \approx 0.5$ due to limitations in the meshing algorithm, artificially stiffening results only slightly.**

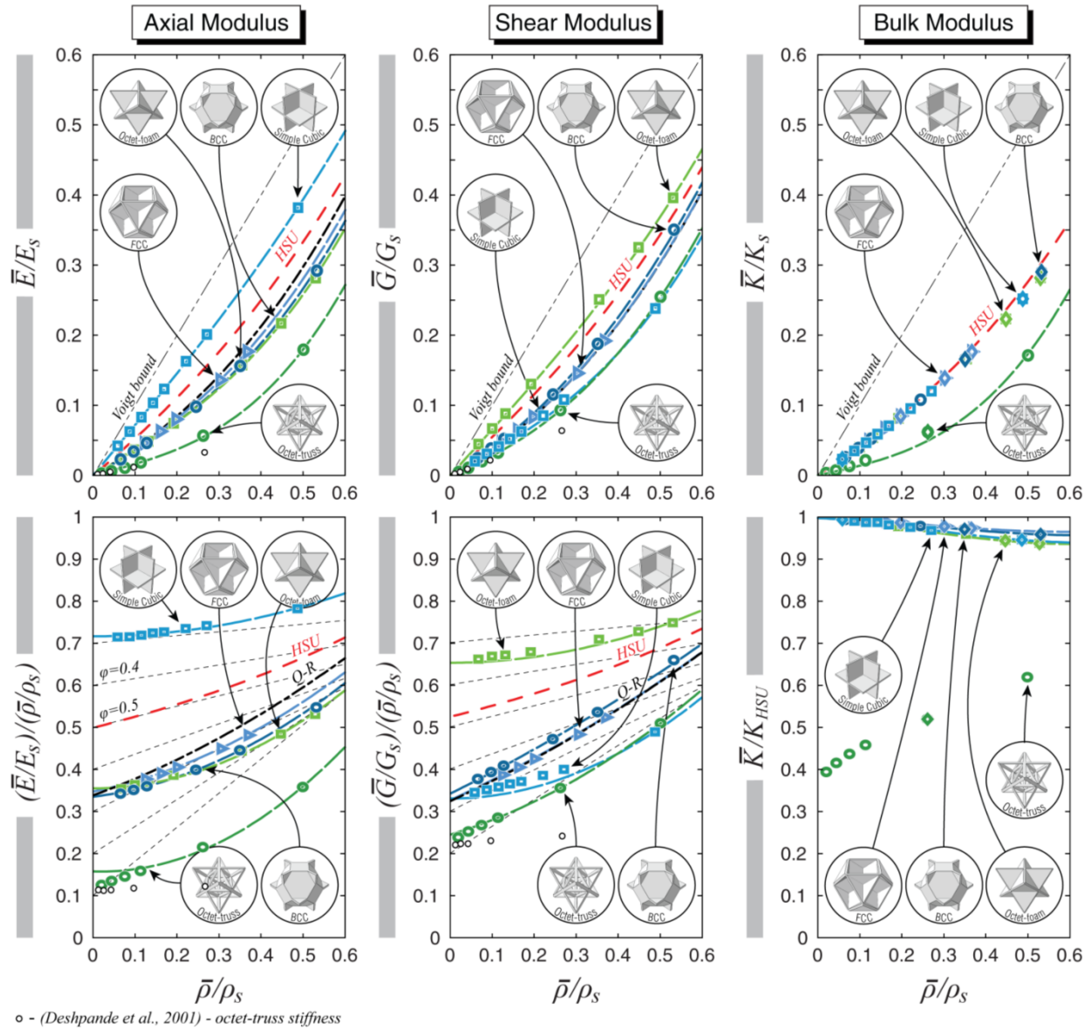

**Figure 32 - Normalized effective axial, shear and bulk moduli (left, center and right respectively). Effective moduli are normalized by the moduli of the bulk material (top), and by the moduli of the bulk material and the Voigt bound (bottom) for the cases of $\bar{E}$ and $\bar{G}$, and by the Hashin-Shtrickman (H-S) upper bound for the case of bulk modulus. Contours of Equation (78) and (79) are shown (bottom-left and –center) where the linear stretching coefficient, $(1-\phi)$, are the $y$-intercepts. The axial and shear stiffness of the QR foams are plotted for comparison (left and center). All these materials have cubic symmetry so only one axial and shear modulus is reported. In the case of bulk modulus the results for direct calculations are shown with a diamond; they agree with the remaining calculations done using the axial modulus, the effective Poisson ratio, $\bar{\nu}_{ij}$, and the assumption of isotropy. While the H-S bound on bulk modulus is rigorous (right) the bounds on Young's and shear moduli are not due to the high degree of anisotropy of some designs.**

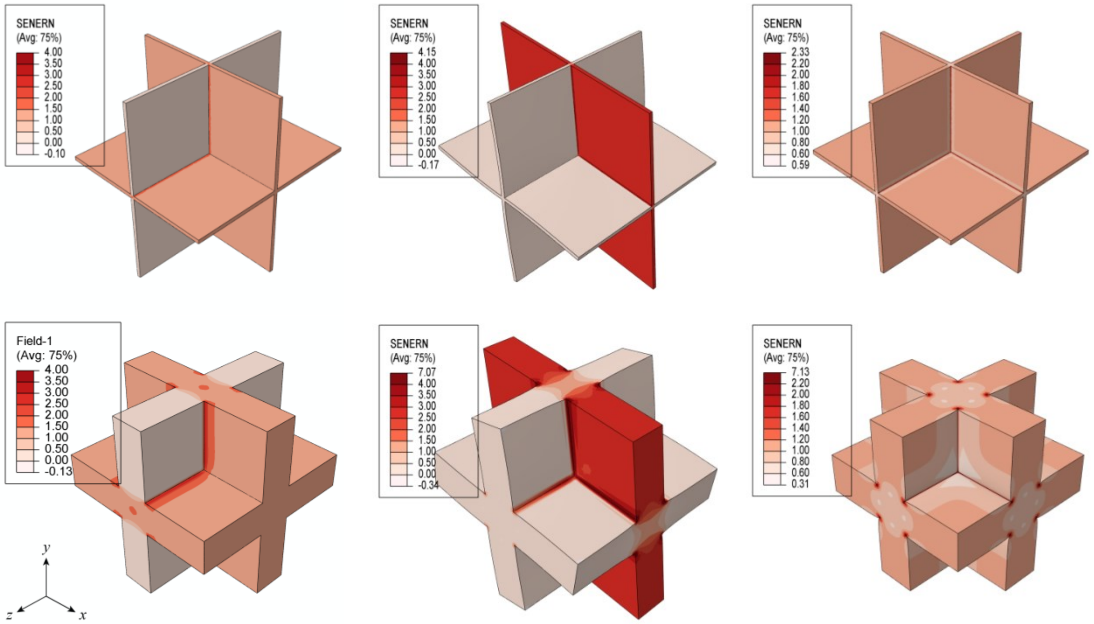

**Figure 33 - Normalized strain energy distributions in SC foams with wall thickness $t/L = 2\%$ and $t/L = 20\%$ (top and bottom respectively) under macroscopic axial compressive stress (left), shear (center) and hydrostatic compression (right). In all cases $\epsilon = 0.1\%$ which have been magnified 100X. Local strain energy densities are normalized by the average local strain energy density. Low density foams have large regions of uniform strain energy compared with higher density foams. Material in edges and vertices in walls under high stress is confined by neighboring material in the intersecting walls at lower stress. As wall thickness increases with relative density a degradation in performance is seen in all designs relative to the Hashin-Shtrikman upper bound on bulk modulus** (Hashin and Shtrikman, 1963) **due to this constrained material. Under shear loading two of three walls are relatively unstrained increasing the magnitude of this effect. (Negative strain energy levels indicated in legends are fictitious and do not actually occur in models.)**

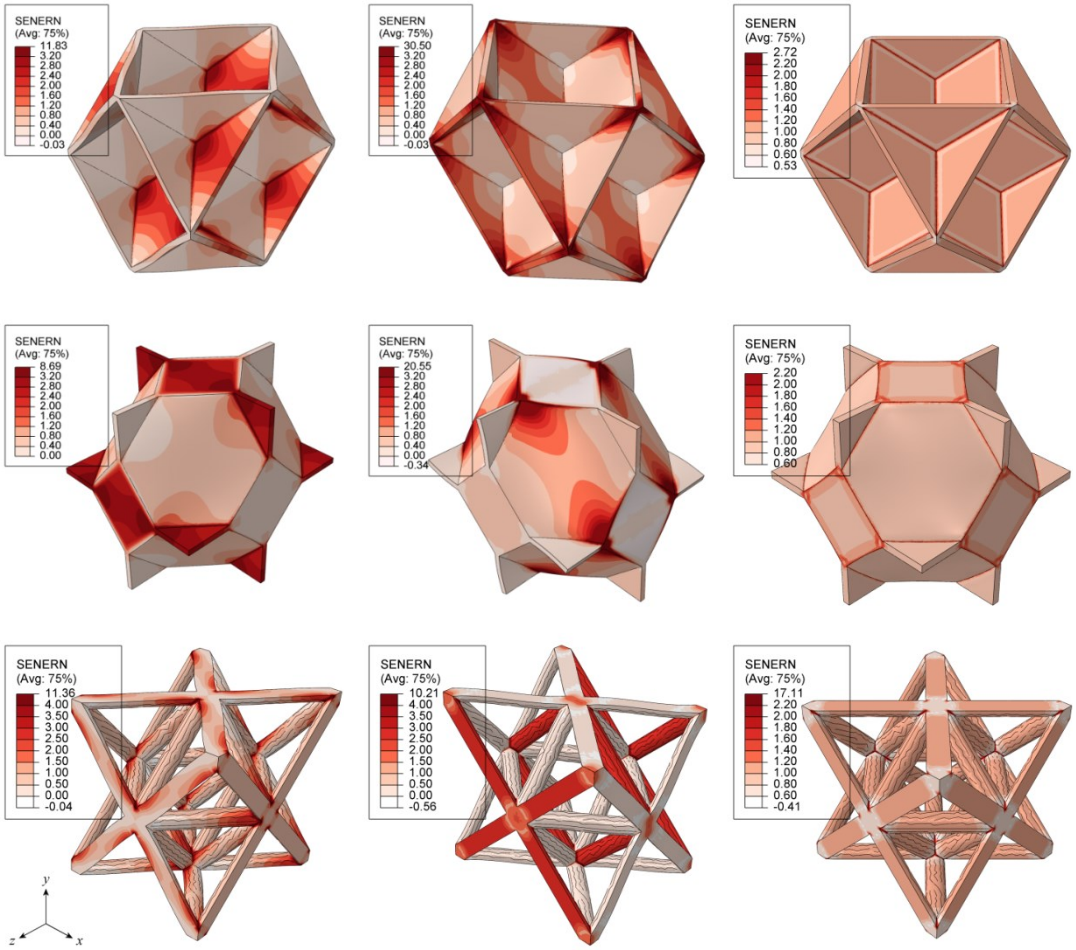

**Figure 34 - Normalized strain energy distributions in FCC and BCC foams (top and middle) and Octet-truss (OT) (bottom) under axial, shear and hydrostatic loading (left, center and right). Strain energy contours of greatest interest and influence are plotted at the sacrifice of fidelity near strain energy concentrations; the magnitude of strain energy concentrations are of course mesh dependent and do not contribute substantially to the total strain energy. Under axial load strain energy is clearly concentrated in cell walls aligned with the applied stress (top- and middle-left) which form stiff chains of material. Strain energy is more clearly partitioned by the local mode of deformation in the BCC foam whose square cell walls can store almost no strain energy depending on their orientation in both axial and shear case. The high shear stiffness of the OT results from the alignment of principle stresses with the longitudinal axis of truss members where strain energy is stored through stretching (bottom-center); under axial loading the OT undergoes mostly bending (bottom-left). (Negative strain energy levels indicated in legends are fictitious and do not actually occur in models.)**

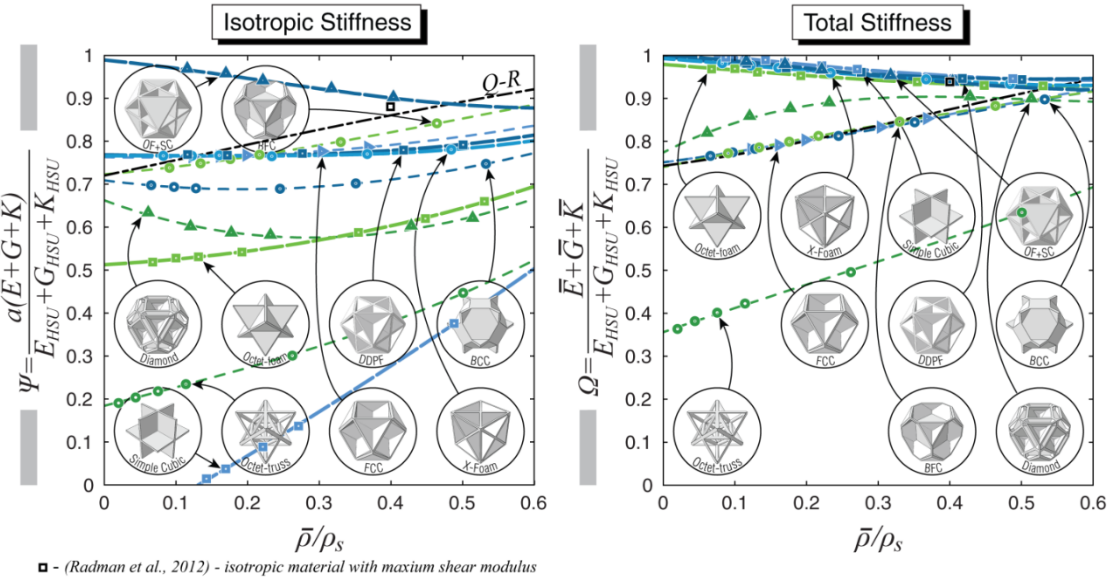

**Figure 35 - Overall stiffness performance of ten ordered from geometries. The total stiffness (right) segregates the designs into three groups: a group with maximal performance whose total stiffness approaches the sum of the H-S bounds, Ω → 1 as $(\bar{\rho}/\rho_S) \to 0$ (heavy dashed lines), another group whose properties are close to that of the idealized stretch dominated material, having stiffness ~1/3 of the Voigt bound, that have $\Omega \approx 75\%$ as $(\bar{\rho}/\rho_S) \to 0$, and a third, only including the OT, whose performance is less than the others. On the right the total stiffness is multiplied by the isotropy, *a*, as a measure of isotropic stiffness where an ideal isotropic material has $= \Psi = 1$ . A structure produced from topology optimization by (Radman et al., 2012) to be isotropic and have maximum shear modulus has a total stiffness nearly identical to the OF+SC foam; it is slightly more anisotropic by equation (73) and therefor has lower Ψ (left). The scaling factor, *a*, is somewhat arbitrary in magnitude as the objective function is unbounded on one side. The OF+SC foam is found to have a stiffness, $\Omega \to 1$, as $(\bar{\rho}/\rho_S) \to 0$ and is nearly isotropic making it the only material with $\Psi \to \Psi_{HSU}$, as $\bar{\rho} \to 0$, giving it ideal properties far in excess of theoretical stretch dominated lattices. Materials with maximum stiffness are plotted with thick lines.**

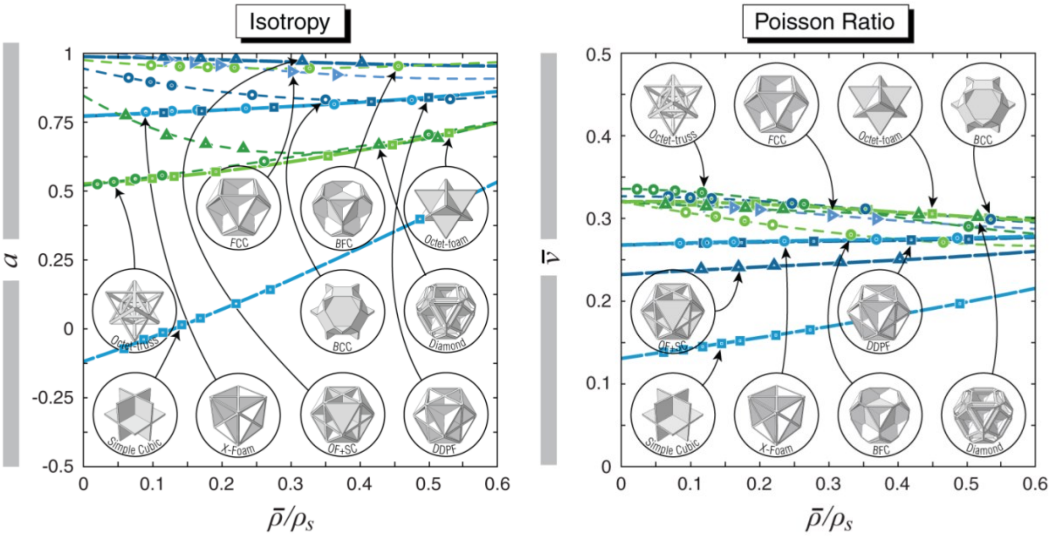

**Figure 36 - Isotropy and effective Poisson ratios as a function of relative density for all geometries with the exception of the QR foams, which are effectively isotropic and have $\bar{\nu} \approx 0.30$. Materials with maximal stiffness are plotted with heavier lines.**

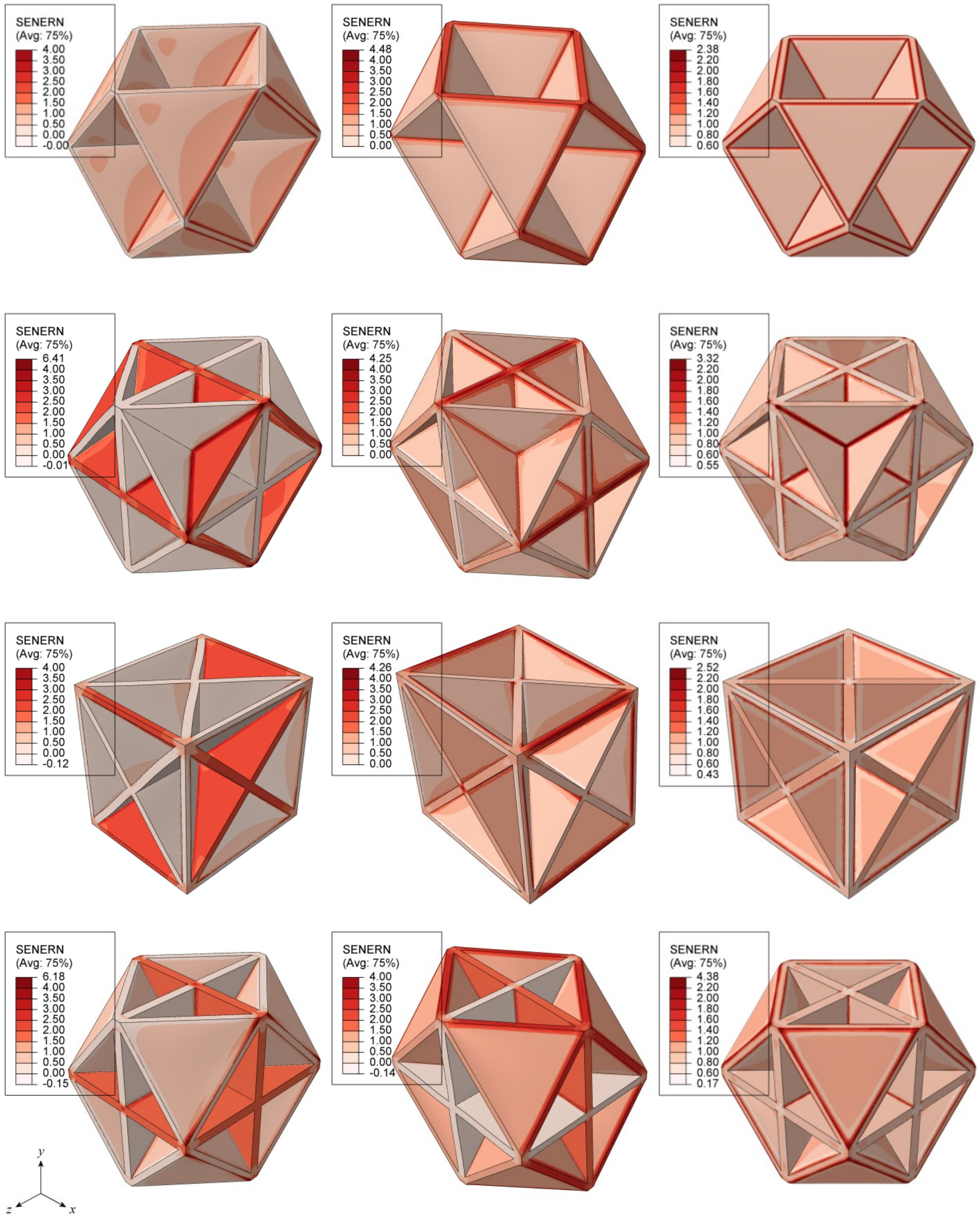

**Figure 37 - Normalized strain energy distributions under axial, shear and hydrostatic loading (left, center, and right respectively) at a macroscopic strain of $\epsilon$=0.1% in the Octet-Foam (OF) (top), dodecahedral-pyramidal foam (DDPF) (2nd row), X-Foam (XF) (third-row) and Octet+'Simple Cubic' (OF+SC) foam (bottom). All strains are scaled 100X for clarity. Because the relative orientation of cell walls in the OF, being composed of regular tetrahedraons, the strain energy distributions in each wall are identical in the both axail and shear cases (top-left and –middle); in the shear case all walls are placed in a state of nearly pure compression or**

**tension suggesting its shear stiffness is maximal, at least in the low density limit. (Negative strain energy levels indicated in legends are fictitious and do not actually occur in models.)**

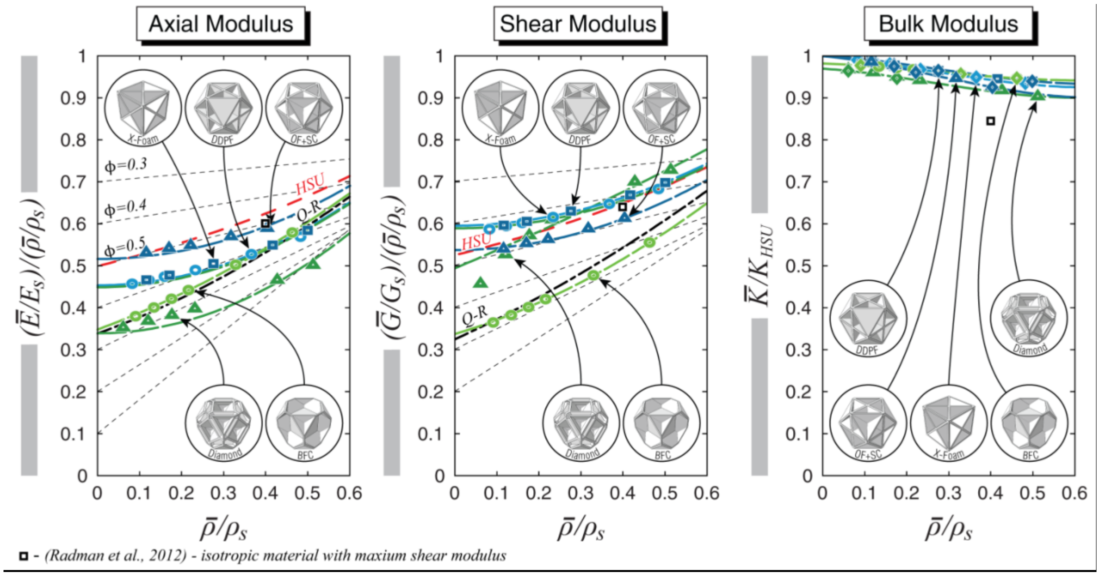

**Figure 38 - Stiffness of X-Foam, Diamond (DF), dodecahedral pyramidal foam (DDPF) and Body+Face Centered (BFC) foams. The OF+SC foam has stiffness that is in excess of 99.9% of the H-S bound on Young's modulus, 97.1% the bound on shear and 98.3% of the bound on bulk modulus, at the lowest density analyzed. The H-S bounds on Young's and shear modulus do not limit the performance of some materials due to their anisotropy. The BFC foam is nearly isotropic with stiffness similar to the QR foams. The OF+SC, DDPF and XF all have bulk moduli that converge on the H-S bound at the low density limit (right). Topology optimization for an isotropic material with maximum shear modulus resulted in a design with similar performance to the OF+SC foam (black-square).**

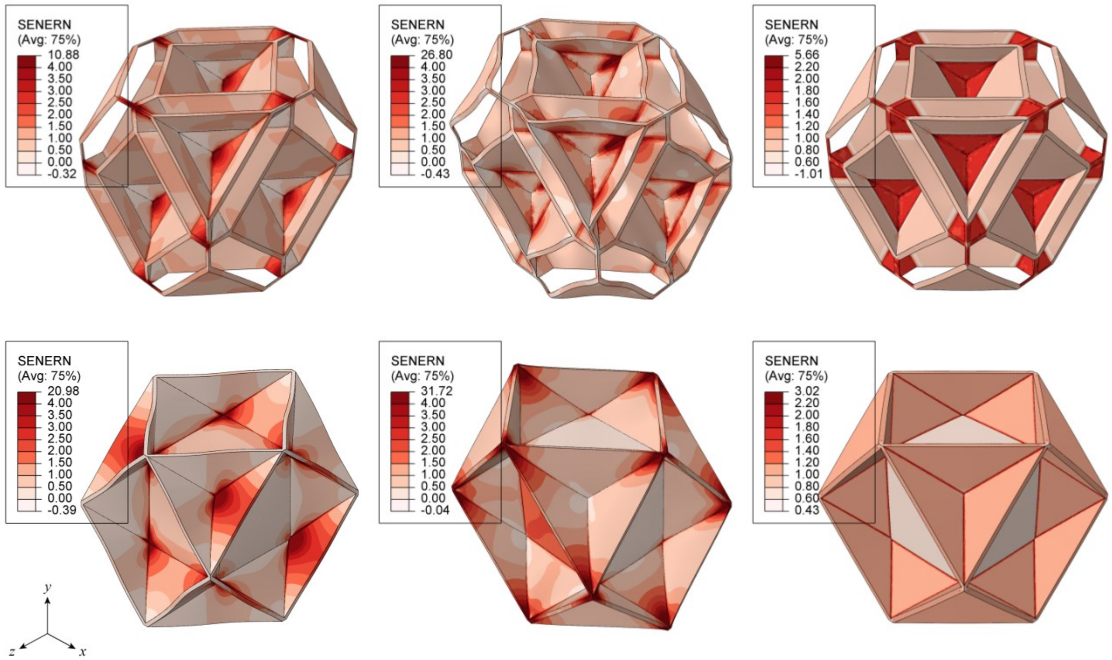

**Figure 39 - Normalized strain energy distributions in the diamond foam (DF) (top) and the Body+Face Centered (BFC) (bottom), both with $t/L = 2\%$, at macroscopic strains of $\epsilon = 0.1\%$. Under axial loading cell walls aligned with the applied stress experience the highest strain energy density (left). Shear loading in the DF results in complementary buckling of neighboring antisymmetrically aligned cells at strains as low $\epsilon = 0.001\%$, when no initial cell wall curvature is present. The sub-maximal bulk stiffness of the DF and BFC foams is evident in the non-uniformity of the strain energy distributions between cell walls under hydrostatic loading (right). Contours of strain energy density around the average are plotted at the expense of fidelity near strain energy concentrations, the magnitude of which are mesh dependent and do not contribute substantially to the total strain energy. (Negative strain energy levels indicated in legends are fictitious and do not actually occur in models.)**

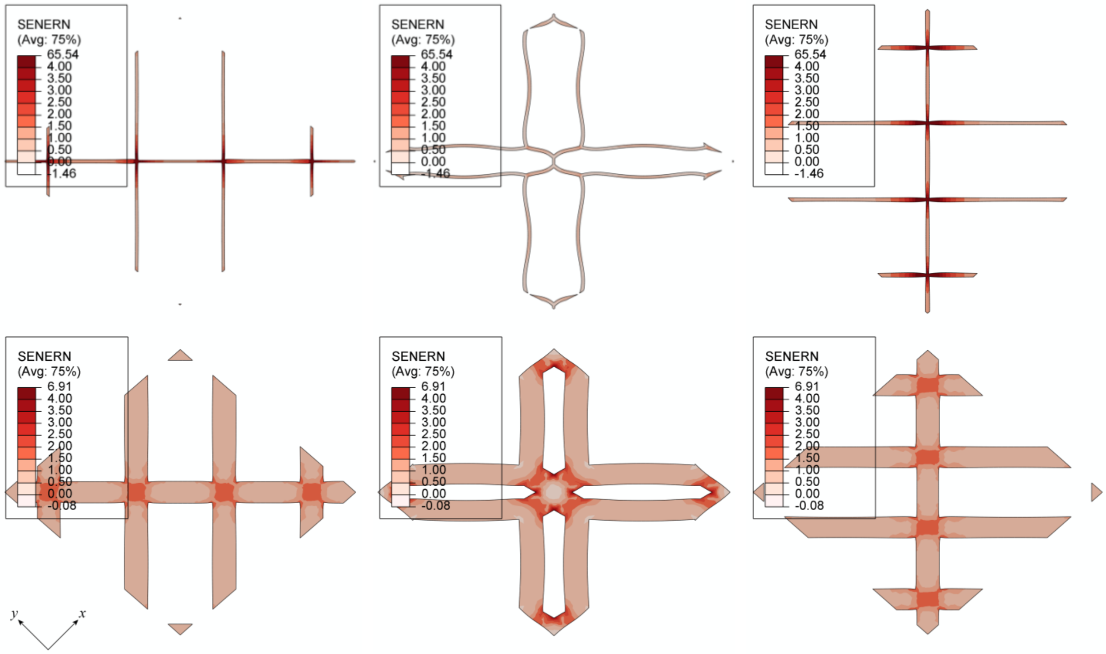

**Figure 40 - Strain energy distributions in cross-sections of DF with $t/L = 1\%$ (top) and $t/L = 8\%$ (bottom) from macroscopic shear loading; macroscopic strains of $\epsilon = 0.1\% = \gamma_{xy}/2$ are scaled 100x. Principle stress directions are horizontal and vertical. Cross-sections are taken at $z$=3/8, 1/2 and 5/8 (left to right respectively). As wall thickness increases the short ligaments thicken and shorten, decreasing in aspect ratio dramatically, increasing their bending stiffness and the overall shear stiffness of the design. Cell walls in the DF take on curvature at all shear strains, $\bar{\gamma}_{xy} > 0$, with zero initial wall curvature, yet the antisymmetric nature leaves some cross-sections with straight lines where antisymmetric buckling mechanisms converge (left and right columns). As relative density increases complementary buckling mechanisms are inhibited causing more energy to be stored through stretching. Contours of strain energy density around the average are plotted at the expense of fidelity near strain energy concentrations, the magnitude of which are mesh dependent and do not contribute substantially to the total strain energy. (Negative strain energy levels indicated in legends are fictitious and do not actually occur in models.)**

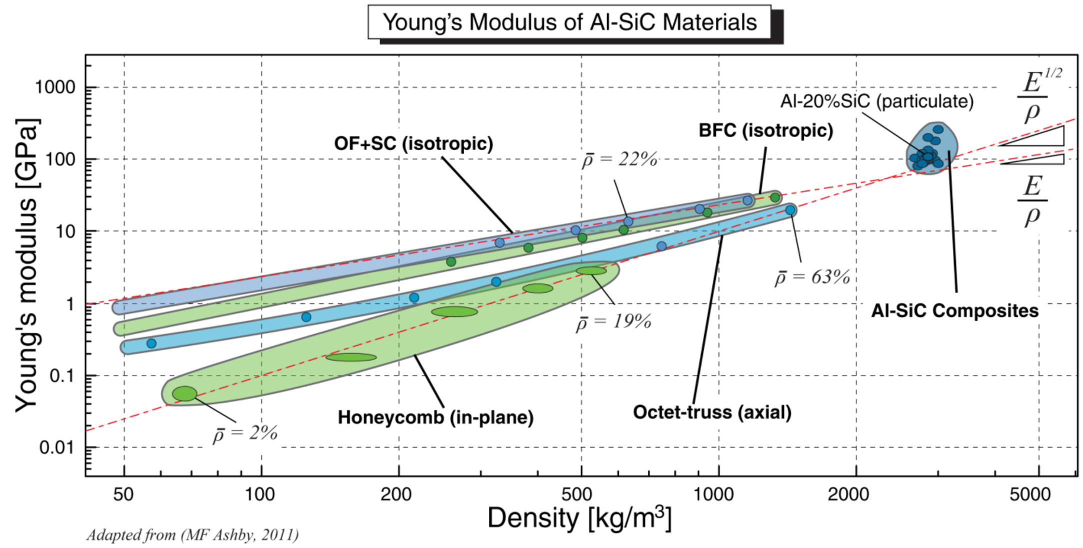

*Adapted from (MF Ashby, 2011)*

**Figure 41 – Ordered foams and lattices comprised of an Al-20%SiC composite outperform stochastic foams made from the same material. While the octet-truss has comparable shear stiffness to isotropic stretch dominated foams at low relative densities (~1/3 of the Voigt bound), it is anisotropic and has an axial stiffness that approaches that of stochastic foams at relative densities $\gtrsim 20\%$. The stiffness of the OF+SC foam is almost directly proportional to $E/\rho$, while the BFC foam, having stiffness similar to the Q-R foams (~1/3 of the Voigt bound at low relative densities), has the performance of theoretical stretch dominated lattices of** (Ashby, 2011)**.**

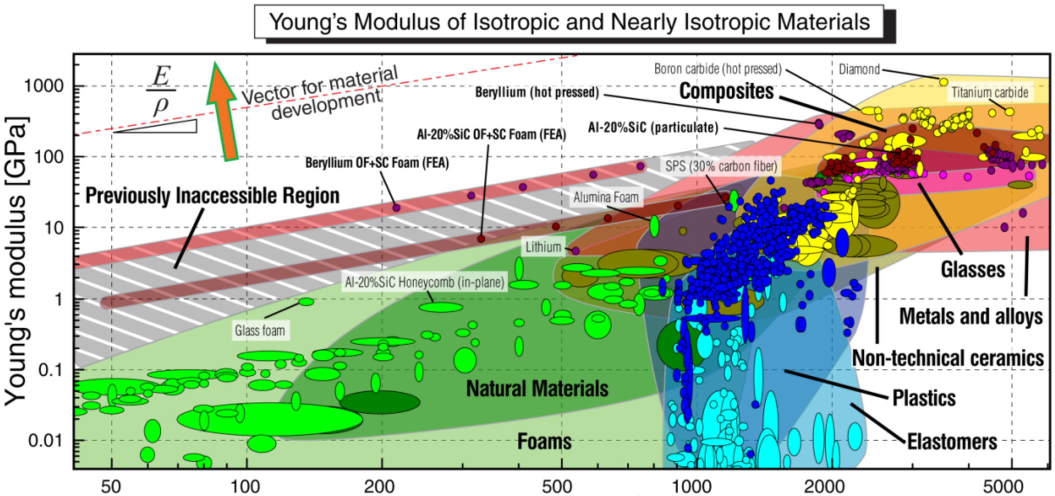

*Adapted from (MF Ashby, 2011)*

**Figure 42 – Finite element (FE) results for the OF+SC foam composed of an Al-SiC composite, and Beryllium, are placed in the universe of available isotropic, or nearly isotropic, materials; excluded from this are fibers, laminates and woods. Only the stiffest foams, made of ceramics, rival the stiffness of the Al-SiC OF+SC foam, and then only at densities above 600 (kg/m$^3$). The OF+SC foam composed of Beryllium can potentially be more than one order of magnitude stiffer, at a given density, than currently available nearly isotropic materials; a system incorporating this material would realize a proportional and dramatic weight savings. As single crystal diamond is not a reasonable constituent material, and polycrystalline diamond has only half its stiffness, the maximally stiff OF+SC foam composed of beryllium represents the maximum performance achievable by any material system barring the development of new materials on the atomic scale.**

# IV. Design Considerations for Ordered Foams

The representative selection of foam topologies described in the previous chapter exhibit a wide range of properties however there remains the possibility to utilize some of the design lessons from this study to create materials with properties highly tailored for a specific application.

The isotropy of materials can be altered by the addition, or increasing the thickness, of certain cell walls with favorable orientations relative to the applied load. For example the OF+SC foam has the clear potential to possess any isotropy between being isotropic, as it is described in this study, to as anisotropic and stiff in shear as the OF, the stiffest in shear, by altering the relative wall thickness of the OF and SC substructures.

The continuity of cell-walls between neighboring cells is responsible for the stiffness of designs with maximal performance. The observation that this property is required for maximal stiffness is perhaps obvious in retrospect. For a member, be it a cell wall or edge, plate or beam, uniformly stretched, to impart such a uniform stress state on an adjacent member, those members must be aligned. One can imagine two beams welded together at their ends at an arbitrary angle. When force is applied to separate the bars the only configuration that produces a uniform stress state is the one where the beams are aligned and stretched axially. Any misalignment of forces or members results in bending, non-uniform stresses and a degradation in structural efficiency . The alignment of cell-walls and the efficient transmission of strain energy between them is of paramount importance in designing high-performance architectures.

Closed cell foams gain significant additional stiffness over comparably aligned open cell structures from the interconnectedness of the material geometry. Every cell wall is constrained at its edges by neighboring cell walls thereby greatly reducing the degrees of freedom of every material point in the body. The reduced entropy of closed cell foams drives their performance well in excess of open cell foams and lattice structures. This is evident in contrasting the performance of the OT, FCC foam, and the SC which exhibit the characteristics of an open cell, closed but non-aligned and maximal stiffness closed cell foams respectively.

Buckling of members is significantly mitigated by the constraint of neighboring material in closed cell foams. While this aspect is not directly studied in this work, the DF, for example, responds in buckling to all shear loads and all relative densities yet retains a high stiffness. Any local region that is oriented in a manner that produces significant bending from an applied load is always connected to an adjacent region that must stretch to accommodate this bending. The configurational entropy in closed cell foams is so low that even when cell walls become appreciably thin stretching is still likely to dominate the response.

The strength of ordered foams is of great interest given their appreciable stiffness properties. The assessment of strength however brings with it many more considerations than does the characterization of stiffness. Clearly stress and strain concentrations are of interest, which can to some degree be ascertained from the results in this study, showing strain energy concentrations under some basic loading and boundary conditions. One must also consider to first order the failure mechanisms expected in the material of interest. Material selection is intimately tied to the processing and manufacturing methods chosen, the properties of which will determine defect magnitudes, population and distribution. It is safe to assume that a single unit-cell is representative in the case of stiffness, but when considering failure the periodicity of deformations can easily extend beyond the characteristic dimension of the geometric unit cell. Tearing and other localized deformation in the regions neighboring the boundary of an applied load may be significant in the onset macroscopic failure. Considering a detailed multi-unit-cell model is not currently intractable but brings with it the need for considerable computational resources. These needs will only diminish relatively with the development of faster and cheaper hardware but currently large parametric studies are cumbersome, requiring a significant amount of resources to process and store the associated data.

There is no singular structural feature that is found to give rise to higher stresses irrespective of the loading conditions. In some loading scenarios and topologies edges possess the highest strain energy concentrations, and are perhaps likely failure initiation zones, while in others cell faces become the focus.  While it is difficult to make specific predictions about the strength of ordered foams one can observe that stress and strain concentrations are detrimental to both strength and stiffness performance.  Maximal performance designs should have strength far in excess of stochastic foams and even lattices due to their ability to store strain energy relatively uniformly.  Although the specific strength performance must be interrogated it is unlikely that the strength performance of ordered foams should suffer disproportionately when compared to stochastic foams and lattice structures.

# V. Concluding Remarks

In the previous chapters two material systems are presented that possess novel properties, offering high stiffness combined with relatively low density. Chapter one details a material that expands the bounds of property space, pairing low, zero or even negative thermal expansion with near theoretically maximum stiffness. In the second chapter a family of ordered foams is found to include a geometry that achieves theoretical bounds for Young's, shear and bulk modulus simultaneously. This material has the potential to achieve more than ten times the stiffness of other known comparable material systems, including stochastic foams, honeycombs and lattices, offering a revolutionary leap in achievable material performance. In the realm of aerospace and high-performance transportation, where vehicle mass is of primary importance, such materials will undoubtedly have a profound impact upon designs in the future. Contemporary computer automated design and finite element representative volume element modeling have proven to be the prime tool of merit in investigating the behavior of these types of cellular materials. Cellular materials are difficult to characterize experimentally due to topological complexity and problems of scale. Assessing constituent properties and cell geometries are difficult as are the application of forces through appropriate boundary conditions. While some experimental work has been done in terms of fabricating and measuring the performance of tailorable thermal expansion lattices there remains almost a complete absence of work on ordered closed cell foams. It is our hope that this body of work will serve as a starting point for the realization of such lattices and foams with such notably unrivaled properties. The advantages of realizing these materials in a practical context is manifest in their superior properties.